

**NONDESTRUCTIVE ASSAY OF NUCLEAR
MATERIALS BY GAMMA RAY
SPECTROMETRY**

By

Chhavi Agarwal

Bhabha Atomic Research Centre, Mumbai

A thesis submitted to the

Board of Studies in Chemical Sciences

In partial fulfillment of requirements

for the Degree of

DOCTOR OF PHILOSOPHY

of

HOMI BHABHA NATIONAL INSTITUTE



March, 2011

STATEMENT BY AUTHOR

This dissertation has been submitted in partial fulfillment of requirements for an advanced degree at Homi Bhabha National Institute (HBNI) and is deposited in the Library to be made available to borrowers under rules of the HBNI.

Brief quotations from this dissertation are allowable without special permission, provided that accurate acknowledgement of source is made. Requests for permission for extended quotation from or reproduction of this manuscript in whole or in part may be granted by the Competent Authority of HBNI when in his or her judgment the proposed use of the material is in the interests of scholarship. In all other instances, however, permission must be obtained from the author.

Chhavi Agarwal

DECLARATION

I, hereby declare that the investigation presented in the thesis has been carried out by me. The work is original and has not been submitted earlier as a whole or in part for a degree / diploma at this or any other Institution / University.

Chhavi Agarwal

Dedicated to my parents

List of Publications

REFEREED JOURNALS

- [1] “Determination of uranium in aqueous attenuating samples using gamma ray spectrometry.” **Chhavi Agarwal**, P.C.Kalsi, A. Mhatre, and A. Goswami, *Applied Radiation and Isotopes*, 65 (2007) 1386.
- [2] “A simple numerical method for gamma ray self-attenuation correction for samples of common geometries.” **Chhavi Agarwal**, Sanhita Poi, A. Goswami, Manohar Gathibandhe, R. A. Agrawal, *Nuclear Instruments & Methods in Physics Research A*, 597 (2008) 198.
- [3] “Attenuation Correction factors for cylindrical disc and box geometry.” **Chhavi Agarwal**, Sanhita Poi, Amol Mhatre, A. Goswami and Manohar Gathibandhe, *Nuclear Instruments & Methods in Physics Research A*, 607(2009) 439.
- [4] “Nondestructive determination of plutonium by gamma spectrometry and neutron well coincidence counting.” **Chhavi Agarwal**, Sanhita Poi, T. N. Nathaniel, Amol Mhatre, P.C. Kalsi, Sarbjit Singh and A. Goswami, *Journal of Nuclear Materials*, 385 (2009) 131.
- [5] “Full energy peak efficiency calibration of HPGe detector for point and extended sources using Monte Carlo code.” **Chhavi Agarwal**, Sanhita Chaudhury, A. Goswami and Manohar Gathibandhe, *Journal of Radioanalytical and Nuclear Chemistry* 287 (2011) 701.
- [6] “Coincidence summing corrections for point and extended geometries” **Chhavi Agarwal**, Sanhita Chaudhury, A. Goswami and Manohar Gathibandhe, *Applied Radiation and Isotopes* 289 (2011) 773.
- [7] “Nondestructive assay of plutonium in empty stainless steel boxes by apparent mass method.” **Chhavi Agarwal**, Sanhita Chaudhury, A. Goswami and M. Gathibandhe, *Journal of Radioanalytical and Nuclear Chemistry* (Accepted).

REPORTS

- [8] “Gamma ray self-attenuation correction: a simple numerical approach and its validation.”
Chhavi Agarwal, Sanhita Poi, Amol Mhatre and A. Goswami, BARC external report, BARC/ 2009/E/005.

CONFERENCE PROCEEDINGS

- [9] “Estimation of uranium in liquid sample by gamma ray spectrometry: Effect of gamma-ray attenuation.” **Chhavi Agarwal**, Amol Mhatre, P. C. Kalsi and A. Goswami, DAE-BRNS Symposium on Nuclear and Radiochemistry symposium at Maharaja Sayajirao University of Baroda, Vadodara, February 14-17, 2007.
- [10] “Attenuation correction factors for disc geometry.” **Chhavi Agarwal**, Sanhita Poi, Amol Mhatre and A. Goswami, DAE-BRNS Symposium on Nuclear and Radiochemistry at SVKM’s Mithibai College of Arts, Vile Parle (W), Mumbai, January 7-10, 2009.
- [11] “Nondestructive determination of plutonium by gamma spectrometry and neutron well coincidence counting.” **Chhavi Agarwal**, Sanhita Poi, T.N. Nathaniel, Amol Mhatre, P.C.Kalsi, Sarbjit Singh and A.Goswami, Plutonium Futures “The Science”2008 at Dijon, France, July 7-11, 2008.
- [12] “Nondestructive assay of plutonium in empty stainless steel boxes by apparent mass method.” **Chhavi Agarwal**, Sanhita Chaudhury, A. Goswami and M. Gathibandhe, Fourth International Symposium on Nuclear Analytical Chemistry (NAC IV), Mumbai, November 15-19, 2010.
- [13] “Coincidence summing corrections for point source geometry.” **Chhavi Agarwal**, Sanhita Chaudhury, A. Goswami and M. Gathibandhe. DAE-BRNS Symposium on Nuclear and Radiochemistry at GITAM University, Visakhapatnam, February 22-26, 2011.

ACKNOWLEDGEMENTS

First and Foremost, I would like to express my sincere gratitude to my research guide **Dr. A. Goswami** for the continuous support of my Ph.D. study and research, for his patience, motivation, enthusiasm, and immense knowledge. His guidance from the initial to the final level enabled me to develop an understanding of the subject and helped me in the timely submission of this thesis. I could not have imagined having a better guide and mentor for my Ph.D. study. He will be a source of inspiration always. Besides my research guide, I would like to thank **Dr. P.C. Kalsi**, my co-guide for his encouragement and support throughout the work.

I am grateful to the Director and Associate Director of Radiochemistry and Isotope Group for permitting me to register for my Ph.D. and for their support. I am also grateful to **Dr. V.K.Manchanda**, Head Radiochemistry Division and Chairman of my Ph.D. committee, for his moral support throughout the work. I would also like to thank the members of my Ph.D. committee: **Dr B.S.Tomar**, **Dr Bency John** and **Dr. P.K.Pujari** for their time, insightful comments and questions. I am particularly indebted to **Shri Manohar Gathibandhe** for teaching us the MCNP code which we have used almost at every stage of the work and the use of which has made the work more valuable.

I wish to express gratitude towards **Dr. Sarbjit Singh**, **Dr. T.N.Nathaniel**, **Dr. H. Naik** and **Dr. A.K.Pandey** for providing valuable suggestions from time to time during the course of my Ph.D. work. I am indebted to many of my fellow labmates, particularly **Sanhita Chaudhury**, **Amol Mhatre**, **Vivek Chavan** and **Sadananda Das** for all the precious help and cooperation that they lent to me during my research work. I am heartily thankful to many of my colleagues **Suparna Sodaye**, **Kathi Sudarsan**, **Rahul Tripathi**, **Arunasis Bhattacharya**, **Neetika Rawat**, **Sumit Kumar**, **Manoj Mohapatra**, **Dhanadeep Dutta** and **Seraj Ansari**, for sharing their knowledge and to help me on day to day basis. I also must mention the valuable support that I received from

Aishwarya Soumitra Kar, Sandeep Sharma, Priya Maheshwari, Arijit Sengupta, Amit Kumar and *Santosh Gupta*. I am pleased to have good friends in them, on whom I can rely for any help. Many thanks goes to the *Electronics and Instrumentation Section* of the Radiochemistry Division for extending their help for the repair of electronic instruments as and when required and prevented my work from getting hampered. I also take this opportunity to express my gratitude towards all my seniors and colleagues of Radiochemistry and Isotope Group who in one way or the other have always helped in my work.

I would like to thank my *family* for all their love and encouragement. My *parents* deserve special mention for their support in all my pursuits and their persistent confidence in me. I owe my every achievement to them. I also thank my younger siblings *Pooja* and *Shilpi* for their love and support at times I tend to give away. Words fail me to express my appreciation to my husband *Shankar* for his support, encouragement, and patience especially during the final stages of this Ph.D. Also I thank all my *friends* for their love and support over the last few years. I am privileged to have them around me. Lastly, I would like to thank everybody who was important to the successful realization of this thesis, as well as expressing my apology that I could not mention everyone personally.

Chhavi Agarwal

CONTENTS

	Page No.
SYNOPSIS	1
LIST OF FIGURES	20
LIST OF TABLES	26
CHAPTER	
1 INTRODUCTION	29
1.1 Nondestructive Assay: A General Overview	30
1.2 Passive Nondestructive Assay Methods	33
<i>1.2.1 Passive neutron counting</i>	34
<i>1.2.2 Passive gamma ray spectrometry</i>	36
1.3 Gamma ray Interaction with Matter	37
1.4 Different Types of Gamma ray Detectors	42
1.5 Conventional Gamma ray Spectrometry vs. Gamma based NDA	45
1.6 Role of Gamma ray Spectrometry in NDA	46
1.7 Need of Simulation in NDA	47
1.8 Monte Carlo Method	49
<i>1.8.1 Basic principle</i>	49
<i>1.8.2 Random number generation</i>	50
<i>1.8.3 Inverse transform method</i>	51
1.9 Scope of the Thesis	54

2	EXPERIMENTAL AND THEORETICAL TECHNIQUES	56
2.1	Introduction	57
2.2	Gamma ray Spectrometry with HPGe Detector	57
	2.2.1 <i>Basic principle of semiconductor detector</i>	57
	2.2.2 <i>Configurations of HPGe detector</i>	62
	2.2.3 <i>Characteristics of gamma ray spectra</i>	63
	2.2.4 <i>Detector parameters</i>	65
2.3	Instrumentation for Gamma ray Spectrometry	68
	2.3.1 <i>High voltage bias supply</i>	68
	2.3.2 <i>Preamplifier</i>	69
	2.3.3 <i>Amplifier</i>	69
	2.3.4 <i>Single channel analyzer</i>	70
	2.3.5 <i>Multichannel analyzer</i>	70
2.4	Spectrum Analysis	70
2.5	MCNP Code	76
	2.5.1 <i>Structure of the MCNP input file</i>	79
3	HYBRID MONTE CARLO METHOD FOR STANDARD SOURCE GEOMETRY	89
3.1	Introduction	90
3.2	Attenuation Correction Factor	91
	3.2.1 <i>Measurement of linear attenuation coefficient (μ)</i>	92
	3.2.2 <i>Calculation of attenuation correction factor (k_{att})</i>	94
	3.2.3 <i>Aim of this work</i>	97
3.3	Hybrid Monte Carlo Method	99
3.4	Programs	102
	3.4.1 <i>Cylindrical geometry</i>	102

	3.4.2	<i>Box geometry</i>	103
	3.4.3	<i>Spherical geometry</i>	104
	3.4.4	<i>Disc geometry</i>	105
3.5		Validation of the Hybrid Monte Carlo Approach	105
	3.5.1	<i>Theoretical validation</i>	105
	3.5.2	<i>Experimental validation</i>	117
3.6		Conclusion	124
4		APPARENT MASS METHOD FOR NONSTANDARD SOURCE GEOMETRY	126
	4.1	Introduction	127
	4.2	Apparent Mass Method: <i>Basic Principle</i>	128
	4.3	Standardization of Apparent Mass Method	129
	4.3.1	<i>Uranium assay</i>	129
	4.3.2	<i>Plutonium assay</i>	135
	4.4	Applications	138
	4.4.1	<i>Empty stainless steel boxes</i>	138
	4.4.2	<i>Sludge samples</i>	141
	4.4.3	<i>Enriched uranium sample</i>	143
	4.5	Conclusion	144
5		FULL ENERGY PEAK EFFICIENCY CALIBRATION OF HPGe DETECTOR BY MCNP	145
	5.1	Introduction	146
	5.2	Efficiency Calibration: Different Methods	146
	5.3	Monte Carlo Method	149
	5.3.1	<i>Detector parameters determination</i>	150

5.3.2	<i>Effect of detector parameters on the FEP efficiency</i>	154
5.3.3	<i>Optimization of detector geometry</i>	154
5.4	Objective of the Work	155
5.4.1	<i>Gamma spectrometric measurements</i>	155
5.4.2	<i>Monte Carlo simulation</i>	157
5.4.3	<i>Comparison of MCNP and experimental efficiencies</i>	158
5.5	Optimization of Different Detector Parameters	160
5.5.1	<i>Detector crystal geometry</i>	161
5.5.2	<i>Detector end cap thickness and end cap to crystal distance</i>	163
5.6	Efficiency Transfer to Volumetric Sources	169
5.7	Conclusion	171
6	TRUE COINCIDENCE SUMMING CORRECTIONS	172
6.1	Introduction	173
6.2	True Coincidence Summing	173
6.2.1	<i>General overview</i>	173
6.2.2	<i>Factors affecting true coincidence summing</i>	175
6.2.3	<i>Methods for coincidence correction</i>	175
6.3	Objective of the Work	182
6.4	Gamma Spectrometric Measurements	182
6.4.1	<i>Standardization of gamma sources</i>	182
6.4.2	<i>Efficiencies of point sources at different distances</i>	183
6.5	Coincidence Summing Correction for Point Source Geometry	185
6.5.1	<i>Coincidence summing correction factors by analytical method</i>	185

6.5.2	<i>Validation of the analytical method</i>	186
6.5.3	<i>Application of the method</i>	188
6.6	Coincidence Summing Correction for Volumetric Sources	189
6.7	Conclusion	195
7	SUMMARY AND CONCLUSIONS	196
	BIBLIOGRAPHY	204
	APPENDIX	219

SYNOPSIS

Nondestructive assay (NDA) techniques, as the name suggests, are the techniques capable of assaying a sample nondestructively without altering the physical and chemical state of the sample. These techniques rely on the measurement of induced or spontaneously emitted radiation from the nuclear materials such as uranium and plutonium. The energy and intensity of the detected radiation can be correlated to the characteristics and quantity of the radionuclides present. These techniques play a very important role in the assay of nuclear materials and find wide range of applications throughout the nuclear fuel cycle for nuclear materials accounting, process control, safeguards and perimeter monitoring. Although less accurate than conventional chemical/electrochemical techniques, the NDA techniques are direct, fast and amenable to automation leading to higher assay throughput in fuel cycle facilities [Ensslin et al., 1991]. Also NDA techniques are generally versatile with respect to chemical composition and physical configurations and do not require sampling. These techniques are most useful for sealed containers and finished products. NDA is generally the preferred approach when prior knowledge about an item is not available [Carchon et al. (2000)]. However, no single assay technique can be selected that best suits all the requirements due to the diversity of the sample characteristics and the parameters to be measured.

NDA techniques can be classified as Active and Passive. In active mode, radiations induced by nuclear reactions like delayed neutrons, prompt neutrons or gamma rays emitted from the irradiated samples are monitored. Active methods need neutron sources such as nuclear reactors, ^{252}Cf sources or high energy, high intensity X-ray and gamma ray sources. Whereas in passive mode, only radiations such as gamma rays or neutrons

from the radioactive decay of the isotopes of interest are monitored. The selection of an assay technique for a particular application depends on nuclear characteristics of the material, chemical composition and the required accuracy of the measurement. Active interrogation techniques are employed when the isotopes in the sample being assayed do not emit sufficient spontaneous radiations to permit precise measurements in a realistic time period, or when the direct measurement of a fissile isotope is required. The ensuing prompt or delayed fission neutrons can then be counted using a moderating detection chamber, as for passive neutron detection techniques. For example, uranium has a very low spontaneous fission rate (both ^{238}U and ^{235}U) and passive assay of uranium sample by neutron counting does not give the results with sufficient precision in a reasonable time period unless the amounts are high (~kilogram level). Therefore, one has to adopt active interrogation techniques such as irradiating the sample with an AmLi source and monitoring the neutrons from induced fission of ^{235}U . Whereas for assaying a sample containing plutonium by neutron counting, passive NDA techniques can be used owing to the high spontaneous fission rate of the even-even isotopes of plutonium. The present thesis work will be confined to the NDA techniques based on passive assay.

In passive methods, there are two ways to assay the quantity of uranium or plutonium present in the bulk samples of metal, oxide, mixed oxide etc. in sealed containers. Either the neutrons born in spontaneous fission (sf, n) and (α , n) reactions or the gamma ray emitted from nuclear transitions following α or β decay of the nuclide of interest can be monitored. This thesis will be focused on the NDA techniques based on gamma ray spectrometry. The gamma ray intensity is related to the amount of the nuclide monitored.

Passive NDA based on gamma ray spectrometry is different than the conventional gamma ray spectrometry as the samples are generally voluminous in nature. Also samples required to be assayed in NDA are usually in diverse form and containments such as in sealed containers, in solid or liquid form, in waste packets, as scraps etc. Conversion of the measured count rate from such samples to the mass of the nuclide emitting the gamma ray often poses difficult problem due to the loss of proportionality between the measured count rate and the sample amount [Reilly et al. (1991), Parker (1984)]. This may be either due to absorption or scattering of gamma rays by the matrix or due to true and random summing effects. The direct use of calibration standards is difficult due to diversity of size, shape and characteristics of the samples encountered. The problem can be circumvented by devising appropriate procedures for obtaining correction factors for sample self-attenuation, true coincidence summing losses and rate-related losses. The corrected count rate (CR) then is given by:

$$CR = k_{att} \times k_{TCS} \times k_{rate} \times RR \quad (1)$$

where k_{att} , k_{TCS} and k_{rate} are the correction factors for attenuation in the sample, for true coincidence effects and for rate-related losses respectively and RR is the count rate of the sample registered in the detection system. The corrected count rate, CR can then be used to obtain the mass (M) of the isotope emitting the gamma ray of interest using the standard equation:

$$CR = K \times M \quad (2)$$

where K is the calibration constant and is the disintegration rate per unit mass of the sample which can be obtained using a non-attenuating standard of same size and shape as that of the sample. Development of procedures for obtaining the appropriate correction

factors in equation 1 are immensely important for gamma ray spectrometry based NDA techniques and is the aim of this thesis work.

The Monte Carlo method is an indispensable tool for nondestructive assay. This is a universal numerical technique for solving mathematical problems by simulations of random variables. In this method a large number of uniform random numbers are generated between 0 and 1 and these random numbers are transformed into desired distribution. The final result is the average of all the trials. So this method is also called as the method of statistical trials. In nondestructive assay, apart from other applications, this method is predominantly used for the following purposes:

- (i) In designing new nondestructive assay system, Monte Carlo simulation is required to obtain the optimum configurations and the desired efficiency.
- (ii) Verification of any experimental data or any method can be done by simulating the basic facts involved in the experiment.
- (iii) The method is very useful in simulating the full energy peak (FEP) and total efficiency of the detector for various source collimator geometries.

The aim of this thesis work is to develop procedures for obtaining the attenuation and true coincidence summing correction factors which are required to restore the proportionality between the measured count rate and the amount of the nuclide monitored (equation 1 and 2). In the present work, attenuation correction procedures have been developed for both homogeneous as well as inhomogeneous samples. For homogeneous samples, a Hybrid Monte Carlo method has been developed to calculate attenuation correction factors for samples of different geometries. For inhomogeneous samples,

apparent mass method has been standardized for samples with uranium and plutonium as the analyte.

Though the Monte Carlo technique can be used for detector efficiency simulation, the results often do not match with the experimental efficiencies due to incomplete knowledge of the detector geometry. The optimization of the detector geometry is invariably required to match the experimental and calculated efficiencies. Once optimized, the same can be used to simulate efficiency for different source configurations. In this study, geometry of the HPGe detector routinely used in our lab has been optimized to match experimental and MCNP calculated efficiencies at different energies. The total efficiency has also been calculated by MCNP for the optimized detector geometry. These FEP and total efficiencies have been subsequently used to obtain true coincidence correction factors for a number of nuclides like ^{60}Co , ^{152}Eu , ^{133}Ba , ^{134}Cs , ^{106}Ru , ^{125}Sb and ^{144}Ce . These correction factors have been calculated by using analytical method available in literature. The results have also been experimentally validated. The thesis is organized into following seven chapters.

Chapter 1. Introduction

The basic principle of the various NDA techniques available in literature has been described in this chapter. The different NDA methods based on gamma ray and neutron measurements used for the assay of nuclear materials have been briefly reviewed. An introduction to passive gamma ray assay and different types of detectors used for it has been given. Different factors which may result in non-proportionality between the

measured count rate and the mass of the isotope has been discussed. The need for obtaining these correction factors has been described. The importance of the use of simulation in nondestructive assay has been emphasized. The basic principle of the Monte Carlo method which is one of the most common computational tools used in nondestructive assay has been discussed. How a uniform random number is generated and its conversion to a distribution of desired distribution is described. The aim and scope of the present thesis has been discussed.

Chapter 2. Experimental and Theoretical Techniques

In this work, gamma spectrometric measurements have been carried out using HPGe detector. This is a semiconductor diode detector. The main advantage of using a semiconductor detector over other detector types is its good resolution owing to the more number of charge carriers produced per quantum of energy deposited. The basic principle of a semiconductor detector has been discussed in the experimental section of this chapter. The different detector parameters e.g. resolution, efficiency governing the choice of a detector for a particular application have been discussed. Basic components of a radiation detection system such as high voltage bias supply, preamplifier, amplifier and analog to digital converter (ADC) and their functions has been discussed in this chapter. The spectra once acquired, has to be analyzed to obtain the peak areas of the different gamma ray peaks. The gamma ray spectrum analysis has been discussed with reference to PHAST software used in our lab for spectrum analysis. This involves locating a peak, fitting it to a suitable function and determining its area. Usually a gamma spectrum is

used to obtain the number of photons of a given energy emitted per unit time by the source (dps). Efficiency calibration is required to relate the area to the dps of the source. For energy information, the channel output from the ADC is related to the gamma ray energy. The experimental section of this chapter also gives the details of the HPGe detector that has been used for this work.

In the theoretical section, the basic features of the Monte Carlo Neutral Particle Code (MCNP) and its scope have been described. This code can be used for neutron, photon, electron, or coupled neutron/photon/electron transport. In this code, a particle is randomly generated in the source volume and the path of the particle is tracked from its point of origin in the source to the point of its complete absorption in the detector or upto its point of escape from the detector. The probability of its interaction along its track and the type of interaction, are taken care randomly by its mean free path and the relative probabilities of the different interactions ultimately related to the cross sections of the processes in question. In this way a large number of photons are generated and the ultimate result is given as the average of all successes. How a given problem is tackled and a geometrical representation of the system involving the source and the detector is constructed from small building blocks have been explained in detail in this chapter. An input file as a sample has been given to explain all its components and to give the format in which the data has to be given.

Chapter 3. Hybrid Monte Carlo Method for Standard Source Geometry

In NDA, the samples are generally voluminous in nature and the gamma rays while coming out of the sample may be absorbed or scattered within the sample. This is called as self-attenuation of the gamma rays and results in non-proportionality between the count rate and the nuclide mass (equation 1 and 2). As emphasized above, the calibration standards cannot serve the purpose even for the samples with standard geometry unless proper matrix correction is done. Standard sample geometry implies that the standards are generally available so that the efficiencies at the energies of interest are known. So, one has to correct the measured count rate with the attenuation correction factors to get correct results. The attenuation correction factor (k_{att}) is defined as the ratio of the count rate for a non-attenuating sample to that of an attenuating sample of same geometry and is written as:

$$k_{att} = \frac{\int_v \rho I \varepsilon dV}{\int_v \rho I \varepsilon \exp(-\mu t) dV} \quad (3)$$

where ρ = spatial density of the isotope being assayed (g/cm^3),

I = emission rate of the assayed gamma ray ($\gamma/\text{g-s}$),

ε = absolute full energy detection efficiency,

μ = linear attenuation coefficient of the sample,

and t = distance the gamma ray travels within the sample.

This chapter gives an overview of different attenuation correction procedures available in the literature for samples with standard geometry. It has been observed that the

approaches available in literature are valid under certain assumptions regarding sample-detector geometry. The different approaches available are applicable to different ranges of D/R where D is the sample-to-detector distance and R is the sample radius. No common approach is available for all sample geometries and at all sample-to-detector distances. This chapter describes the attenuation correction procedure developed in this thesis work for samples with standard geometry based on Hybrid Monte Carlo (HMC) approach [Agarwal et al. (2008), Agarwal et al. (2009)]. This is a very simple approach and is based on equation 3. For a homogeneous sample, the factor ρI will remain constant in both the numerator and denominator and will cancel out. The parameters ε and t are function of the co-ordinate of the point at which gamma ray originates within the sample and cannot be taken out of the integral. Hence they will not cancel out. Since ε is the efficiency of the detector for a sample-detector geometry and so is inversely proportional to $1/r^2$ where r is the distance the gamma ray travels from the sample-to-detector surface. Therefore the equation 3 simplifies to:

$$k_{att} = \frac{\frac{1}{n} \sum_{i=1}^n 1/r_i^2}{\frac{1}{n} \sum_{i=1}^n \exp(-\mu t_i) / r_i^2} \quad (4)$$

$$= \frac{\langle 1/r_i^2 \rangle}{\langle \exp(-\mu t_i) / r_i^2 \rangle} \quad (5)$$

where r_i is the distance traveled by the gamma ray to reach the detector and t_i represents the distance traveled by the gamma ray within the sample. The HMC method involves

generation of a random point within the sample and on the detector surface. The r_i and t_i are then calculated analytically. In this way, a large number of random points are generated in the sample volume and on the detector surface and the ratio of the averaged numerator and the denominator gives the attenuation correction factor. This method is termed as Hybrid Monte Carlo method because the problem is partly solved by Monte Carlo method and partly by analytical method. This reduces the computational time substantially compared to a full scale Monte Carlo simulation.

This method has been applied to some of the common standard sample geometries e.g. cylinder, disc, box and sphere. The theoretical validation of the approach has been done by comparing the results for cylindrical, box and spherical geometry at different distances with attenuation correction factors calculated by using far and near-field expressions available in literature [Agarwal et al. (2008)]. The results at different distances have also been compared with the attenuation correction factors computed by using MCNP code. An uranium solution of known concentration having experimentally determined $\mu = 0.5 \text{ cm}^{-1}$ at 186 keV was chosen as the matrix. The transmittance of the solution was varied by changing the radius of the cylinder. The unattenuated count rate was obtained by replacing the sample solution by air. The k_{att} was calculated from the ratio of unattenuated to attenuated count rates. The attenuation correction factors from both the HMC method and MCNP were found to match at all sample-to-detector distances and for all the geometries. The experimental validation of the Hybrid Monte Carlo approach at different sample-detector distances was carried out by comparing the computed correction factors with experimentally determined correction factors obtained for cylindrical, disc and box geometry [Agarwal et al. (2009)]. The experimental correction

factors at a particular energy were obtained by taking the ratio of the actual disintegration rate of the sample and the experimental disintegration rate at that energy. The HMC approach was found to be valid at all sample-to-detector distances. It was observed that the near-field formula although meant for close sample-detector geometries do not work at very close sample-to-detector distances. Also near-field formula is not available for all the sample geometries like box and sphere and far-field formula for disc geometry. The advantage of the HMC method is that it is a simple numerical approach which is common to all the geometries and is independent of any approximations regarding sample-detector geometry. This method is found to be applicable at all sample-to-detector distance so that additional care to select a proper formula valid at a particular sample-detector distance is eliminated.

Chapter 4. Apparent Mass Method for Nonstandard Samples

In NDA of nuclear materials, there is a possibility of encountering samples of any nonstandard shape. The usual assay procedures cannot be used for these kind of samples due to unavailability of gamma ray standards leading to difficulty in efficiency calibration. Along with this, the assay of these samples may be limited by self absorption taking place in the samples. Usual attenuation correction procedures cannot be applied as these methods are applicable for standard geometries only. In this chapter, nondestructive assay of nonstandard attenuating samples have been discussed. An empirical approach known as apparent mass method has been proposed by Venkataraman and Croft (2003). This method makes use of the multigamma rays emitted by the nuclides and relies on the empirical relation between the apparent mass of the sample and the gamma ray energy.

Extrapolation of apparent mass to infinite photon energy gives actual mass of the sample (zero photon attenuation condition). In this chapter, work carried out to standardize this method for samples with uranium and plutonium as the analyte has been presented. For this, standard uranyl nitrate solutions [Agarwal et al. (2007)] and PuO₂ packets [Agarwal et al. (2008)] have been used. The uranium concentration in a number of aqueous attenuating uranyl nitrate samples was determined using the apparent mass approach with an adjustment of the exponent of E in the empirical equation from 1.00 to 1.35. Also, work carried out to apply this method to a variety of sample matrices eg. empty stainless steel samples used to store plutonium [Agarwal et al. (Communicated)], sludge samples and enriched uranium samples have been described.

Chapter 5. Full Energy Peak Efficiency Calibration of HPGe Detector by MCNP

Detector efficiency calibration is an integral part of gamma ray spectrometry and is required for getting quantitative information about the nuclide monitored. This can be done by using a set of monoenergetic gamma ray standards eg. ²⁴¹Am, ¹⁰⁹Cd, ⁵⁷Co, ²⁰³Hg, ⁵¹Cr, ¹³⁷Cs, ⁶⁵Zn or by using standard multigamma ray sources like ¹⁵²Eu, ¹³³Ba. The monoenergetic gamma ray standards are not easily available and some of them have short half-lives eg. ⁵¹Cr (27.7 d) and ²⁰³Hg (46 d), requiring frequent replacement. Although the multigamma ray sources provide a good efficiency calibration, the calibration can be erroneous at closer sample detector geometry due to coincidence summing effects. Monte Carlo method can also be used to simulate the efficiencies. The advantage of this method

is that the efficiency can be simulated for a variety of sample shapes and matrices and is free of any coincidence summing effects. However, this method requires detailed detector description. Due to inaccuracy in the detector dimensions, there is often a mismatch between experimental and MCNP efficiencies. Effect of different detector parameters on the FEP efficiency has been studied in literature [Kamboj and Kahn (2003), Vargas et al. (2002)]. Physical characteristics of the detector have been measured experimentally and detector geometry has been optimized by adjusting the detector parameters [Binquan et al. (2005), Helmer et al. (2003), Dryak and Kovar (2006)].

In this chapter, work carried out to optimize the dimensions of an HPGe detector routinely used in our lab for activity determination has been described [Agarwal et al. (In Press)]. The MCNP efficiencies for point source geometry calculated using the manufacturer supplied detector geometry parameters were found to be systematically higher than the experimental efficiencies and a distance dependence of the ratio of the two efficiencies was observed. Details have been given in this chapter on how the different parameters were changed sequentially to match the experimental and MCNP efficiencies for point source geometries. The optimized geometry was then used to calculate efficiencies for extended geometries and compared with the experimental efficiencies. The two efficiencies for both point and extended geometries were found to match within 5%. The advantage of the detector geometry optimization is that once the detector dimensions have been optimized using experimental efficiencies, it can be used for obtaining FEP as well as total efficiencies for various sample geometries without the need of gamma ray standards. Also, the efficiencies obtained from MCNP are free of any

true coincidence summing effects so that these efficiencies can be used at any sample-to-detector distance.

Chapter 6. True Coincidence Summing Corrections

In gamma ray spectrometry, true coincidence summing (TCS) takes place when two or more cascade gamma rays are detected within the resolving time of the detector. There may be summing in and summing out effects resulting from the addition of counts at the energy corresponding to the sum of two energies and loss of counts from the two peaks respectively. These effects will lead to inaccurate activity determination of the nuclide monitored. These effects are independent of count rate of the source and depend solely on the emission probabilities and detection efficiencies of the cascade gamma rays. The magnitudes of these corrections become significant at close sample-to-detector distances owing to a greater probability of two gamma rays reaching the detector simultaneously. These corrections become important for low level measurements where the sample has to be counted close to the detector. An analytical method for computing coincidence correction factors was first demonstrated by Andreev et al. (1972) and has been further developed and modified by other authors [Andreev et al. (1973), Debertain and Schotzig (1979), McCallum and Coote (1975)]. This method involves the use of decay scheme and needs information about the mode of parent nuclide decay, energies of γ -transitions, γ -ray emission probabilities, K-capture probabilities (in electron capture decay), mean energy of K X-rays, fluorescence yield and total and K conversion coefficients. This method also needs full energy peak as well as total efficiencies over the entire energy range. As

explained in the previous chapter, the experimental determination of FEP and total efficiencies needs a large number of monoenergetic standards which are difficult to obtain. Also, the advantage of obtaining efficiencies by MCNP and the need for detector geometry optimization has been already discussed. In the previous chapter, the work on optimization of geometry of an HPGe detector routinely used in our lab has been described. This optimized geometry was then used to get the FEP and total efficiencies required for obtaining true coincidence summing factors. The analytical method for obtaining TCS factors has been standardized for the HPGe detector whose geometry has been optimized. In this method, k_{TCS} is given by:

$$k_{TCS} = \frac{1}{1 - \sum_{i=1}^{i=j} p_i \varepsilon_{i_i}} \quad (6)$$

where, p_i represents the probability of simultaneous emission of i^{th} gamma and the gamma ray of interest and ε_{i_i} represents the total efficiency of i^{th} gamma ray. The coincidence correction factors has been computed for point and extended sources for ^{60}Co , ^{152}Eu , ^{133}Ba , ^{134}Cs , ^{106}Ru , ^{125}Sb and ^{144}Ce .

For validation of the calculation, experimental coincidence correction factors were also obtained. Coincidence correction factors are negligible at sample-to-detector distance greater than about 15 cm. Thus the point sources were first calibrated at a far distance using ^{152}Eu - ^{133}Ba efficiency curve. The disintegration rates of these sources were then used to get experimental FEP efficiencies at closer distances. The experimental correction factors were then obtained by taking the ratio of MCNP to experimental FEP efficiencies.

The two sets of correction factors have been found to compare well thereby validating the analytical approach.

Chapter 7. Conclusions

The last chapter of this thesis includes the main conclusions of this work. Major achievements pertaining to the development of procedures for obtaining different correction factors in NDA of nuclear materials based on gamma ray spectrometry have been summarized as follows:

1. The Hybrid Monte Carlo method developed in this work for obtaining attenuation correction factors has been applied to some common sample geometries eg. cylinder, disc, box and sphere. The correction factors from HMC approach have been compared with MCNP, far-field, near-field and experimental results. This method has been found to be valid at all sample detector distances. The approach is very simple and can be extended to any sample geometry.
2. The apparent mass method has been developed for the assay of attenuating samples of nonstandard geometry. This method has been standardized by using standard uranyl nitrate solutions and PuO₂ packets. It has been observed that for uranyl nitrate solutions, in all the cases, the uranium mass is overestimated and the exponent of E has to be modified from 1 to 1.35 to get results within 4-5% whereas for PuO₂ samples the exponent of E is 1 as suggested by the Venkataraman and Croft (2003). These different exponents for uranium and plutonium can be explained based on the energy range monitored. This method has also been applied to real samples eg.

- sludge, enriched uranium and stainless steel samples for the estimation of uranium or plutonium in these samples.
3. The MCNP code has been used for FEP efficiency calibration of HPGe detector. The MCNP efficiencies calculated for manufacturer supplied detector dimensions were found to be higher than the experimental efficiencies. The detector geometry was optimized by systematically changing the detector geometry parameters eg. detector crystal radius, its length, inner hole radius, dead layer thickness, Al end cap to crystal distance. The efficiency values were found to be within 5% over the entire energy range. The optimized geometry was checked by comparing the MCNP and experimental efficiencies of extended geometries. From this it can be concluded that the manufacturer supplied detector dimensions are not sufficient to obtain efficiencies accurately by MCNP and one has to optimize detector geometry to get good results. Also, it has been observed that the Al end cap to crystal distance is the main parameter which is responsible for the bias between experimental and MCNP efficiencies.
 4. Coincidence summing correction factors have been obtained for point and extended sources. It has been observed that if the sample-to-detector distance is greater than 5 cm, the coincidence summing corrections becomes negligible. These corrections become important for low level samples where sample has to be counted as close as possible to the detector.
 5. MCNP code is a very important tool in nondestructive assay of nuclear materials. It can be used to simulate the detector response for a variety of sample-detector

geometries. It can also be used to optimize the design of a nondestructive assay system before actually setting up the system.

The Chapter is concluded by bringing out the future scope of the research work related to the topic of the thesis.

References

Agarwal, C., Kalsi, P.C., Mhatre, A. and Goswami, A., Appl. Radiat. and Isot., 65 (2007) 1386.

Agarwal, C., Poi, S., Goswami, A., Gathibandhe, M. and Agrawal, R.A., Nucl. Instr. and Meth. A 597 (2008) 198.

Agarwal, C., Poi, S., Nathaniel, T. N., Mhatre, A., Kalsi, P.C., Singh, S. and Goswami, A., J. of Nuclear Materials, 385 (2009) 131.

Agarwal, C., Poi, S., Goswami, A., Gathibandhe, M. and Agrawal, R.A., Nucl. Instr. and Meth. A 607 (2009) 439.

Agarwal, C., Chaudhury, S., Goswami, A. and Gathibandhe, M., J. Radioanal. Nucl. Chem. (In Press).

Agarwal, C., Chaudhury, S., Goswami, A. and Gathibandhe, M., J. Radioanal. Nucl. Chem. (Communicated).

Andreev, D.S., Erokhina, K.I., Zvonov, V.S. and Lemberg, I.Kh. Instrum. Exp. Technol. 15 (1972) 1358 (English translation).

Andreev, D.S., Erokhina, K.I., Zvonov, V.S. and Lemberg, I.Kh., Izv., Akad Nauk, SSSR Ser. Fiz., 37 No.8. (1973) 1609.

Binquan, Z., Jizeng, M.A., Jianping, C., Liye, L. and Yong, M., Nuclear Electronics & Detection Technology 25(3) (2005) 274 (in Chinese).

Carchon, R., Bruggeman, M. and Majkowski, I., Appl. Radiat. and Isot.53 (2000) 317.

Debertin, K. and Schotzig, U., Nucl. Instr. and Meth. 158 (1979) 471.

Dryak, P. and Kovar, P., 2006. Appl. Radiat. and Isot. 64 (2006) 1346.

Ensslin, N., Reilly, D., Smith Jr., H., and Kreiner, S., editors, 1991. Los Alamos National Laboratory 111 (LANL), NUREG/CR-5550 LA-UR-90-732 Available from: [http://www.lanl.gov/orgs/n/n1/panda/.](http://www.lanl.gov/orgs/n/n1/panda/)]

Helmer, R.G., Hardy, J.C., Iacob, V.E., Sanchez-Vega, M., Neilson, R.G. and Nelson, J., Nucl. Instr. and Meth. A 511 (2003) 360.

Kamboj, S. and Kahn, B., Radiat. Meas. 37 (2003) 1.

Mccallum, G. J. and Coote, G. E., Nucl. Instr. and Meth. 130 (1975) 189.

Parker, J. L., 1984. Los Alamos National Laboratory report LA- 10045.

Reilly, D., Ensslin, N., Smith, Jr. H. and Kreiner, S., 1991. United States Regulatory Commission, NUREG/CR-5550, LAUR- 90-732.

Vargas, M.J., Timo' n, A.F., Di'az, N.C., Sa'nchez, D.P., J. Radioanal. Nucl. Chem. 253 (3) (2002) 439.

Venkataraman, R. and Croft, S., Nucl. Instr. and Meth. A 505 (2003) 527.

LIST OF FIGURES

Figure 1.1 Gamma ray emission as a result of a nuclear decay.

Figure 1.2 The mechanism of photoelectric interaction. Here E_γ and E_e are the initial gamma ray energy and the kinetic energy of ejected electron after photoelectric interaction respectively.

Figure 1.3 The energy dependence of the three interaction processes of a gamma ray in germanium and their total effect.

Figure 1.4 The mechanism of Compton scattering. Here E_γ , E'_γ and E_e are the initial and the scattered gamma ray energy and the kinetic energy of scattered electron after Compton scattering.

Figure 1.5 The mechanism of Pair Production.

Figure 1.6 The method of Inverse Transform.

Figure 2.1 Energy band diagrams of (a) Metal, (b) Insulator and (c) Semiconductor.

Figure 2.2 Energy level diagram of a p-type and n-type semiconductor.

Figure 2.3 Junction diode at (a) zero bias (b) forward bias (c) reverse bias.

Figure 2.3 Junction diode at (a) zero bias (b) forward bias (c) reverse bias.

Figure 2.4 Creation of hole shown as positive charge at valance band and excitation of electron to conduction band by interaction of radiation.

Figure 2.5 Different shapes of co-axial HPGe detectors (a) True co-axial (b) Closed-end co-axial (c) Closed-end co-axial (bulletized) [Knoll (2000)].

Figure 2.6 Configurations of a (a) p-type and an (b) n-type closed end co-axial detector [Knoll (2000)].

Figure 2.7 Pulse height spectra of an HPGe detector.

Figure 2.8 Basic components of a radiation detection system.

Figure 2.9 Schematic representation of interaction processes for a photon trajectory in a detector medium.

Figure 2.10 General structure of a MCNP input file.

Figure 2.11 Intersection **(a)** and union **(b)** of two surfaces 1 & 2.

Figure 3.1 Possible gamma ray interactions within the sample volume before reaching the detector.

Figure 3.2 Transmission of a gamma ray through an attenuating medium present in between the source and the detector.

Figure 3.3 The geometrical arrangement of the sample and detector. **(a)** Cylindrical geometry **(b)** Disc geometry and **(c)** Box geometry.

Figure 3.4 Representative paths of two gamma rays from sample to the detector surface.

Figure 3.5 Transmission curve as a function of gamma ray energy using ^{169}Yb as transmission source.

Figure 3.6 Ratio of attenuation correction factors at different distances as a function of transmittance for cylindrical geometry. **(a)** $k_{att}^{\#} / k_{att}^*$

(b) $k_{att}^{\#} / k_{att}^{\$}$

[#] Present calculation

^{\$} MCNP calculation

^{*} From Reilly et al. (1991)

Figure 3.7 Two dimensional model for computing k_{att} for a cylindrical sample.

Figure 3.8 Ratio of attenuation correction factors at different distances as a function of transmittance for cylindrical geometry. **(a)** $k_{att}^{\#} / k_{att}^*$

$$(b) k_{att}^{\#} / k_{att}^{\$}$$

$$(c) k_{att}^{\#} / k_{att}^{\&}$$

[#] Two-dimensional model [Parker (1991)] calculation

^{\$} Present calculation

^{*} From Parker (1991)

[&] From MCNP calculations

Figure 3.9 Ratio of attenuation correction factors at different distances as a function of transmittance for box-shaped sample. **(a)** $k_{att}^{\#} / k_{att}^*$

$$(b) k_{att}^{\#} / k_{att}^{\$}$$

[#] Present calculation

^{*} From Parker (1991)

^{\$} MCNP calculation

Figure 3.10 Ratio of attenuation correction factors at different distances as a function of transmittance for spherical geometry. **(a)** $k_{att}^{\#} / k_{att}^*$

$$(b) k_{att}^{\#} / k_{att}^{\$}$$

[#] Present calculation

^{*} From Parker (1991)

^{\$} MCNP calculation

Figure 3.11 The attenuation correction factors computed using numerical approach for cylindrical geometry as a function of transmittance for different sample-to-detector distances (d) **(a)** $d = 2.5$ cm **(b)** $d = 4.5$ cm **(c)** $d = 20$ cm.

Figure 3.12 The attenuation correction factors computed using numerical approach for disc geometry as a function of transmittance for different sample-to-detector distances (d) (a) $d = 2$ cm (b) $d = 4$ cm (c) $d = 5$ cm.

Figure 3.13 Count rate per gram of ^{57}Co activity at 122 keV as a function of lead acetate concentration. The straight line shows the expected count rate per gram as a function of lead acetate concentration.

Figure 3.14 The attenuation correction factors computed using numerical approach for box geometry as a function of transmittance for different sample-to-detector distances (d) (a) $d = 2.6$ cm (b) $d = 5.0$ cm (c) $d = 20.1$ cm.

Figure 4.1 Absolute efficiency as a function of gamma ray energies (keV) of ^{235}U .

Figure 4.2 The plot of count rate vs. concentration of uranium (mg/ml) at different energies.

Figure 4.3 Apparent mass of uranium as a function of $I/E^{1.35}$ for different samples where E is the gamma ray energy in keV.

Figure 4.4 The apparent mass of plutonium as a function of I/E for different samples, where E is the gamma ray energy in keV.

Figure 4.5 The ^{152}Eu - ^{133}Ba efficiency curve as a function of gamma ray energy.

Figure 4.6 Apparent mass of plutonium as a function of I/E for different samples where E is the gamma ray energy.

Figure 4.7 The apparent mass curve for the two sludge samples.

Figure 5.1 X-ray and gamma ray radiographs of an HPGe detector [Dryak and Kovar (2006)].

Figure 5.2 Schematic diagram of the detector geometry supplied by manufacturer.

Figure 5.3 Experimental and MCNP simulated FEP efficiency for point source geometry using the manufacturer supplied detector geometry at three sample-to-detector distances, $d = 1.7$ cm, 12.6 cm and 21.7 cm.

Figure 5.4 Axial profile of a collimated ^{109}Cd source from the surface of the detector.

Figure 5.5 Experimental and MCNP simulated FEP efficiency for point source geometry using the optimized detector geometry at three sample-to-detector distances, $d = 1.7$ cm, 12.6 cm and 21.7 cm.

Figure 6.1 True coincidence summing effects in the beta decay of ^{60}Co .

Figure 6.2 Effect of solid angle on true coincidence summing effects.

Figure 6.3 A typical decay scheme of a nuclide X decaying to Y .

Figure 6.4 Full energy peak (FEP) efficiencies as a function of gamma ray energy for point source geometry at sample-to-detector distances, $d =$ **(a)** 12.6 cm, **(b)** 6.5 cm and **(c)** 1.7 cm. The solid line corresponds to the fourth order log-log fitting of efficiencies of monoenergetic sources. The nuclides marked with FP in the figure shows the nuclides present in the fission product sample.

Figure 6.5 Corrected Efficiencies as a function of gamma ray energy for point source geometry at $d = 1.7$ cm. The solid line corresponds to the fourth order log-log fitting of efficiencies of monoenergetic sources.

Figure 6.6 The gamma ray spectra of a fission product sample.

Figure 6.7 Efficiencies as a function of gamma ray energy for point source geometry at sample-to-detector distances, $d =$ **(a)** 10.3 cm, **(b)** 6.8 cm, **(c)** 4.4 cm and **(d)** 2.0 cm. The solid line corresponds to the fourth order log-log fitting of efficiencies of monoenergetic

sources. The nuclides marked with FP in the figure shows the nuclides present in the fission product sample.

Figure 6.8 Corrected efficiencies as a function of gamma ray energy for 5 ml geometry at sample-to-detector distances, $d = 2.0$ cm. The solid line corresponds to the fourth order log-log fitting of efficiencies of monoenergetic sources. The nuclides marked with FP in the figure shows the nuclides present in the fission product sample.

LIST OF TABLES

Table 1.1 Comparison of Nondestructive Assay and Conventional techniques for the assay of nuclear materials.

Table 2.1 Specifications of a surface in MCNP.

Table 3.1 Gamma ray energies of ^{169}Yb and ^{235}U .

Table 3.2 Results of k_{att} calculations by the present method and comparison with values available in the literature for samples of different geometries.

Table 3.3 Results of k_{att} calculations by the present method and comparison with values available in the literature and MCNP values for cylindrical sample.

Table 4.1 ^{235}U gamma ray peaks used in the analysis.

Table 4.2 The expected and obtained uranium concentration in aqueous samples.

Table 4.3 Gamma ray energies and intensities of the nuclides used in the analysis.

Table 4.4 The expected and the obtained plutonium amount in the samples.

Table 4.5 Isotopic composition of one of the representative empty stainless box.

Table 4.6 The plutonium amount obtained in different stainless steel samples.

Table 4.7 The results of uranium assay in the sludge sample.

Table 4.8 The results of enriched uranium assay by apparent mass method and by simple gamma counting.

Table 5.1 Monoenergetic sources used as calibration sources.

Table 5.2 Multi-energetic sources used as calibration sources.

Table 5.3 Detector parameters provided by manufacturer and optimized by MCNP simulation.

Table 5.4 The comparison of experimental and MCNP efficiencies at three sample-to-detector distances, $d = 1.7$ cm, 12.6 cm and 21.7 cm. The detector geometry used has been provided by the manufacturer.

Table 5.5 The ratio of MCNP and experimental efficiencies at two sample-to-detector distances, $d = 1.7$ cm and 21.7 cm. The MCNP efficiencies are computed by changing some detector crystal parameters to see its effect on the detector efficiency.

Table 5.6 The comparison of experimental and MCNP efficiencies at two sample-to-detector distances, $d = 1.7$ cm and 21.7 cm. The MCNP efficiencies are computed by changing the Al end cap to detector crystal distance (d_{alc}) to see its effect on the detector efficiency.

Table 5.7 The comparison of experimental and MCNP efficiencies at two sample-to-detector distances, $d = 1.7$ cm and 21.7 cm. The MCNP efficiencies are computed by taking the optimized the Al end cap to detector crystal distance as the basis and further optimization by changing the detector radius and dead layer thickness.

Table 5.8 Ratios of MCNP to experimental efficiencies for 5 ml sources of ^{109}Cd , ^{57}Co , ^{203}Hg , ^{137}Cs and ^{65}Zn and for 100 ml ^{152}Eu source.

Table 6.1 Coincidence correction factors for different nuclides at $d = 1.7$ cm by the analytical and experimental method for point source geometry.

Table 6.2 Coincidence correction factors for nuclides present in fission product sample at $d = 1.7$ cm for point source geometry.

Table 6.4 Coincidence correction factors for different nuclides at $d = 2.0$ cm by the present and analytical method for 5 ml source geometry.

Table 6.5 Coincidence correction factors for nuclides present in fission product sample at $d = 2.0$ cm for 5 ml geometry.

Introduction

- 1.1 Nondestructive assay- a general overview
- 1.2 Passive nondestructive assay methods
 - 1.2.1 Passive neutron counting*
 - 1.2.2 Passive gamma ray spectrometry*
- 1.3 Gamma ray interaction with matter
- 1.4 Different types of gamma ray detectors
- 1.5 Conventional gamma ray spectrometry vs. gamma based NDA
- 1.6 Role of gamma ray spectrometry in NDA
- 1.7 Need of simulation in NDA
- 1.8 Monte Carlo method
 - 1.8.1 Basic principle*
 - 1.8.2 Random number generation*
 - 1.8.3 Inverse transform method*
- 1.9 Scope of the thesis

1.1 Nondestructive Assay: A General Overview

As the name suggests, nondestructive assay (NDA) techniques are the techniques capable of assaying the sample in its existing form without altering the physical and chemical state of the sample. These techniques are generally used for the assay of nuclear materials such as uranium, plutonium. These techniques rely on the measurement of radiation induced or emitted spontaneously from these nuclides. The energy and intensity of the detected radiation is correlated to the characteristics and quantity of the radionuclide present. A variety of radiometric NDA techniques find wide range of applications throughout the nuclear fuel cycle for nuclear materials accounting, process control, safeguards and perimeter monitoring [Baumung et al. (1970), Clapham et al. (1997), Rogers (1983), Berndt (1988), Bäcklin et al. (1991), Hakkila et al. (1993), Cobb et al. (1982), Wells et al. (1991), Henry (1981)].

Although less accurate than conventional chemical/electrochemical techniques, the NDA techniques are direct, fast and amenable to automation leading to higher assay throughput in fuel cycle facilities [Ensslin et al., 1991]. Also, conventional techniques require more rigorous sampling protocols, and hence, are not suited for large scale batch processes and finished products. Chemical techniques generate liquid waste, which demand further recovery of precious actinides. NDA do not require any preparation of radioactive samples and therefore no residual waste forms are created and operator radiation exposure is greatly reduced. Moreover for an inhomogeneous sample, NDA of the bulk item is potentially more accurate than a physical sampling as required by chemical conventional techniques because the finite number of samples may not be representative of the bulk nuclear material. This is because, the distribution of radioisotopes and

therefore radioactivity may not be uniform across the item. Conventional techniques therefore require a strategy to homogenize and sample the item, ensuring that a representative sampling scheme is obtained [Meeks and Chapman, 1991]. NDA is generally the preferred approach when prior knowledge about an item is not available [Carchon et al. (2000)]. Table 1.1 provides a summary of the relative advantages and disadvantages of NDA and conventional chemical methods [Evans, 2009].

Table 1.1 Comparison of nondestructive assay and conventional techniques for the assay of nuclear materials.

Nondestructive assay techniques	Conventional techniques
Nondestructive	Destructive
Less Accuracy	Better Accuracy
No Sampling	Sampling required
Radioactively “clean”	Residual waste forms, secondary wastes
In-situ measurement : possible	In-situ measurement : not possible
Matrix Effects: attenuation, self-absorption, short range of α and β particles	Sampling error, non-homogeneity of matrix
Rapid measurement	Time consuming, expensive

NDA techniques can be classified as Active and Passive. In active mode, induced radiations from nuclear reactions like delayed neutrons [Tuttle (1975), Kull et al. (1970), Moss et al. (2004)], prompt neutrons or gamma rays emitted from the irradiated samples

[Fisher and Engle (1964), Hollas et al. (1987), Norman et al. (2004), Gmar and Capdevila (1999)] are monitored. Active methods need neutron sources such as nuclear reactors, ^{252}Cf sources or high energy, high intensity X-ray and gamma ray sources due to which, these methods pose a greater radiological hazard thus often prohibiting their field application. In passive mode, only radiations from the radioactive decay of the isotopes of interest are monitored like gamma rays from nuclear transitions following α or β decay or neutrons born in either spontaneous fission (sf, n) and (α , n) reactions. Because of the absence of an interrogating radiation source, the passive techniques are much simpler to deploy and pose less radiological hazard to the personnel operating the equipment.

The selection of an assay technique for a particular application depends on the nature of the radioisotope present in the sample, its chemical composition and the required accuracy of the measurement. Active interrogation techniques may be employed when the isotopes in the sample being assayed do not emit sufficient spontaneous radiations to permit precise measurements in a realistic time period, or when the direct measurement of a fissile isotope is required. For example, uranium has a very low spontaneous fission rate (both ^{238}U and ^{235}U), so that with passive neutron assay, results with sufficient precision are not obtained in a reasonable time unless the amounts are very high and one has to adopt active interrogation techniques such as irradiating the sample with an AmLi source and monitoring the neutrons from induced fission of ^{235}U . Whereas for assaying a sample containing plutonium, passive NDA techniques can be used owing to the high spontaneous fission rate of the even-even isotopes of plutonium. The present thesis work will be confined to the NDA techniques in passive mode only.

1.2 Passive Nondestructive Assay Methods

Passive nondestructive assay methods can be realized by either counting the spontaneously emitted gamma rays or neutrons. Calorimetric measurements i.e. the measurement of the heat generated from radioactive decay, due to the interaction of decay products in the surrounding material, are also classed as passive process. Hence there are three main classifications of NDA techniques currently available: gamma ray spectrometry, neutron counting and calorimetry.

The selection of a passive assay technique for a particular application depends on a large number of factors:

- (a) Parameters need to be measured (isotopic composition/radioisotope amount).
- (b) Nuclear characteristics of the radioisotope to be assayed (spontaneous fission rate/ gamma ray intensities).
- (c) Physical characteristics of the sample (physical composition of the contents - materials, density, homogeneity etc and shape/size/composition of container).
- (d) Chemical composition of the sample to be assayed (metal/oxide/fluoride/high Z matrix).
- (e) Required limit of detection.

Due to a large number of variables, the criteria for selection of an assay technique can be complex. Generally, no single assay technique may be sufficient to suit all the requirements and one has to integrate various techniques to achieve a desired sensitivity and accuracy. For example, the interpretation of results from passive neutron measurements and calorimetry require isotopic composition which is obtained either from high-resolution gamma spectrometric measurements or from other destructive techniques

like mass spectrometry. Therefore, gamma ray spectrometry is often combined with both passive neutron counting and calorimetry for plutonium assay, allowing total plutonium mass determination. The problem associated with the gamma ray spectrometry is self-absorption of gamma rays in high Z matrix. Principles of passive neutron counting and gamma ray spectrometry are briefly described in the following:

1.2.1 Passive Neutron Counting

Passive neutron techniques rely upon the detection of spontaneous fission neutrons emitted from the assay material without relying on any external excitation of the sample. In plutonium, for example, the fertile isotopes (^{238}Pu , ^{240}Pu and ^{242}Pu) undergo spontaneous fission generating neutrons. In addition to spontaneous fission neutrons, most plutonium isotopes result in (α, n) neutrons as a result of reaction of alpha particles emitted by plutonium isotopes with the surrounding materials. In many nondestructive assay applications, the neutrons may be accompanied by intense fields of gamma rays, eg. in irradiated fuel measurements.

The two types of detectors mainly used in passive neutron detection are: gas-filled detectors and scintillation detectors. Thermal neutron detection equipment based on gas-filled detectors generally uses either boron trifluoride or ^3He gas-filled proportional counters and is based on detection of charged particles generated as a result of nuclear reactions of neutrons with ^{10}B and ^3He respectively. A variation of gas-filled detectors in which the chambers are lined with a thin layer of uranium highly enriched in ^{235}U is also used. ^4He and CH_4 gas-filled detectors based on proton recoil are available for fast neutron detection. Scintillators of lithium (eg. $\text{LiI}(\text{Eu})$) and boron (eg. B_2O_3 fused with

ZnS) are also used [Knoll, 2000]. Boron and cadmium loaded plastic scintillators are also available [Crane and Baker, 1991]. Generally, in scintillation detectors, fission neutrons and gamma rays both are counted with high probability but can be discriminated by pulse shape analysis [Miller (1968), Normand et al. (2002), Winyard (1972), Czirr (1970)]. Plastic detectors, like most organic scintillators, have several advantages such as faster time response [Kelly et al. (1973), Lyons and Stevens (1974), Lynch (1975), Sanyal et al. (1976)], and higher amplitude pulses over other neutron detectors. These materials can be tailored to a variety of sizes and shapes, and are non-directional in response. However, they usually have poorer stability with increase in temperature and are less rugged [Gozani, 1981]. Due to the high interaction probability of thermal neutrons and low interaction probability of gamma rays i.e. due to their high efficiency for neutron detection and gamma ray insensitivity, the ^3He and BF_3 proportional counters find many applications in the nondestructive assay of nuclear materials. The alternative detectors (^4He , CH_4 , fission chambers and scintillators) are, however, of limited use for waste assay because of the much lower detection efficiencies. Except in the case of fast neutron detectors (^4He , CH_4 and plastic scintillators), in all the other neutron detectors, to increase the detector efficiency, the neutron is thermalized by surrounding the detector with moderator. The information about the neutron energy is thus lost. The amount of a specific nuclide can be determined given the neutron emission intensity and relative abundance of each nuclide. This technique is limited to detection of some plutonium isotopes, where the spontaneous fission rates are relatively high. The abundance of elements in the matrix materials surrounding the nuclear material which can be potential targets for (α , n) reaction will also affect the gross neutron counts [Reilly et al. (1991)].

In such a case, a coincidence technique is often used to distinguish fission neutrons from other neutrons, including from (α , n) reactions in the matrix material. This differentiation is based on the principle that in a spontaneous fission, 2-3 neutrons are usually emitted simultaneously and are thus time correlated. In contrast, neutrons from other sources like (α , n) reactions are emitted at randomly spaced intervals with respect to time. For a well designed setup, the probability of detecting multiple fission neutrons within the coincidence time is relatively high. On the other hand, the probability of detecting an (α , n) neutron or background neutron in this time interval is no greater than it would be in any other time interval of the same duration. Thus, detectors working in coincidence mode selectively detect fission neutrons. Passive neutron detection techniques find wide range of applications in waste assay and safeguards [Kouzes et al. (2008)].

1.2.2 Passive Gamma ray Spectrometry

A nucleus decaying spontaneously by alpha, beta or electron capture process or undergoing a nuclear reaction generally leaves nucleus in an excited state. The nucleus may then deexcite by emission of electromagnetic radiations called as gamma rays. Since the life time of the excited nuclear state is usually shorter (of the order of picoseconds or less) than the alpha (α), beta (β) and electron capture processes, gamma rays appear with a half-life characteristic of the parent nucleus. The energy of the emitted photons is equal to the difference between the energies of the two states of the daughter nucleus involved in transition as shown in Figure 1.1. As the energy levels in a nucleus are discrete, so energy of the gamma rays is characteristic of the daughter nucleus. Moreover, the peak

intensities are the measure of the amount of radionuclides. The gamma ray spectrometry is, therefore, a useful tool for qualitative as well as quantitative assay of radionuclides.

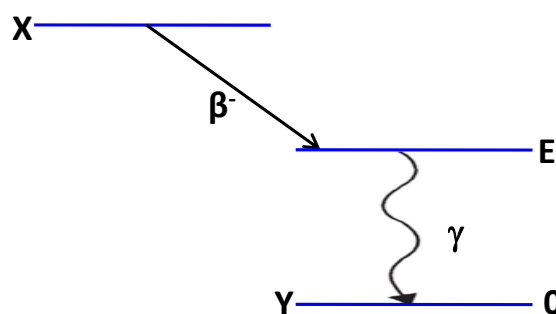


Figure 1.1 Gamma ray emission as a result of a nuclear decay.

1.3 Gamma ray Interaction with Matter

Detection and measurement of nuclear radiations viz. α , β and γ radiations depend on their mechanism of interaction within a medium. Therefore the understanding of how a photon interacts in a medium is essential for its detection and measurement. A photon can interact in a medium by the following three major processes [Knoll, 2000]: (A) Photoelectric effect (B) Compton scattering (C) Pair production.

A. Photoelectric effect

Photoelectric absorption is a process in which a gamma ray photon of energy E_γ interacts with an electron bound to an atom and disappears completely. In its place, the photoelectron is ejected from the atom (Figure 1.2) with a kinetic energy E_e given by Einstein's photoelectric effect equation:

$$E_e = E_\gamma - E_b \quad (1.1)$$

where E_b is the binding energy of the ejected electron in the atom.

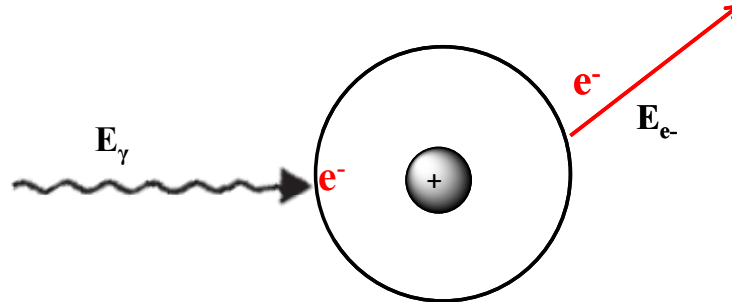


Figure 1.2 The mechanism of photoelectric interaction. Here E_γ and E_e are the initial gamma ray energy and the kinetic energy of ejected electron after photoelectric interaction respectively.

The cross-section (σ_{pe}) for this process is given as:

$$\sigma_{pe} \propto \frac{Z^{4-5}}{E_\gamma^{3.5}} \quad (1.2)$$

where, Z is the atomic number of the medium and E_γ is the energy of the interacting photon. The strong dependence of the cross-section σ_{pe} in Equation 1.2 on Z and E_γ is the reason why this effect dominates for high Z materials and at low energies, but becomes negligible at higher energies. If the energy of the gamma ray photon is more than the binding energy of the K-shell electron then predominantly, the electron is ejected out from K-shell of the atom. If energy is not sufficient to eject a K electron, L or M electrons will be ejected instead.

After photoelectric interaction, the atom is left in an excited state and can regain its ground state in two ways: either the vacancy of the ejected electron is filled by a higher-shell electron and characteristic X-rays are thereby emitted, or the excess energy is

redistributed between the remaining electrons in the atom. The latter process results in the release of loosely bound electrons (Auger electrons). Figure 1.3 shows the energy dependence of the photoelectric cross-section (σ_{pe}) in germanium. The y-axis in the figure represents linear attenuation coefficient which is $N\sigma$ (cm^{-1}) where N is the number of absorber atoms per cubic cm. In the low energy region, the discontinuities correspond to the binding energies of electrons in the various shells and are called as absorption edges. When the gamma ray energies are slightly above the edge, the photon energy is just sufficient to eject a shell electron while just below it, this process is no longer energetically possible. Therefore, the interaction probability drops abruptly.

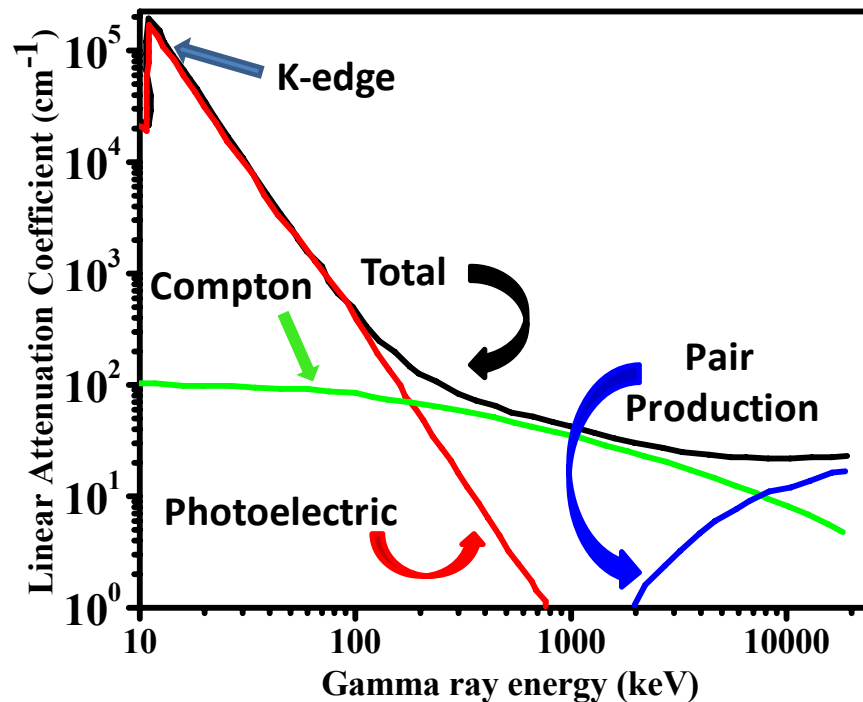


Figure 1.3 The energy dependence of the three interaction processes of a gamma ray in germanium and their total effect.

B. Compton scattering

It is defined as an elastic collision (i.e. total linear momentum and kinetic energy are conserved) of a photon with an electron which is assumed to be free and at rest in the laboratory system. In this, unlike photoelectric absorption, the photon is deflected through an angle θ with respect to its original direction and transfers only a fraction of E_γ to the recoil electron as shown in Figure 1.4.

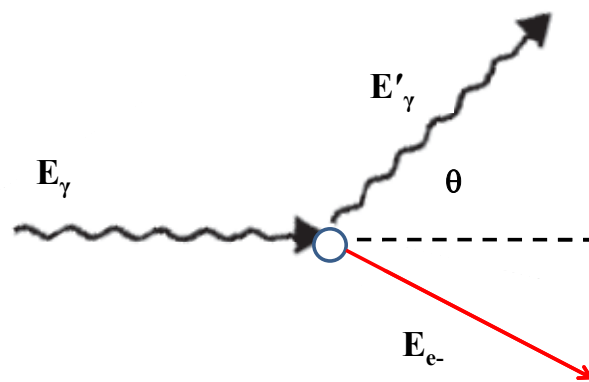


Figure 1.4 The mechanism of Compton scattering. Here E_γ , E'_γ and E_e are the initial and the scattered gamma ray energy and the kinetic energy of scattered electron after Compton scattering.

The cross-section (σ_{cs}) for this process is given as

$$\sigma_{cs} \propto \frac{Z}{E_\gamma} \quad (1.3)$$

where, Z is the atomic number of the medium and E_γ is the energy of the interacting photon. The probability for Compton scattering increases as Z of the medium increases but the dependence is not that strong as photoelectric effect. The interaction probability of a gamma ray by Compton scattering also falls gradually with increasing energy as shown in Figure 1.3.

When gamma ray undergoes Compton scattering in a detector medium, the scattered photon may either escape from the detector or further undergo Compton scattering or photoelectric absorption. Thus, Compton scattering may lead to incomplete deposition of photon energy and usually gives rise to a Compton continuum in the gamma ray spectrum. The energies of the scattered photon (E_γ') and Compton electron (E_e) are given by:

$$E_\gamma' = \frac{E_\gamma}{1 + \frac{E_\gamma}{m_0 c^2} (1 - \cos \theta)} \quad (1.4)$$

$$E_e = E_\gamma - E_\gamma' \quad (1.5)$$

where m_0 is the rest mass of the electron (511 keV). For small photon scattering angles, the energy transferred to the electron is negligible and the secondary photon possesses almost the same energy as the incoming photon and even in the case of backscattering (photon scattering angle, $\theta = 180^\circ$) only a fraction of the gamma ray energy is transferred to the recoil electron. Thus in a Compton scattering process, the gamma ray energy is never fully deposited in just one interaction.

C. Pair production

For gamma ray energies more than 1.02 MeV, pair production becomes energetically possible interaction mechanism. In this process, a photon on interacting with the medium fully disappears and an electron-positron pair is created. The interaction usually occurs in the Coulomb field of the nucleus as shown in Figure 1.5. The probability (σ_{pp}) for this process is given as:

$$\sigma_{pp} \propto Z^2 \ln(E_\gamma - 1.02) \quad (1.6)$$

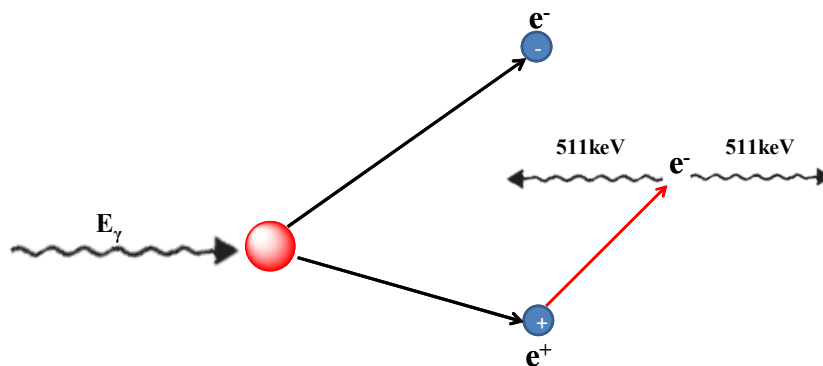


Figure 1.5 The mechanism of Pair Production.

Equation shows that the interaction probability of the photon by pair production increases with its energy. This can also be seen from Figure 1.3 where the interaction probability is zero before 1.02 MeV and after that it increases with gamma ray energy. The excess energy ($E - 1.02 \text{ MeV}$) of the photon is equally shared as the kinetic energy of the produced electron-positron pair. The mechanism of pair production has been shown in Figure 1.5. As shown in the figure, the positron subsequently annihilates after slowing down in the absorbing medium and produces two 511 keV photons at 180° to each other to conserve the linear momentum of the system.

1.4 Different Types of Gamma Ray Detectors

Since an incident gamma quantum is uncharged and creates no direct ionization or excitation in the detector material, a gamma ray detector should serve two fold purposes: First it should act as a conversion medium in which the incident gamma quantum have reasonable probability of interacting to yield one or more fast electrons. It is thus desirable that the detector has a high absorption coefficient so that there is a reasonable probability for complete absorption of the incoming gamma ray. Second, it should act as

a conventional detector where the fast electrons produced deposits their energy to create measurable electric signal. In gamma ray spectrometry, this signal is recorded and is proportional to the gamma ray energy. Two types of detectors are mainly used in gamma ray spectrometry – semiconductor (High Purity Germanium (HPGe), CdTe, CdZnTe) and scintillator (NaI(Tl), plastic, LaBr₃, BGO) detector.

Scintillation detectors

In a scintillation detector, the interaction of a photon with the crystal results in the excitation of atoms to higher energy states, followed by their immediate relaxation with consequent emission of the excitation energy in the form of light. This light is collected on a photocathode, composed of a material with a high probability of photoelectric effect, resulting in the emission of an electron with energy proportional to the energy of the original photon. These electrons are then multiplied in number by successive acceleration in an electric field and collisions on metallic dynodes, finally resulting in a charge burst hitting the anode of the photomultiplier tube. Scintillators in general, and NaI(Tl) in particular, are characterized by a high detection efficiency, counterbalanced by a poor energy resolution (~7% for 661 keV of ¹³⁷Cs). Due to this last feature they are not suitable for cases involving complex spectra with many closely spaced gamma lines.

Semiconductor detectors

In a semiconductor detector, the photon deposits its energy in the crystal and generates electron-hole pairs, which are collected at the respective electrodes by applying a bias to the semiconductor. The most commonly used semiconductor radiation detector is HPGe

detector. These detectors provide good energy resolution (~ 2 keV at 1332 keV). So the detector is preferred for the assay of radionuclides with complex gamma ray spectra. However, room temperature operation of HPGe detector is not possible due to high leakage current which is because of low band gap in Ge. Thus, to guarantee an optimum semiconductor performance, the germanium crystal has to be maintained at very low temperatures, typically using liquid nitrogen (77 K) or electro-mechanical systems. Due to the required cooling, germanium detector units tend to be relatively heavy and large. So their use in hard to access places becomes difficult. For applications where portability or accessibility is an important requirement, other types of crystals have been introduced, such as Cadmium Zinc Telluride (CZT) coupled to a Multichannel Analyzer which provides reasonable energy resolution at room temperature. However, CZT detectors have a poorer energy resolution than Ge detectors. Depending upon the problem, one has to choose an appropriate detector.

Gamma-based NDA instrumentation can be used to quantify those radionuclides that emit gamma rays with sufficiently high intensity. Gamma-emitting waste can be measured either by counting the total number of gamma rays being produced by a sample or by counting the number of gamma rays being produced as a function of gamma ray energy. Non-energy specific, *gross gamma counting* instrumentation can be used to measure material where only a single gamma-emitting radionuclide (or a predictable and simple mixture of radionuclides) is present. Techniques that measure the energy spectrum of the gamma rays being produced, called as *gamma spectrometric* methods, can be further subdivided into *Low Resolution Gamma Spectrometry* (LRGS) and *High Resolution Gamma Spectrometry* (HRGS). Owing to the poorer resolution, the use of

NaI(Tl) detectors in NDA applications is often referred to as Low Resolution Gamma Spectrometry (LRGS). The main advantages of NaI(Tl) detectors are high detection efficiency and low cost enabling large detectors and easy portability. High Resolution Gamma Spectrometry (HRGS) is generally referred to the use of HPGe detectors. The choice of technique depends on the application for which it is to be used. As a rule of thumb, the less that is known (or can be assumed) about the material that is to be measured, the more complex and sophisticated measurement system is required. This thesis will be focused on the NDA techniques based on gamma ray spectrometry based on HPGe detector only.

1.5 Conventional Gamma ray Spectrometry vs. Gamma based NDA

Compared to conventional gamma ray spectrometry, in gamma based nondestructive assay of nuclear materials, the samples required to be assayed usually occur in diverse form and containments such as in sealed containers, in solid or liquid form, in waste packets, as scraps etc. Also, the samples are generally voluminous in nature. Conversion of the measured count rate from a sample to mass of the nuclide emitting the gamma ray often poses difficult problem due to the loss of proportionality between the measured count rate and the sample amount. This may be either due to absorption or scattering of gamma rays by the matrix or due to true and random summing effects. The use of calibration standards is difficult due to diversity of size, shape and characteristics of samples encountered. The problem can be circumvented by devising appropriate procedures for obtaining correction factors for sample self-attenuation, true coincidence summing losses and rate related losses. The corrected count rate (CR) then is given by:

$$CR = k_{att} \times k_{TCS} \times k_{rate} \times RR \quad (1.7)$$

where k_{att} , k_{TCS} and k_{rate} are the correction factors for attenuation in the sample, true coincidence effects and rate-related losses respectively and RR is the count rate of the sample registered in the detection system. CR can be used to obtain the mass (M) of the isotope emitting the gamma ray of interest using the standard equation:

$$CR = K \times M \quad (1.8)$$

where K is the calibration constant and is the disintegration rate per unit mass of the sample which can be obtained using a non-attenuating standard of same size and shape as that of the sample.

1.6 Role of Gamma ray Spectrometry in NDA

Nondestructive assay techniques are used at various stages of the nuclear fuel cycle such as in safeguards, quality control of finished products, nuclear materials accounting and process control [Russo and Vo (2005)]. Gamma ray spectrometry is the most commonly used nondestructive assay technique at all these stages. Like other passive NDA techniques (neutron counting and calorimetry), gamma ray spectrometry also require isotopic composition in order to convert the measured quantity into total mass, but the advantage of gamma ray spectrometry is that it is self sufficient to obtain the isotopic composition while the other techniques rely on gamma ray spectrometry to determine isotopic composition nondestructively. The gamma based NDA technique is used in nuclear safeguards to measure uranium enrichment and plutonium isotopic composition [Reilly et al. (1991), Guardini (2003), Auguston and Reilley (1974), Dragnev (1973), Gosnell et al. (1997), Hsue (1978), Hsue et al. (1978)]. The use of NaI(Tl) detectors

(LRGS) in nuclear safeguards, is limited to the measurement of ^{235}U enrichment in uranium samples. They are suitable for any type of mobile measurements, where the high efficiency allows for shorter measurement times, and thus higher temporal and spatial resolution. High Resolution Gamma Spectrometry (HRGS) using HPGe detector is the preferred technique for plutonium isotopic determination, although it can also be applied to measure uranium enrichment. HPGe combines both sensitivity (the availability of large detector volume) and selectivity (the intrinsically high "energy resolution" of these detectors). No other gamma ray detection technology compares to the performance of HPGe detectors. These detectors are also utilized in many radiation portal monitors developed for security applications. Other important field of application of gamma ray spectrometry in NDA is measurement on spent fuel to confirm its characteristics, cooling time, initial enrichment or burn-up of fuel assemblies. Gamma ray spectrometry is also an important technique for the measurement of quantities of nuclear material holdup in processing equipment [Sprinkle et al. (1996), Russo et al. (1990), Sheppard et al. (1991), Wenz et al. (1991)]. Such passive methods have found application in the assay of materials in waste containers [Reilly et al. (1991), Martz et al. (1992), Simmonds et al. (1990), Estep (1990)].

1.7 Need of Simulation in NDA

Simulation is an indispensable tool of nondestructive assay. Simulation helps in investigating the different aspects of an experimental phenomenon without doing the experiment actually. It helps in better understanding of how the different parameters contribute to the final output. Simulation can provide fruitful improvements in the

measurement procedures and must be considered as one of the available tools in experimental physics [Chard, 2006]. The capability of computational tools has increased dramatically with the development of computer performances. In nondestructive assay, apart from other applications, the simulations are predominantly used for mainly three purposes:

- (i) In designing new nondestructive assay system, simulation is required to obtain the optimum configurations and the desired efficiency.
- (ii) Verification of any experimental data or any method can be done by simulating the experiment and calculating the physical parameters obtained experimentally.
- (iii) The method is very useful in getting the detector full energy peak (FEP) and total efficiency of the detector when it is difficult to determine it experimentally.

Monte Carlo method is one of the most common computational procedure used in nondestructive assay. It is used in both safeguards and waste management applications. Monte Carlo simulations applied to nondestructive assay systems are commonly used as a design tool for NDA equipment [Mariani et al. (2003)], to optimize their performance and to predict their response in different kinds of configurations, as well as a computational calibration technique [Peerani and Looman (2002), Weber (2006)]. Computation codes based on the Monte Carlo method allow the modeling of complex geometries in three dimensions and determination of the response of an NDA instrument without the need of nuclear standards.

1.8 Monte Carlo Method

1.8.1 Basic Principle

Any method which solves a problem by generating suitable random numbers and observing that fraction of the numbers obeying some property or properties is called as a Monte Carlo (MC) method. This is a universal numerical technique for solving mathematical problems by simulations of random variables [Sobol (1993)]. The accepted birth time of Monte Carlo method is 1949 [Metropolis and Ulam (1949)] though theoretical foundation of the method was laid down long before it. The American mathematicians John von Neumann and Stanislaw Ulam are the main originators of this method. Since the simulation of random variables manually is a laborious process, the method became popular only with the advent of computers.

Generally, Monte Carlo methods are used to simulate problems that are too difficult and time consuming when solved by other methods. One can find MC methods used in everything from economics to nuclear physics to regulating the flow of traffic. Of course the way these methods are applied varies widely from field to field, and there are dozens of subsets of MC even within chemistry. In principle, any problem whose development is influenced by random factors is solvable by the Monte Carlo method. By this method a probabilistic model (or several such models) can be artificially constructed. An example is the use of Monte Carlo technique in integrating very complex multidimensional integrals. This is a task that other processes cannot handle well, but which Monte Carlo method can. For example, solving equations which describe the interactions between two atoms is fairly simple, however, solving the same equations for hundreds or thousands of atoms is impossible. With MC methods, a large system can be sampled in a number of

random configurations, and that data can be used to describe the system as a whole [Woller (1996)].

In this method, a random number is sampled from a uniform distribution between 0 and 1 and this random number is transformed into a desired distribution. Similarly, a large number of random trials are carried out, with each trial independent of others and the final result is the average of all the trials. So this method is also called as the method of statistical trials.

1.8.2 Random Number Generation

Uniform random numbers can be produced by the use of some random physical process such as noise in electronic circuit or time interval between decays of a radioactive substance. However, these numbers are not reproducible and specialized devices are required to generate random numbers. Due to this difficulty, generally uniform random numbers are generated using recurrence relation where each successive number is generated by using the preceding number. These types of random numbers are called as pseudorandom numbers since they are not truly random in nature but they satisfy all the conditions that a random number should satisfy. The most commonly used generator is the linear congruential random number generator with the form:

$$U_{n+1} = a(U_n + C) \text{ mod}(m) \quad (1.9)$$

where $\text{mod}(m)$ is the modulus and is the largest number available on the computer, a is the multiplier and C is the additive constant. The size of the modulus constrains the period and is usually chosen to be either prime or a power of 2.

1.8.3 Inverse Transform Method

This method is used for transforming a uniform random number to a random number distributed according to a particular probability density function. Suppose a random number y following a probability density function $p(y)$ is to be generated. This can be obtained by using the fundamental transformation law of probability, according to which the cumulative distribution function of this variable, $F(y)$ can be equated with the cumulative distribution function of a uniform random variable, $F(x)$, where x has a probability distribution function $p(x)$ ($0 < x < 1$):

$$F(x) = F(y) \quad (1.10)$$

$$\int_0^x p(x)dx = \int_0^y p(y)dy \quad (1.11)$$

$$\int_0^x p(x)dx = x \quad (1.12)$$

So,
$$x = F(y) \quad (1.13)$$

The desired transformation which takes a uniform random variable into the one distributed with a probability density function, $p(y)$ is therefore given as [Press et al. (1996)] :

$$y = F^{-1}(x) \quad (1.14)$$

where F^{-1} is the inverse function of F . But this method can only be applied if F^{-1} can be computed analytically. This method is well explained in Figure 1.6. First a uniform random variable x is generated between 0 and 1. Its corresponding y on the definite integral curve is the desired variable. This is the essence of the **inverse transform method**, which was proposed by John von Neumann for generating random numbers.

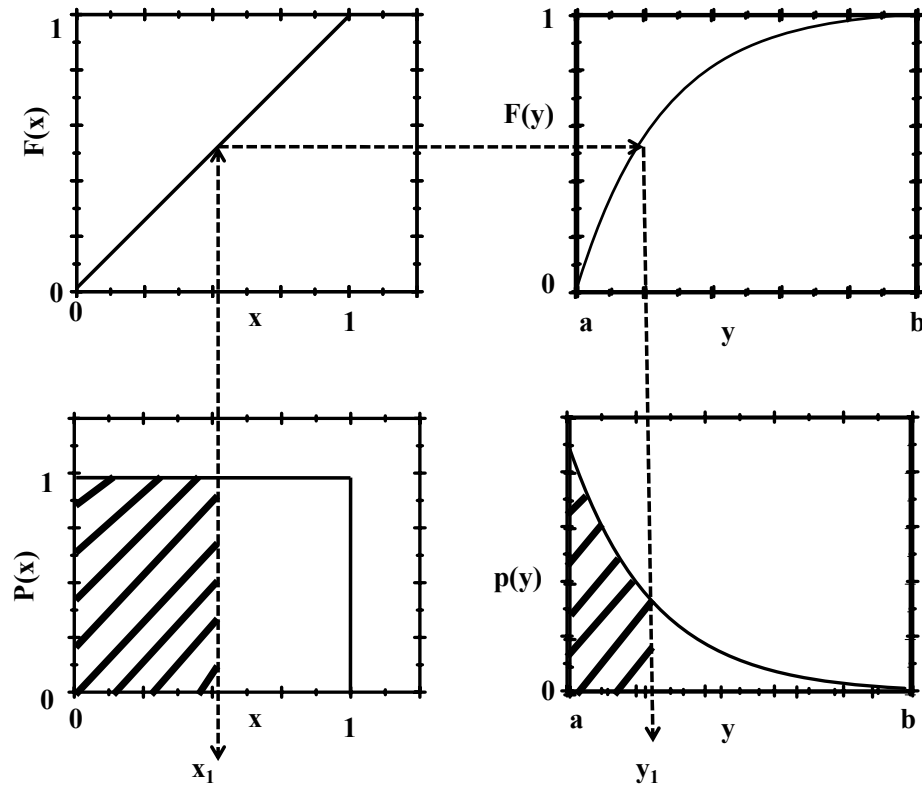


Figure 1.6 The method of Inverse Transform.

The key to the Monte Carlo technique is to recognize that if one lets $F(x_1)$ equal to $F(y_1)$, then a point of connection is made between $p(x_1)$ and $p(y_1)$. A random number, x_1 , is chosen by the computer between 0 and 1. The value x_1 points to a particular value $F(x_1)$. The value $F(x_1)$ points to an equal value $F(y_1)$. The value $F(y_1)$ points to a value y_1 . This y_1 is the random number from the required distribution.

Let us consider the following example of the inverse transform method. Suppose x is a random variable with a probability density function $p(x)$ given by:

$$p(x) = \mu_{total} \exp(-\mu_{total}x) \quad (1.15)$$

This probability density is used to find the random flight path between scattering events of a particle whose total attenuation coefficient is μ_{total} . If we substitute (1.15) into (1.13) and solve, we get:

$$\xi = -(I/\mu_{\text{total}}) \ln(1-\gamma) \quad (1.16)$$

where ξ is the desired random variable and γ is a uniform random variable between 0 and 1. Because $1-\gamma$ is distributed in the same way as γ , we can write

$$\xi = -(I/\mu_{\text{total}}) \ln(\gamma) \quad (1.17)$$

Here, ξ gives the random flight path between two collisions. In such a way, a uniform random variable can be transformed into a random number of desired distribution. However, if inverse function method fails, other transformation methods such as rejection method and composition methods are available. The primary components of a Monte Carlo simulation method include the following:

- *Probability distribution functions (pdf's)* --- the physical (or mathematical) system must be described by a set of pdf's.
- *Random number generator* --- a source of random numbers uniformly distributed in the unit interval must be available.
- *Sampling rule* --- a prescription for sampling from the specified pdf's, assuming the availability of random numbers on the unit interval, must be given.
- *Scoring (or tallying)* --- the outcomes must be accumulated into overall tallies or scores for the quantities of interest.
- *Error estimation* --- an estimate of the statistical error (variance) as a function of the number of trials and other quantities must be determined.
- *Variance reduction techniques* --- methods for reducing the variance in the estimated solution to reduce the computational time for Monte Carlo simulation.

In the Monte Carlo method, the error of calculation is proportional to $\sqrt{(A/N)}$, where A is some constant and N is the number of trials [Sobol (1993)]. So to increase the accuracy of the result one has to increase the number of trials. However, to decrease the error by a factor of n , it is necessary to increase N by a factor of n^2 . To get a higher accuracy by this way is very difficult. Consequently, the Monte Carlo method can be applied for solving those problems that require moderate accuracy. The accuracy of the result can be significantly improved by choice of a computational method having a considerably smaller value of A .

1.9 Scope of the Thesis

The aim of this thesis work is to develop procedures for obtaining the attenuation and true coincidence summing correction factors for nondestructive assay of nuclear materials by gamma ray spectrometry. Attenuation correction procedures have been developed for both homogeneous as well as inhomogeneous samples. For homogeneous samples, a Hybrid Monte Carlo method has been developed to calculate attenuation correction factors for samples of different geometries. For inhomogeneous samples, apparent mass method has been standardized for samples with uranium and plutonium as the analyte. The HPGe detector routinely used in our lab for measurements, has also been calibrated for its full energy peak (FEP) efficiency by using Monte Carlo code. In this study, the HPGe detector geometry has been optimized to match experimental and MCNP calculated efficiencies at different energies. The true coincidence summing correction factors have been calculated for a number of nuclides like ^{60}Co , ^{152}Eu , ^{133}Ba , ^{134}Cs , ^{106}Ru , ^{125}Sb and ^{144}Ce by using analytical method. The correction factors have been calculated

for point and 5 ml cylindrical samples. The FEP and total efficiency has been calculated by MCNP for the optimized detector geometry.

Experimental & theoretical techniques

- 2.1 Introduction**
- 2.2 Gamma ray spectrometry with HPGe detector**
 - 2.2.1 Basic Principle of Semiconductor detector*
 - 2.2.2 Configurations of HPGe detector*
 - 2.2.3 Characteristics of gamma ray spectra*
 - 2.2.4 Detector parameters*
- 2.3 Instrumentation for gamma ray spectrometry**
 - 2.3.1 High Voltage Bias Supply*
 - 2.3.2 Preamplifier*
 - 2.3.3 Amplifier*
 - 2.3.4 Single Channel Analyzer*
 - 2.3.5 Multichannel Analyzer*
- 2.4 Spectrum Analysis**
- 2.5 MCNP code**
 - 2.5.1 Structure of the MCNP input file*

2.1 Introduction

This chapter gives the basic principle of HPGe detector used in the present work. The instrumentation of a gamma ray spectrometry system has been briefly described. The spectrum analysis with reference to PHAST software has been discussed. Then, the basic principle and components of an input file of MCNP code used in the present work has been described.

2.2 Gamma ray Spectrometry with HPGe Detector

2.2.1 Basic Principle of Semiconductor Detector

Every solid material has its own characteristic electronic energy band structure. Highest occupied electronic energy band is called valence band and above which empty band exist called as conduction band. The energy gap between valence band and conduction band is called as band gap.

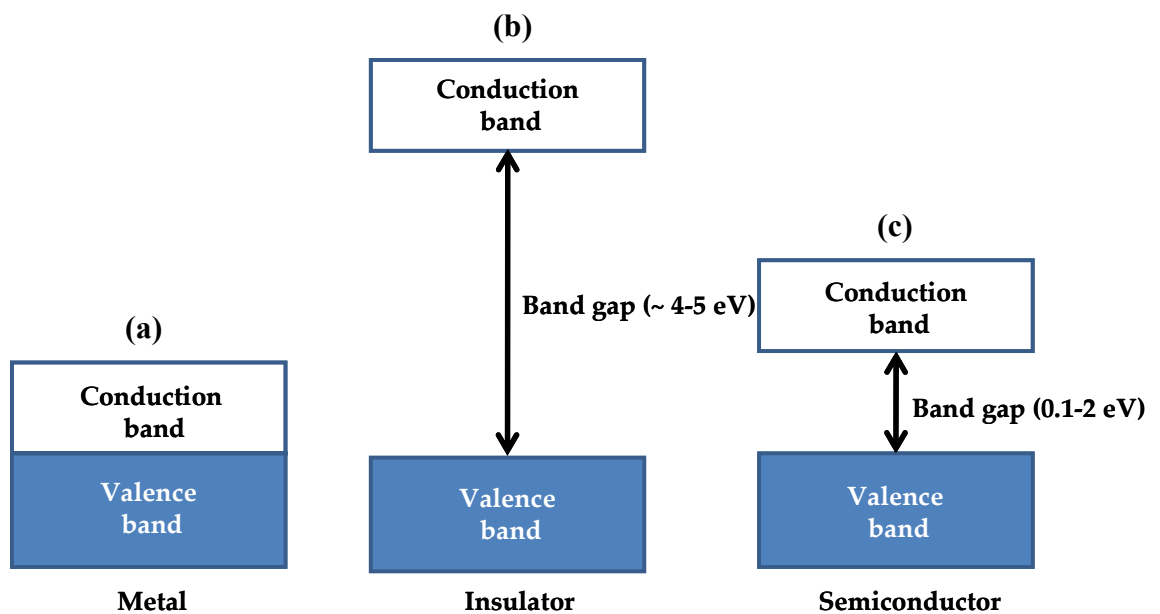


Figure 2.1 Energy band diagrams of (a) Metal, (b) Insulator and (c) Semiconductor.

Depending upon band gap, materials are classified as metal, insulator and semiconductor as shown in Figure 2.1. In case of metal, band gap is zero i.e. valence band and conduction band are overlapping [see Figure 2.1(a)]. Consequently under applied bias, electron can move with low resistance in conduction band. Whereas for insulator, a filled valence band containing no allowed empty state is separated from empty conduction band by band gap of about 4-5 eV, so no empty state is available to carry current under bias [see Figure 2.1(b)]. There are solid materials like silicon, germanium with band gaps in the range of 1 eV [see Figure 2.1(c)]. These types of materials are called semiconductors. Band gap of the semiconductor material is such that a few electrons can get thermally excited from valence band to conduction band leaving hole or positive charge in the valence band. These generated charge carriers (hole and electrons) carry small current under bias. Therefore current in semiconductor can be increased by increasing concentration of either holes or electrons. This has been achieved by doping the semiconductor material. Such doping add a new energy level in the band structure (see Figure 2.2).

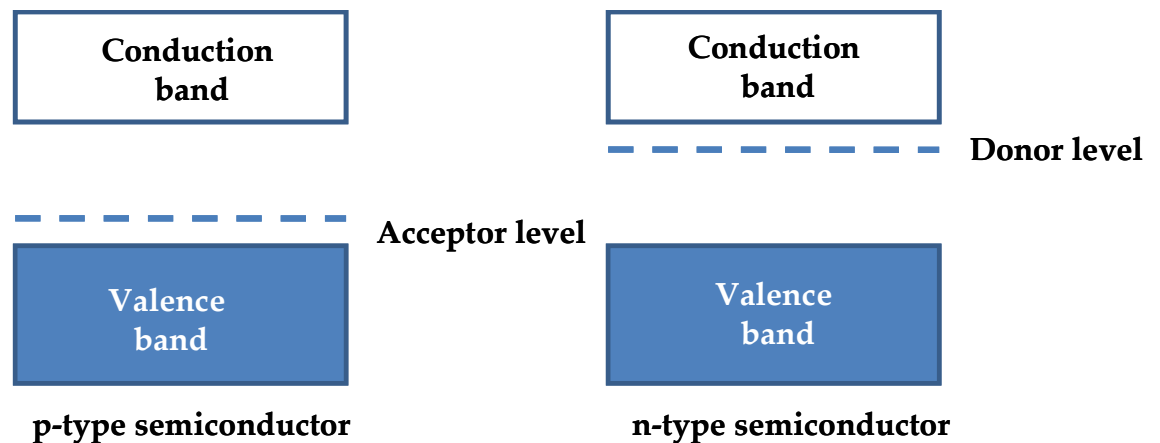


Figure 2.2 Energy level diagram of a p-type and n-type semiconductor.

To increase the hole concentration, the semiconductor crystal (e.g. Si/Ge) is generally doped with atoms with three valence electrons such as B, Al, Ga and In. This type of dopant introduces an impurity level near the valence band. These levels are close enough to accept electrons from valence band due to thermal excitation, leaving behind holes in the valence band. Since they accept electrons, the levels are called as acceptor levels and the semiconductor is called as p-type semiconductor. Similarly, to increase the electron concentration, semiconductor is doped with atoms having five valence electrons (eg. P, As, Sb). This type of dopant introduces an impurity level near the conduction band. These levels are close enough to donate the electrons to conduction band due to thermal excitation, increasing the electron concentration in the conduction band. Since they donate electrons, the levels are called as donor levels and the semiconductor is called as n-type semiconductor.

When n-type and p-type semiconductor are joined together, electron moves from n-type region to p-type region and hole from p-type to n-type until an electric field is developed between the junction to oppose further accumulation of charge. Due to this charge carrier movement, a charge free region is created called as depletion region as shown in the Figure 2.3(a). Such p-n junction called as junction diode readily conducts electricity under forward bias (p-end is positively biased and n-end is negatively biased as shown in Figure 2.3(b) and the depletion region shrinks. In reverse bias, p-end is negatively biased and n-end is positively biased as shown in Figure 2.3(c), due to which depletion region increases and less current flows.

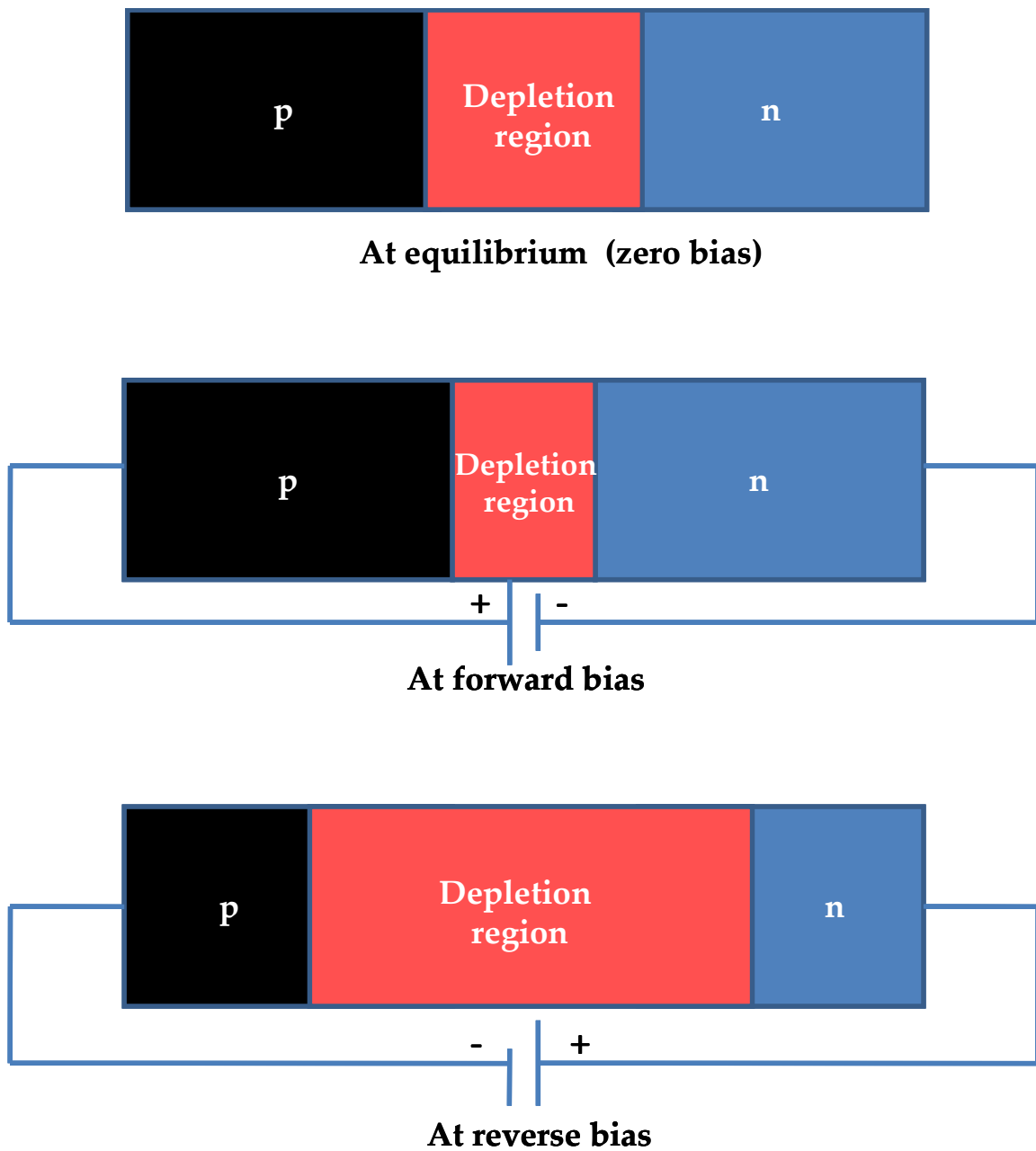


Figure 2.3 Junction diode at (a) Zero bias (b) Forward bias (c) Reverse bias.

In solid state radiation detectors, when radiation passes, equal numbers of electron-hole pairs are created along its track (Figure 2.4). The generated charge is collected by applying an electric field which produces a voltage pulse. When forward biased, even in the absence of ionizing radiation, large current will flow across the semiconductor due to

thermal excitation. This current will obscure the small current due to ionizing radiation. Whereas in case of a reverse biased junction, the current flowing through the semiconductor is negligible and the ionization current can be detected. Moreover, the sensitive volume of the detector i.e. the thickness of the depletion region is more, so that the semiconductors are generally reverse biased to be used as radiation detectors.

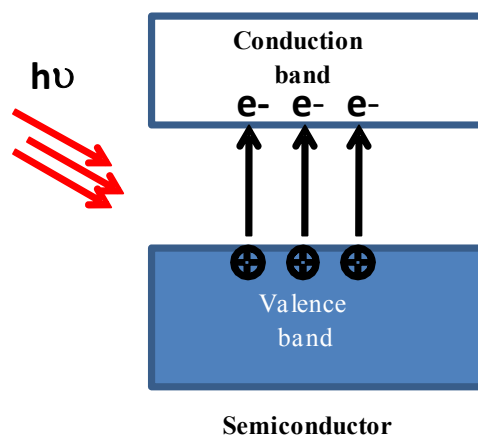


Figure 2.4 Creation of electron-hole pair by interaction of radiation.

In the case of a silicon or germanium of normal purity, the maximum depletion depth (d) beyond 2-3 mm (according to equation 2.1) is difficult to achieve even at breakdown voltage.

$$d = \left(\frac{2\varepsilon V}{eN} \right)^{1/2} \quad (2.1)$$

where V is the reverse bias voltage, N is the impurity (dopant) concentration, ε is the dielectric constant and e is the electronic charge. Gamma ray being highly penetrating in nature requires high depletion depth for detection. According to equation 2.1 for a given voltage, depletion depth (d) can be increased by reducing impurity concentration.

Techniques have been developed to manufacture high purity germanium crystal with depletion depths upto several centimeters. But for Si, manufacturing of such high purity crystal is not possible. The detector based on high purity Ge is known as high purity germanium (HPGe) detector. HPGe has low band gap of 0.67 eV at 300 K. So it can generate current (called leakage current) at room temperature. Therefore HPGe detector is operated at 77 K.

2.2.2 Configurations of HPGe Detector

Based on the shape of detector crystals, there can be two configurations of HPGe detector: planar and co-axial. Co-axial detectors can be open ended or closed ended, as shown in Figure 2.5. Co-axial detectors have large sensitive volumes (750 cc as compared to 10-30 cc of planar detectors) and therefore higher detection efficiencies than planar detectors. Although smaller in size, the planar detectors have best energy resolution because of their low capacitance and are generally preferred for low energy applications eg. for low energy gamma and X-ray spectra of uranium and plutonium.

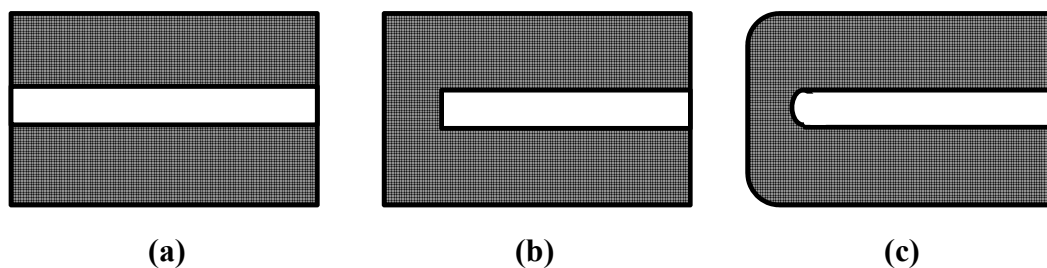


Figure 2.5 Different shapes of co-axial HPGe detectors (a) True co-axial (b) Closed-end co-axial (c) Closed-end co-axial (bulletized) [Knoll (2000)].

In co-axial HPGe detectors, two types of electrical contacts have been used: diffused contact is an n^+ layer and is the positive electrode and metal contact is a p^+ layer and is the negative electrode. These detectors can be generally classified as n-type and p-type detectors. In a p-type co-axial HPGe detector, the diffused contact is on the outside surfaces and the ion-implanted contact is given in the inner hole. Since the diffused contact is thicker, this limits the utility of the p-type detector for gamma rays below 40 keV. In contrast, an n-type co-axial detector, the thinner metal contact is on the outer surface and is usable down to 5 keV. Configurations of a p-type and an n-type closed end co-axial detector have been shown in Figure 2.6.

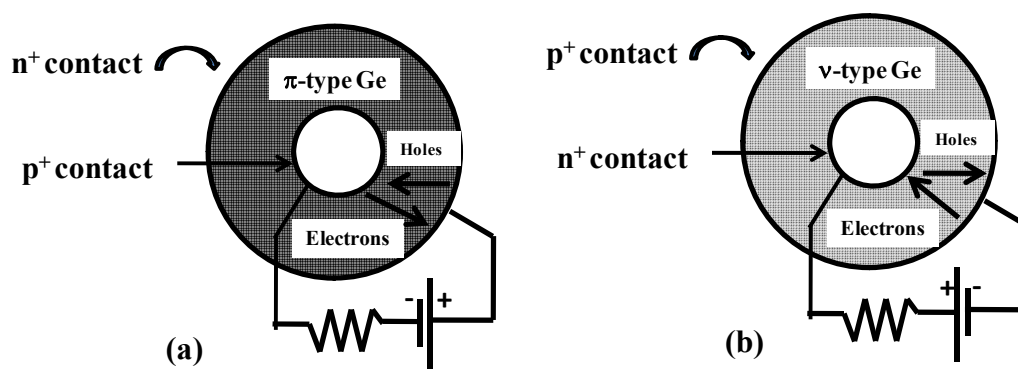


Figure 2.6 Configurations of a (a) p-type and an (b) n-type closed-end co-axial detector [Knoll (2000)].

2.2.3 Characteristics of Gamma ray Spectra

A pulse height spectrum obtained at the end of the measurement reflects the energy deposition of the gamma ray in the detector as shown in Figure 2.7 for a ^{60}Co source. It contains the contribution from all the three gamma ray interaction processes namely photoelectric absorption, Compton scattering and pair production.

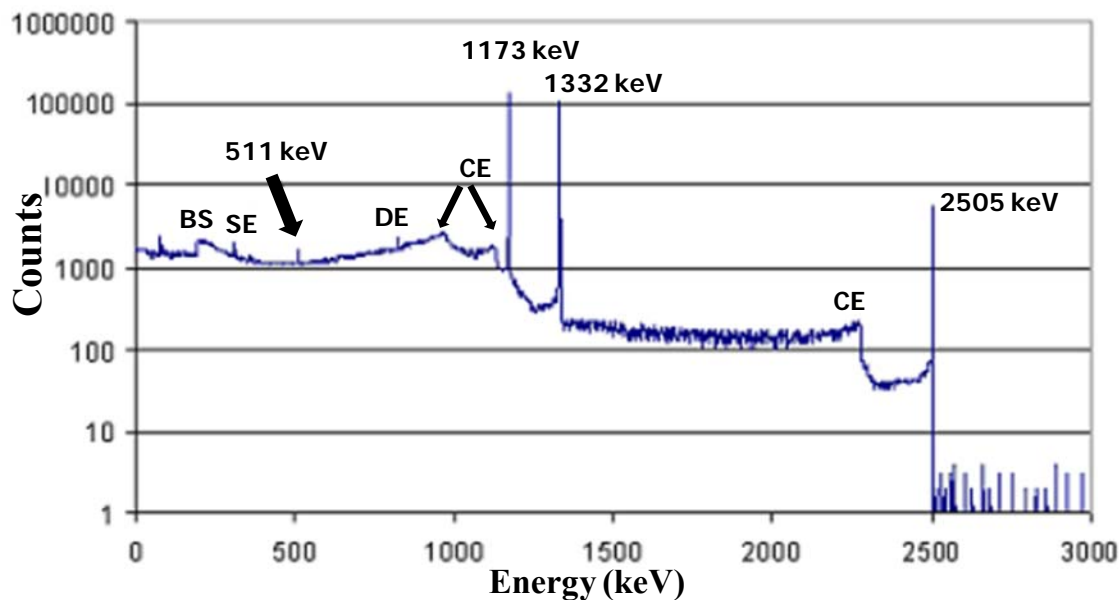


Figure 2.7 Pulse height spectra of an HPGe detector.

Some of the important spectral features are:

- (i) **Full energy peak:** Full energy peak is generated as a result of full energy deposition in the detector by photoelectric absorption, multiple Compton scattering or by deposition of full energy by the two 511 keV photons generated in the pair production as shown in the spectra (Figure 2.7) at 1173, 1332 and 2505 keV.
- (ii) **Compton continuum:** This is generated due to partial energy deposition in the detector due to Compton scattering process.
- (iii) **Compton edge:** The Compton edge appears at an energy corresponding to maximum energy loss by the gamma ray photon in a Compton scattering event. This corresponds to the Compton scattering interaction in which the gamma ray photon is backscattered and is labeled as *CE* corresponding to the Compton edges of gamma rays at energies i.e. 1173, 1332 and 2505 keV respectively in the figure.

(iv) **Compton valley:** This corresponds to the partial energy deposition by a photon after undergoing multiple Compton events and lies between the Compton edge and the full energy peak.

(v) **Backscatter peak:** This arises due to Compton scattering of the gamma ray by more than 110° in the surrounding material and generally occurs at 256 keV for a gamma ray of high energy. This is shown as *BS* in the Figure 2.7.

(vi) **Single escape peak:** This peak appears due to the escape of one 511 keV gamma ray produced in pair production and appears at $(E-511)$ keV as labeled in the Figure 2.7 as *SE*.

(vii) **Double escape peak:** This peak appears due to the escape of both the 511 keV gamma rays produced in pair production and appears at $(E-1022)$ keV as labeled in the Figure 2.7 as *DE*.

(viii) **Annihilation peak:** This is generated due to pair production of the scattered gamma ray in the surrounding material and subsequent annihilation of electron and positron formed, leading to generation of 511 keV gamma ray which is detected in the detector.

2.2.4 Detector Parameters

A detector is generally characterized by two parameters:

(I). **Resolution:** The resolution of the detector is the ability of the detector to resolve two nearby peaks. It is specified as Full Energy at Half Maximum (FWHM) given by:

$$FWHM = 2\sigma\sqrt{2\ln 2} \quad (2.2)$$

The % resolution (R) at a given energy E_o is given by

$$R = \frac{FWHM}{E_o} \times 100 \quad (2.3)$$

Smaller is the R , better is the resolution of the detector. For a co-axial HPGe detector, the value of R is very small and the resolution of detector is generally expressed in terms of FWHM at 1332 keV or at 122 keV for low energy.

(II). Detector Efficiency:

Absolute efficiency of a detector is defined as

$$\varepsilon_{tot} = \frac{\text{total number of detected photons in the full energy peak}}{\text{total number of photons emitted by the source}} \quad (2.4)$$

This is the characteristic of the detector as well as the counting geometry and is expressed as the product of two terms:

$$\varepsilon_{abs} = \varepsilon_{geom} \varepsilon_{int} \quad (2.5)$$

The geometric efficiency is given by

$$\varepsilon_{geom} = \frac{\text{number of photons incident on the detector}}{\text{number of photons emitted by the source}} \quad (2.6)$$

This factor is independent of the gamma ray energy and depends upon the solid angle subtended by the source on the detector (Ω) and is also written as:

$$\varepsilon_{geom} = \frac{\Omega}{4\pi} \quad (2.7)$$

The geometric efficiency is responsible for the inverse square law of the variation of count rates as a function of source-to-detector distance.

The intrinsic efficiency is defined as

$$\varepsilon_{\text{int}} = \frac{\text{number of pulses recorded}}{\text{number of photons incident on the detector}} \quad (2.8)$$

This depends upon the detector characteristics i.e. on the atomic number (Z) of the detector material. Assuming that the photon is normally incident on the detector, the intrinsic efficiency of a windowless detector can be given as:

$$\varepsilon_{\text{int}} = 1 - e^{-\mu t} \quad (2.9)$$

where μ is the linear attenuation coefficient of the detector material and t is its thickness. Higher is the Z , higher will be the intrinsic efficiency and higher will be the absolute efficiency of the detector. It is practically independent of the source-detector geometry. Depending upon the nature of the events monitored, the absolute efficiency of the detector can be of two types:

(i) Full energy peak efficiency: Only the full energy peak is monitored where the counts may come due to full energy absorption of the gamma ray by any of the three interaction processes.

(ii) Total efficiency: All the events are monitored whether it leads to full or partial energy deposition.

The efficiency of an HPGe detector is generally specified by *relative efficiency* which means the efficiency of the detector at 1332 keV relative to efficiency for a point source at that energy of a 3" x 3" NaI(Tl) detector at a source-to-detector distance of 25 cm.

2.3 Instrumentation for Gamma ray Spectrometry

The electric signal produced as a result of collection of charge is analog in nature and is then processed in a pulse processing electronic chain. This typically consists of a preamplifier, amplifier, an analog-to-digital converter (ADC) and a multichannel analyzer (MCA) that produces the gamma spectrum. The components of a radiation detection system have been shown in Figure 2.8. The gamma spectrum is simply the number of photons detected in a preset number of channels, each channel corresponding to an energy band. Finally, the spectrum is analyzed in a PC using specialized software, performing energy and efficiency calibration, peak fitting, background subtraction, peak intensity calculation. The details of these components have been discussed in the following sections.

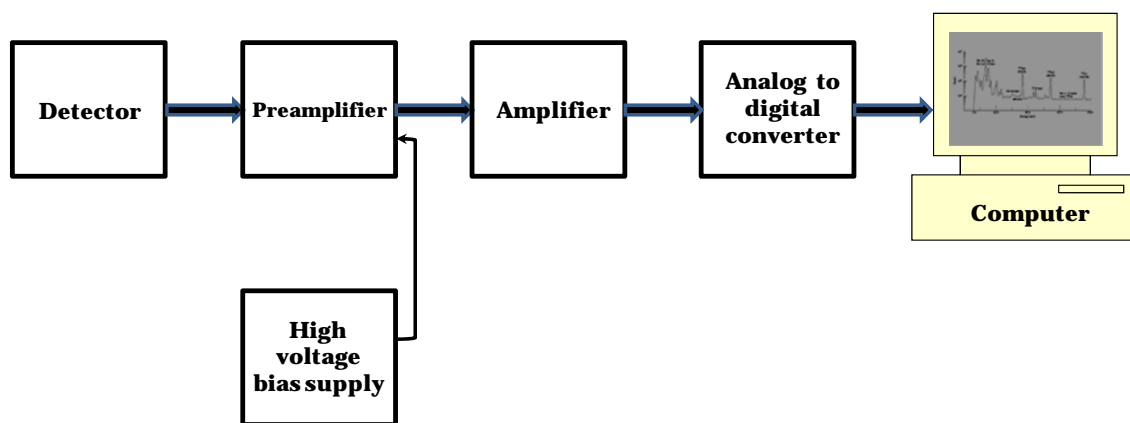


Figure 2.8 Basic components of a radiation detection system.

2.3.1 High Voltage Bias Supply

A bias voltage is required for collection of charge formed in the detector. This voltage is chosen high enough to ensure complete charge collection and low enough to avoid

voltage breakdown. In semiconductor detectors, bias supplies upto 5 kV are required. Electronic switching device, battery packs or charged capacitors can work as high voltage supplies.

2.3.2 Preamplifier

The preamplifier has two main functions: firstly, it converts the low amplitude, short duration current pulse from the detector into a voltage pulse whose amplitude is proportional to the energy deposited by the gamma ray in the detector. Secondly, it maximizes the signal to noise ratio of the output pulse and preserve the gamma ray energy information. To reduce the output noise level, the preamplifier is kept as close as possible to the detector. The output pulse from a preamplifier has a fast rise time (\sim nanosecond) and a slow decay time (\sim 50-100 μ s).

2.3.3 Amplifier

The purpose of a amplifier is to amplify the pulses from the preamplifier into a linear voltage pulse in the range of 0 to 10 V. The amplifier also shapes the pulses to meet the requirements of the pulse height analysis instrumentation. This is important since the analyzer measures the input pulse amplitude relative to a reference voltage so that the output pulse from the amplifier should return as fast as possible to a stable voltage. This is vital for a high quality spectrum. Output pulses from the amplifier can be unipolar or bipolar. The former has a high signal to noise ratio leading to a better resolution. The latter, due to stable and easily detectable zero cross-over point, are used for timing applications.

2.3.4 Single Channel Analyzer

The pulse from the amplifier goes to a single channel analyzer which is a pulse height analysis instrument. Basically it contains two discriminators and only pulses with heights in between the two thresholds are allowed. It is connected to a scalar which will count the number of such pulses.

2.3.5 Multichannel analyzer

The multichannel analyzer (MCA) is the heart of most experimental measurements. It performs the essential functions of collecting the data, providing a visual monitor of the pulse height spectrum produced by the detector. An analog-to-digital converter (ADC) converts the analog voltage pulse from the amplifier into a binary output. The ADC sorts the pulses into a large number of channels according to the height of the voltage pulse and since the height is proportional to the energy of the gamma ray, the relationship between the channel number and energy is nearly linear. Two types of ADC's are commonly used. They are called as Successive Approximation type ADC and Wilkinson type ADC.

2.4 Spectrum Analysis

Once the spectrum has been acquired it has to be analyzed to extract the desired information from the spectrum. Usually a gamma spectrum is used to give energy and number of photons emitted by the source [Debertin and Helmer (1988)]. Since the energy corresponding to full energy events is characteristic of a nuclide, though the spectrum contains all the events, usually only full energy events are monitored. After the

acquisition of spectra for the nuclide monitored, the peaks in the spectrum are analyzed with respect to their location (in channels), their peak area and full width at half maximum (FWHM). In this work, PHAST software [Mukhopadhaya, 2001] have been used for gamma ray spectrum analysis, therefore these operations have been discussed in the light of this software.

Peak Location

Although visual location of the peaks may be the best option, several methods [Mariscotti (1967), Black (1969), Conelly and Black (1970), Slavic and Bingulac (1970), Bullock and Large (1971), Lauterjung (1985)] have been developed to locate a peak in a spectrum. This becomes very useful when large number of peaks have to be located in the spectrum [Debertin and Helmer (1988)]. In PHAST, the derivative method developed by Mariscotti (1967) has been used. The peak shape is Gaussian in nature, which when differentiated two times i.e. when its second derivative is taken, gives a central large negative peak flanked by two smaller positive peaks. Whereas a smooth background gives, a constant first derivative and hence a zero second derivative and a Compton edge gives only one positive peak instead of two peaks as in a Gaussian peak. This behavior of the second derivative is considered as the signature of the peak and it is located at the centre of the negative lobe. If there are two or more closeby peaks than the behavior will be still different from a single peak.

Peak Area Determination

Peak area is needed to get information about the number of photons of a particular energy detected in the detector. The peak area can be obtained by summing up the individual counts of all the channels under a peak. This method cannot be used for a complex spectrum where peaks may be overlapping with each other. Most ADC's are equipped with peak area analysis softwares giving energy and intensity of peaks. Analytical fitting functions such as Gaussian functions are used in such softwares:

$$f(x) = \frac{N}{w\sqrt{\pi/(4 \ln 2)}} e^{-(x-X)^2/2\sigma^2} \quad (2.12)$$

where N is the peak area, X is the centroid, FWHM, $w = 2.35\sigma$. To analyze multiplets, the fitting function has to be modified by introducing additional Gaussian functions. Like for a doublet, the function will be given by:

$$f(x) = \frac{N_1}{w_1\sqrt{\pi/(4 \ln 2)}} e^{-(x-X_1)^2/2\sigma^2} + \frac{N_2}{w_2\sqrt{\pi/(4 \ln 2)}} e^{-(x-X_2)^2/2\sigma^2} \quad (2.13)$$

So that, the number of unknown parameters increases to five: N_1 , N_2 , X_1 , X_2 and σ . However, the actual gamma ray peak shape differs from the ideal Gaussian shape because of tailing on the low energy side. Several complex shape functions, taking the tailing into account, have been used in earlier well-known gamma analysis programs [Helmer and Lee (1980), McNelles and Campbell (1973)]. In PHAST software, a part of the Gaussian function is replaced by the exponential function [Routti and Prussin (1969)]:

$$P(x) = he^{-\frac{(x-p)^2}{2\sigma^2}}, \quad x \geq p-J \quad P(x) = he^{\frac{J(2x-2p+J)}{2\sigma^2}}, \quad x < p-J \quad (2.14)$$

The function is Gaussian for $x \geq p-J$ and has a lower exponential tail smoothly joined at $(p-J)$. A similar higher exponential tail may be used for peaks broadened by pile-up.

Moreover, since the full energy peaks rest on a background Compton continuum, this continuum must be subtracted from the gross peak area in order to get correct peak area. A large number of analytical functions representing this spectral background are available. Generally a linear function approximates the background sufficiently well unless there is a Compton edge in that region. In PHAST, a polynomial background function is used to represent the background.

$$B(x) = a_0 + a_1x + a_2x^2 \quad (2.15)$$

So the function fitted to a group of L peaks is

$$F(x) = B(x) + \sum_l P_l(x), \quad l=1 \text{ to } L \quad (2.16)$$

Also an option for addition of a step component corresponding to each peak is added to the background function to account for the escape of electrons from the sensitive volume of the detector giving rise to a step increase in count downwards from the photopeak energy. An option for selecting such terms is provided in the algorithm. The step increase below a peak at p is proportional to h and described in the program by the following function which takes into account the broadening of the step by the detector resolution function.

$$S(x) = ah \cdot \text{erfc}[(x-p)/(2^{0.5}\sigma)] \quad (2.17)$$

where $\text{erfc}(x)$ is the complementary error function.

When this option is used, the function fitted to a group of L peaks is

$$F(x) = B(x) + \sum_l S_l(x) + \sum_l P_l(x), \quad l=1 \text{ to } L \quad (2.18)$$

Peak Fitting Procedure

Fitting involves minimization of the weighted sum χ^2 of the square of the deviations of the data from the function $F(x)$.

$$\chi^2 = \sum_i [Y_i - F(x_i)]^2 / Y_i \quad (2.19)$$

The summation is performed over all the n data points in the range of the peak group being fitted.

Energy Calibration

The ADC sorts the pulses according to their heights into different channel numbers. The energy calibration relates the channel numbers to the energy deposited by the particle in the detector. The energy calibration of a good spectroscopy system is nearly linear and is given by: $E = mx+b$ where E is the energy deposited in the detector, x is the pulse amplitude, m and b is the slope and intercept respectively. If more number of energies are present then value of m and x can be obtained by least square fitting. This method will distribute the deviations between the actual and computed energies more uniformly and also will reduce the sensitivity of the results to the particular choice of peaks and their location in the spectrum. This is required for the identification of nuclides.

$$m = \frac{n \sum x_i E_i - \sum x_i \sum E_i}{\Delta} \quad (2.20)$$

$$b = \frac{\sum x_i^2 \sum E_i - \sum x_i \sum x_i E_i}{\Delta} \quad (2.21)$$

where $\Delta = n \sum x_i^2 - (\sum x_i)^2$

A linear energy calibration upto second place of decimal is usually adequate for NDA applications. In PHAST, a polynomial function is used:

$$E(x) = a_1 + a_2 \cdot x + a_3 \cdot x^2 \quad (2.22)$$

Shape calibration

Before fitting the gamma rays peaks, it is first necessary to calibrate the peak shape. For this, several single peaks with less error in peak area are fitted to second degree polynomials given as:

$$w(x) = (\alpha + \beta \cdot x)^{1/2} \quad (2.23)$$

where $w(x)$ is the FWHM of the peak at x channel number and α and β are the parameters to be determined for FWHM calibration. FWHM calibration is important for resolving multiple peaks.

Efficiency calibration and activity calculation

For conversion of the measured count rate to the disintegration rate (*dps*) of the radionuclide monitored, it is important to calibrate the system for efficiency. Several fitting functions are available [Willet (1970), Gray and Ahmed (1985), East (1971), McNelles and Campbell (1973), Cox and Manneback (1985), Sanchez-Reyes (1987), Jackel (1987)]. Often two functions are used, one for lower energy (upto 200 keV) and other for higher energy range (above 200 keV). Generally a fourth order polynomial function is sufficient to fit the whole energy range from 80 keV to 2 MeV, as given by:

$$\log \varepsilon_i = \sum_{j=0}^3 a_j (\log E_i)^j \quad (2.24)$$

PHAST needs selection of energies and strength of the standard source in Bq for efficiency calibration.

2.5 MCNP Code

MCNP is a general-purpose Monte Carlo N-Particle code that can be used for neutron, photon, electron, or coupled neutron/photon/electron transport. It takes into account the transport of both primary source electrons as well as secondary electrons created by gamma ray interactions in the medium.

It has been developed and maintained by Los Alamos National Laboratory (LANL) and is undergoing continuous development at LANL and its newer versions are released periodically. In the present work, version 4C [Briesmeister (2000)] has been used though its version 5 has already been released. Version 4 of the MCNP code was released in 1990 and was the first UNIX version of the code.

MCNP code is made up of about 48,000 lines of FORTRAN and 1000 lines of C source coding, including comments. This code is having about 385 subroutines. There is only one source code, which is used for all systems. For neutron transport, all reactions given in a particular cross-section evaluation (such as ENDF/B-VI) are accounted. For photon transport, the code takes into account photoelectric absorption, with the possibility of K- and L-shell fluorescent emission or Auger electron, coherent and incoherent scattering and pair production with the emission of annihilation radiation, and bremsstrahlung. For electrons, a continuous slowing down model is used that includes positrons, K X-rays, and bremsstrahlung but does not include external or self-induced fields. The neutron energy regime is from 10^{-11} MeV to 20 MeV, and the photon and electron energy regimes are from 1 keV to 1000 MeV.

In MCNP, a particle (neutron, photon or an electron) is randomly generated in the source volume and the path of the particle is tracked from its point of origin in the source to the

point of its complete absorption in the detector or upto its point of escape from the detector. Along the track of the particle, the distance between two interactions and the type of interaction that a particle undergoes are taken care randomly by its mean free path and the relative probabilities of the different interactions ultimately related to the cross-sections of the processes in question. In this way a large number of particles are generated and ultimate result is given as the average of all the successes. Depending on the number of particles generated, the error can be as small as desired by the user, given sufficient time to complete the calculation. For example, consider the case of a photon of energy E emitted from a source placed on the detector surface as shown in Figure 2.9. Half of the photons emitted by the source will enter the detector at all possible angles from 0 to π with respect to the detector axis. The photons while traveling through the detector may or may not interact with the detector material. Whether an interaction will take place or not and the distance between two interactions will be governed by the mean free path ($\lambda = 1/\mu$, where μ is the linear attenuation coefficient of the medium at E) of the photon in the detector material. Moreover, whether the particle will interact by a photoelectric absorption, Compton scattering or a pair production will depend upon the relative cross-sections of the three processes. If photoelectric absorption takes place then the particle will deposit its full energy in the detector in one event only and the particle will be tracked upto that point. But if Compton scattering or pair production takes place, then there is a probability of photon to escape from the detector. Then the particle will be tracked to the point of its last interaction.

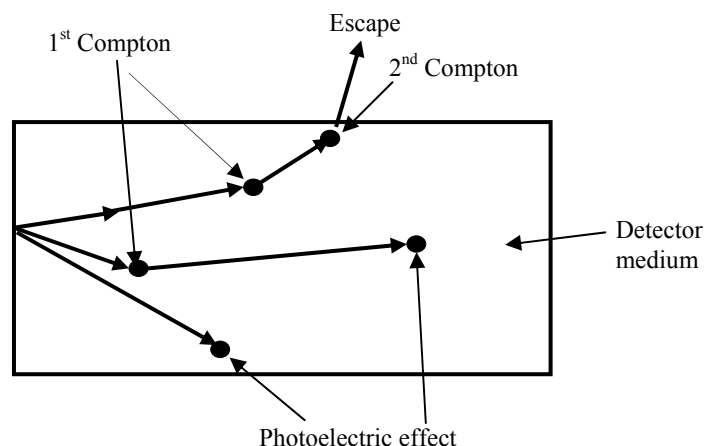


Figure 2.9 Schematic representation of interaction processes for a photon trajectory in a detector medium.

MCNP is a very versatile and powerful transport code, and can model virtually any kind of geometry imaginable. A great advantage of MCNP is that one can vary the geometry of an experimental set-up as many times as needed without having to physically reproduce each change in the laboratory. This saves considerable expense and time by preventing to build and calibrate intermediate designs along the way. Specific areas of application include, but are not limited to, radiation protection and dosimetry, radiation shielding, radiography, medical physics, nuclear criticality safety, detector design and analysis, nuclear oil well logging, accelerator target design, fission and fusion reactor design, decontamination and decommissioning. Also, the MCNP code is commonly used in support of the design and calibration of NDA systems to be used for different applications such as for nuclear material safeguards applications [Weber (2006)]. The simulation can be applied to a range of detectors (high purity germanium detector in the case of gamma spectrometry, ^3He detectors in the case of neutron counting devices), used

with a variety of radioactive sources including containers holding nuclear materials and drums containing neutron- and gamma-emitting waste.

Implementation of a Monte Carlo computational code requires the preparation of an input file which depends upon the problem dealt with. The detail of the input file is given in the following section.

2.5.1 Structure of the MCNP Input File

In the first step, an input file has to be created that describes the geometry of the system in three dimensions, and gives the description of materials including their densities, the location and characteristics of the emitting source, the type of results desired (given in terms of tallies) and variance reduction techniques to be used to improve efficiency of calculations. The geometry of MCNP treats an arbitrary three-dimensional configuration in user defined Cartesian co-ordinate system.

The input file has the following general form:

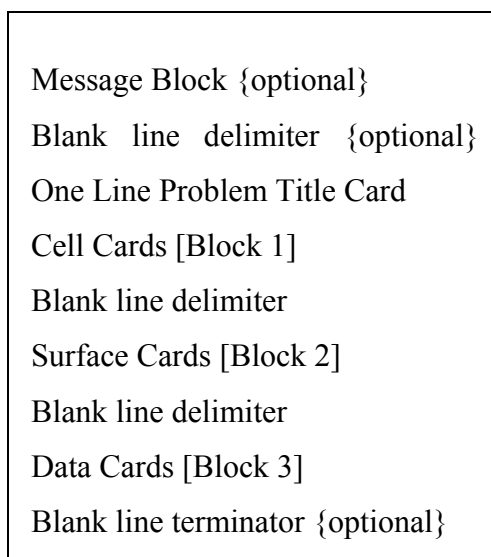


Figure 2.10 General structure of a MCNP input file.

Some of the important points to remember while making an input file are:

- (i) The units to be used while giving an input in MCNP are: length in cm, energy in MeV, atomic densities in units of atoms/barn-cm and mass densities in g/cm^3 . The output is also obtained in these units.
- (ii) Characters written after 80 columns in a line are not read by MCNP while executing a file.
- (iii) If the number of characters is more than 80, then it can be continued to the next line by using an $\&$ sign.
- (iv) MCNP is not case sensitive.
- (v) Anything that follows the $\$$ is interpreted as a comment.
- (vi) Blank lines are used as delimiters and as an optional terminator.

In MCNP, geometry of the concerned problem is treated primarily in terms of regions or volumes bounded by first and second degree surfaces defined with the help of Boolean operators. Geometry of the system is defined by defining cells and surfaces. As seen from Figure 2.10, the input file can be divided into four cards:

(I) Title Card **(II)** Cell Card **(III)** Surface Card **(IV)** Data Card.

The cell and surface card combines to give the complete geometry specification of the problem, while the data card carries the information about materials and selection of cross-section evaluation. Source specification inputs and the required tally types are also given in the data card. Each card is separated by a blank line. These cards have been discussed in details in the following sections.

(I) Title Card

This card gives the title of the problem in one line. It can contain any information you desire but usually contain information describing the particular problem (or can even be blank). The first line in the input file is reserved for this card if there is no message block.

(II) Cell Card

A cell is a region bounded by the surfaces. The full geometry of the concerned problem is divided into a certain number of cells. Each cell is described by a cell number, material number, and material density followed by a list of signed surfaces that bound the cell. Cells are defined by intersections or unions of surfaces defined in the surface card. Intersection operator is simply the blank space while a union operator is defined by ‘.’ sign between the two surfaces. The union and the intersection operators can be understood by considering a pair of concentric circles (with surfaces defined as 1 and 2) as shown in Figure 2.11.

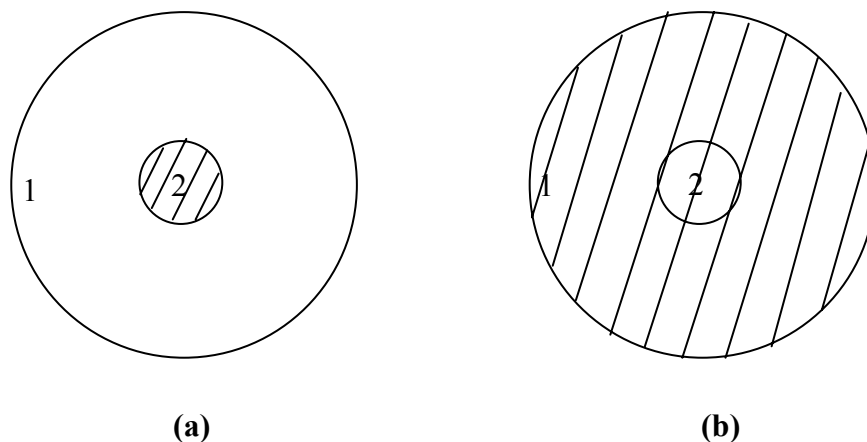


Figure 2.11 Intersection **(a)** and union **(b)** of two surfaces 1 & 2.

The region that belongs to both 1 and 2 is called the intersection of 1 and 2 (i.e. $1 \cap 2$, shown as the lined area in Figure 2.11(a). The region containing points that belong to 1 alone or to 2 alone or to both 1 and 2 is called the union of 1 and 2 (i.e. $1 \cup 2$, shown as the lined area in the Figure 2.11(b). Unions and intersections of geometric surfaces can be used in a combined way to define a cell. Note that a parenthesis is equivalent to a space and signifies an intersection. Apart from this one more Boolean operator is used i.e. NOT denoted by '#'. It acts as a complementary operator. For example # (1:2) represents all space outside the union of 1 and 2. If a cell is defined by only intersections, then all the points within a cell should have same sense (either +ve or -ve) with respect to a given bounding surface. A cell card consists of the cell number, material number, and material density in sequential way separated by spaces, followed by a complete specification of the geometry of the cell. The cell number must begin in columns 1-5. The specification includes a list of signed surfaces bounding the cell where the sign denotes the sense of the regions defined by the surfaces. A void cell (eg. universe) is defined by giving the material number and material density by a zero. The blank line terminates the cell card of the input file. It is always better to define a large number of simple cells rather than defining few complicated cells.

Form of a cell card: cn mn md geom params

cn = cell number.

mn = material number (0 if the cell is a void).

md = cell material density (absent if the cell is a void).

geom = specification of the geometry of the cell. It consists of signed surface numbers and Boolean operators that specify how the regions bounded by the surfaces are to be combined.

params = optional specification of cell parameters by entries in the keyword.

(III) Surface Card

A surface can be defined in two ways in MCNP: **(1)** by specifying known geometrical points on a surface that is rotationally symmetric about a co-ordinate axis, or **(2)** by supplying the appropriate coefficients needed to satisfy the surface equation. The former method can be used only if one is setting up geometry from something like a blueprint where one knows the co-ordinates of intersections of surfaces or points on the surfaces. In the latter method, a surface is defined using one of the surface-type mnemonics as given in Table 2.1 and calculating the appropriate coefficients needed to satisfy the surface equation. In a surface card, the surface number, alphabetic mnemonic indicating the surface type, numerical coefficients of the equation defining the surface are given in the sequential order. The surface number must begin in columns 1-5 and not exceed 5 digits.

Form of a surface card: $sn \quad n \quad a \quad cf$

sn = surface number

n = required only when co-ordinate transformation is there.

a = equation mnemonic from Table 2.1

cf = list of coefficients of the equation describing the surface.

Table 2.1 Specifications of a surface in MCNP.

Mnemonic*	Description	Equation	Card entries required
P	General	$Ax + By + Cz - D = 0$	ABCD
PX	Normal to x axis	$x - D = 0$	D
PY	Normal to y axis	$y - D = 0$	D
PZ	Normal to z axis	$z - D = 0$	D
SO	Centered at origin	$x^2 + y^2 + z^2 - R^2 = 0$	R
S	General	$(x - \bar{x})^2 + (y - \bar{y})^2 + (z - \bar{z})^2 - R^2 = 0$	$\bar{x} \bar{y} \bar{z} R$
SX	Centered on x axis	$x^2 + (y - \bar{y})^2 + (z - \bar{z})^2 - R^2 = 0$	$\bar{x} R$
SY	Centered on y axis	$(x - \bar{x})^2 + y^2 + (z - \bar{z})^2 - R^2 = 0$	$\bar{y} R$
SZ	Centered on z axis	$(x - \bar{x})^2 + (y - \bar{y})^2 + z^2 - R^2 = 0$	$\bar{z} R$
C/X	Parallel to x axis	$(y - \bar{y})^2 + (z - \bar{z})^2 - R^2 = 0$	$\bar{y} \bar{z} R$
C/Y	Parallel to x axis	$(x - \bar{x})^2 + (z - \bar{z})^2 - R^2 = 0$	$\bar{x} \bar{z} R$
C/Z	Parallel to x axis	$(x - \bar{x})^2 + (y - \bar{y})^2 - R^2 = 0$	$\bar{x} \bar{y} R$
CX	On x axis	$y^2 + z^2 - R^2 = 0$	R
CY	On y axis	$x^2 + z^2 - R^2 = 0$	R
CZ	On z axis	$x^2 + y^2 - R^2 = 0$	R

*P, S and C indicates the surface type to be plane, sphere and cylinder respectively

Every surface has a “positive” side and a “negative” side. A point (x, y, z) is defined as having positive sense with respect to a surface when the expression for that surface evaluated at (x, y, z) is positive and vice versa. For example, if a cylinder (with its axis along the x-axis) is a surface then from Table 2.1, the equation for the cylinder will be:

$$y^2 + z^2 - R^2 = 0 \quad (2.25)$$

This surface can be divided into two regions: one outside it and the other inside it. When a point (x, y, z) lies outside the cylinder, then the LHS of the equation at (x, y, z) will be positive, therefore the point (x, y, z) will have a positive sense with respect to this surface and when this point lies inside the cylinder, the LHS of the equation at (x, y, z) will be negative, therefore the point (x, y, z) will have a negative sense with respect to this surface

If this cylinder has a radius of 2.5 cm with its axis along x-axis and is the 3rd surface in the sequence then in the surface card it will appear as

3 CX 2.5

(IV) Data Card

This card specifies the information about the source and the material involved in the problem. This card itself can be divided into a number of cards given below:

1. MODE Card

It gives the mode of transport of the particle in the study. It can be single transport mode like a neutron or a photon or an electron, or it may be coupled. Different transport modes and their corresponding mnemonics are given below.

N – neutron transport only

P – photon transport only

E – electron transport only

$P E$ – photon and electron transport

$N P$ – neutron and neutron induced photon transport

$N P E$ – neutron, neutron induced photon and electron transport

If the MODE card is omitted, mode N is assumed.

2. Cell and Surface Parameter Cards

It includes the *IMP*: particle mnemonic (eg. N or P) card giving the relative cell and surface importances in the sample problem. It is represented as *IMP:N*, *IMP:P*, *IMP:NP*, *IMP:PE*, *IMP:NPE* etc.

For eg. *IMP:N 1*

This means that the neutron data (it can be flux, current etc.) in the cell 1 is the desired output.

3. Source Specification Cards

It is denoted as *SDEF* and gives the specifications of the source. Some of the parameters defined in this card are:

POS = x y z (default is 0 0 0);

CEL = starting cell number (not required for a point source);

ERG = starting energy (default is 14 MeV);

WGT = starting weight (default is 1);

TME = time (default is 0);

PAR = source particle type 1 for N, N P, N P E; 2 for P, P E; 3 for E.

4. Tally Specification Cards

Since MCNP can be used for a variety of purposes, depending upon the type of output required (like current across a surface, flux at a point etc.), different tally cards are used.

The different types of tally cards and their corresponding descriptions are given below.

Tally type	Description
$F1$	Surface current
$F2$	Surface flux
$F4$	Track length estimate of cell flux
$F5$	Flux at a point or ring detector
$F6$	Track length estimate of energy deposition
$F7$	Track length estimate of fission energy deposition
$F8$	Energy distribution of pulses created in a detector

An $F8$ tally, known as a pulse height tally, was used in all models. This tally records the energy deposited in a cell by each source particle and its secondary particles. A Gaussian Energy Broadening (GEB) treatment was used to simulate the resolution of the detector. This treatment uses three parameters to define the resolution of the detector at a specific energy by:

$$FWHM = a + b\sqrt{E + cE^2} \quad (2.26)$$

E = the peak energy (MeV),

$FWHM$ = the full width at half maximum of a Gaussian resolution function centered at E ,

a, b, c = parameters whose values are required as an input and are generally obtained by using the experimental $FWHM$ calibration curve.

5. Materials Specification Card

This card gives the details of the materials i.e. the isotopes present and their fractions in a given material. The general format is

Mm ZAID1 fraction1

Mm+1 ZAID2 fraction2

where m denotes the material number and the material is identified by the number $ZAID$ with the form $ZZZAAA.nnX$, where ZZZ and AAA gives the Z and A of the isotope. Conventionally, nn and X are the cross-section evaluation identifier; if blank or zero, a default cross-section evaluation will be used, and class of data respectively, C is continuous energy, D is discrete reaction, T is thermal, Y is dosimetry, P is photon, E is electron and M is multigroup. Fraction gives the fraction of the isotope present in the material.

A typical input file has been given in the Appendix I of this thesis.

Hybrid Monte Carlo Method for Standard Source Geometry

- 3.1 Introduction
- 3.2 Attenuation Correction Factor
 - 3.2.1 *Measurement of linear attenuation coefficient (μ)*
 - 3.2.2 *Calculation of attenuation correction factor (k_{att})*
 - 3.2.3 *Aim of this work*
- 3.3 Hybrid Monte Carlo Method
- 3.4 Programs
 - 3.4.1 *Cylindrical geometry*
 - 3.4.2 *Box geometry*
 - 3.4.3 *Spherical geometry*
 - 3.4.4 *Disc geometry*
- 3.5 Validation of the Hybrid Monte Carlo approach
 - 3.5.1 *Theoretical validation*
 - 3.5.2 *Experimental validation*
- 3.6 Conclusion

3.1 Introduction

As discussed in Chapter 1, the gamma rays while passing through a medium may interact by any of the three interaction modes and may be scattered or absorbed in the medium. This can be more clearly understood by considering a cylindrical sample placed on the detector surface as shown in Figure 3.1. Due to the voluminous nature of the sample, a fraction of the photons generated in the sample volume may interact in the sample itself as shown in the figure. This results in loss of photons in the sample and hence reduction in the number of photons that would have reached the detector in the absence of such interaction. The probability of such interaction becomes important as the sample becomes more and more voluminous or the density of the sample increases. As emphasized in Chapter 1, the net effect is the loss of proportionality between the measured count rate of a radionuclide and its amount in the sample. The use of calibration standard is difficult due to diversity of sample matrix encountered in NDA [Reilly et al. (1991)] and the problem can only be solved by correcting the measured count rate for self-attenuation as given in equation 1.7.

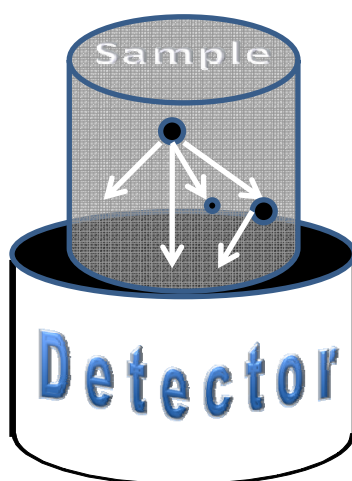


Figure 3.1 Possible gamma ray interactions within the sample volume before reaching the detector.

3.2 Attenuation Correction Factor

The attenuation correction factor (k_{att}) is defined as:

$$k_{att} = \frac{RR(\mu = 0, \text{specified shape})}{RR(\mu \neq 0, \text{real shape})} \quad (3.1)$$

where $RR(\mu = 0, \text{specified shape})$ is the count rate for totally non-attenuating ($\mu = 0$) sample having a specified shape. This specified shape may not necessarily be the actual shape of the sample and can be approximated to a simplified shape like a point or a line depending upon the sample-detector configuration. $RR(\mu \neq 0, \text{real shape})$ is the measured count rate for the sample. For computational purpose, the k_{att} , as defined above, can be written as [Parker (1991)]:

$$k_{att} = \frac{\int_v \rho I \varepsilon(r) dV}{\int_v \rho I \varepsilon(r) \exp(-\mu t(r)) dV} \quad (3.2)$$

where ρ = spatial density of the isotope being assayed (g/cm^3),

I = emission rate of the assayed gamma ray ($\gamma/\text{g-s}$),

ε = absolute full energy detection efficiency,

μ = linear attenuation coefficient of the sample,

and t = distance the gamma ray travels within the sample.

The integration is to be performed over the volume of the sample. From equation 3.2, it can be seen that, for obtaining k_{att} , linear attenuation coefficient of sample matrix is required as an input. The measurement of attenuation correction factor is a two step process. First step is to obtain linear attenuation coefficient of the sample under study.

The next step is to choose an appropriate model to obtain the sample-detector geometry dependent attenuation correction factor. The two steps involved are discussed in detail below.

3.2.1 Measurement of Linear Attenuation Coefficient (μ)

The linear attenuation coefficient (μ) describes the fraction of a beam of X-rays or gamma rays that are absorbed or scattered per unit thickness of the absorber. For a narrow beam of monoenergetic photons (Figure 3.2), the change in beam intensity ($dI(x)$) while passing through a small thickness (dx) of the absorber can be expressed as:

$$dI(x) = -I(x)n\sigma dx \quad (3.3)$$

Where, n is the number of atoms/cm³ and σ is the proportionality constant and is a measure of the probability of gamma ray interaction per absorber atom.

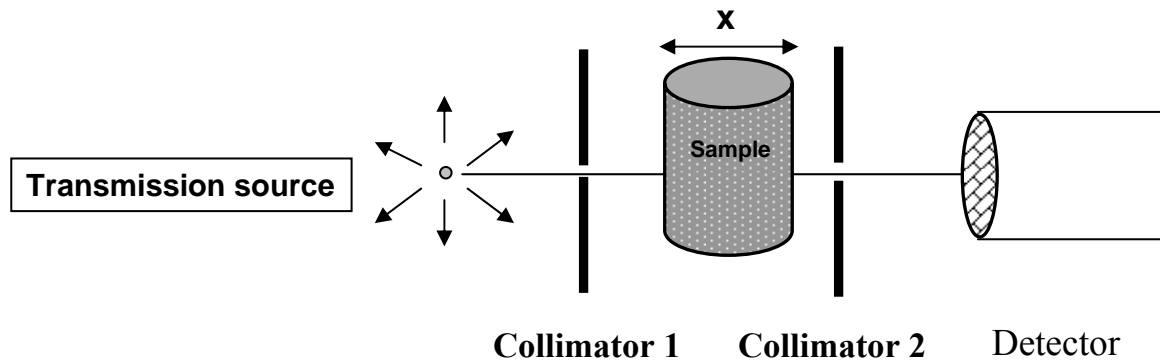


Figure 3.2 Transmission of a gamma ray through an attenuating medium present in between the source and the detector.

On integrating this equation over the thickness of the absorber,

$$I = I_o \exp(-n\sigma x) \quad (3.4)$$

where, I and I_0 are the intensities of gamma ray with and without the absorber, x is the distance traversed by the gamma ray through the absorber. The number of atoms/cm³ (n) and the proportionality constant (σ) are usually combined to yield the linear attenuation coefficient (μ). Therefore the equation becomes:

$$I = I_0 \exp(-\mu x) \quad (3.5)$$

The linear attenuation coefficient determines the mean free path (λ) of a photon in a medium i.e. $\lambda = 1/\mu$ where, λ characterizes the average distance a photon will traverse before undergoing a collision in a medium. If there is a precise knowledge of the composition and density of the sample, the linear attenuation coefficient of the sample can be obtained theoretically by taking the literature mass attenuation coefficient (μ_m) at the monitored energy for the given medium. The μ_m values for different matrices have been compiled in Hubbell (1982). Due to the diversity of samples encountered in NDA work, these details of sample composition and density may not be always available. Thus it is a common practice to measure μ experimentally by transmission technique. The experimental set-up for this is already shown in Figure 3.2. Here, the transmission of a collimated beam of gamma ray from an external source is measured with and without the sample. Then, the linear attenuation coefficient is obtained using equation 3.5. The choice of external source is important and depends upon the radionuclides monitored. In principle, one should use a transmission source that emits a gamma ray of energy as close as possible to the energy of the gamma ray emitted by the sample and should be preferably monoenergetic.

3.2.1 Calculation of Attenuation Correction Factor (k_{att})

Once the μ of the sample is known, one has to choose an appropriate model to obtain the sample-detector geometry dependent attenuation correction factor. This is done by simplifying the general equation 3.2. The detector in this case is considered to be a point detector. For homogeneous sample, the factor ρI will remain constant in both numerator and denominator and will cancel out. Since the parameters ε and t are function of the coordinate of the point at which gamma ray originates within the sample, they cannot be taken out of the integral and hence they will not cancel out. For majority of geometrical configurations, the integrals cannot be evaluated analytically, and numerical integration is required. There is extensive literature on evaluation of k_{att} for different sample shapes [Moens et al. (1981), Debertin and Jianping (1989), Chilton et al. (1984), Croft (1993), Dixon (1951), Dickens (1972)]. Based on sample-to-detector distance, two general approaches have evolved.

(I) Far-field Geometry

A great simplification occurs, if ε is considered to be independent of position within the sample. This idealization is practically realized if the distance between sample and detector is large enough so that the gamma rays reaching the detector are essentially parallel and ε can be assumed to be independent of point of origin of the gamma ray within the sample and can be taken out of integrals. Then ε in the numerator and denominator get cancelled and the integration can be performed over the sample volume. This makes the integrals relatively easy to compute. In such a case, the size of the sample can be considered to be negligible compared to the source-to-detector distance. This

situation is called far-field geometry and k_{att} in such a case becomes independent of the detector size, shape and sample-to-detector distance and is only influenced by the sample characteristics like its size, shape and matrix. For far-field cases, analytical expressions are available in literature for some common sample geometries [Croft et al. (2005)] viz. box-shaped (rectangular parallelepiped), cylindrical [Owen and Fage (1921)] and spherical [Francois (1974), Thirring (1912)].

(II) Near-field Geometry

In practice, it is not always possible to count the sample far away from the detector. For example, in environmental samples, activity is usually low, and the sample is required to be counted close to the detector to maximize the count rate. In such a case, the far-field formulae cannot be applied as they assume detector to be a point detector and ε is assumed to be independent of point of origin of gamma ray in the sample. In literature, separate numerical models are available for calculating attenuation correction factors for the near-field case. These models are based on certain assumptions to simplify the sample-detector geometry. For example, in k_{att} calculation for cylindrical samples in near-field geometry [Parker (1991)], only the circular cross-section of the sample is considered and the detector is assumed to be a point detector. Moreover, there are restrictions about sample-detector dimensions.

Gunnink and Niday (1972) and Cline (1978) developed semi-empirical methods to find the peak efficiency of co-axial Ge(Li) detectors including implicit or explicit corrections for gamma ray attenuation. Points, disks, cylindrical and spherical sources were considered. These techniques, however, are based on approximating mathematical

models, representing the detector [Gunnink and Niday (1972), Cline (1978)] and the source [Gunnink and Niday (1972)] as physical points. Aguiar et al. (2006) and Aguiar (2008) also proposed an analytical approach for cylindrical geometry to get full energy peak efficiency taking into account the self-attenuation in the sample. The approach assumes detector as a point inside the detector volume with its position determined empirically using point sources.

A semi-empirical procedure to calculate absolute detector efficiency for a point, disc and cylindrical samples has also been described by Moens et al. (1981). The method takes care of gamma ray attenuation within the sample and in any interjacent absorbing layer. The method has been devised for cylindrical geometry including co-axial Ge(Li) detectors and is free of any simplification in the sample-detector geometry. The peak efficiency of any investigated configuration ($\varepsilon_{p,x}$) is calculated from the measured efficiency of a reference point source ($\varepsilon_{p,ref}$) positioned on the detector axis at large distance from the detector using the formula:

$$\varepsilon_{p,x} = \varepsilon_{p,ref} \frac{\bar{\Omega}_x}{\bar{\Omega}_{ref}} \quad (3.6)$$

where $\bar{\Omega}_{ref}$ and $\bar{\Omega}_x$ are the effective solid angles of the point source and the sample respectively. $\bar{\Omega}_{ref}$ takes into account the attenuation within the sample. The effective solid angle is related to the peak efficiency (ε_p) as:

$$\varepsilon_p = \frac{1}{4\pi} \frac{P}{T} \bar{\Omega} \quad (3.7)$$

where P/T is peak to total ratio for the detector for the given gamma ray. The method involves numerical integration for the evaluation of $\bar{\Omega}_i$, and requires detector dimensions

as input. Debertin and Jianping (1989) proposed a point detector model for the calculation of detector efficiency from attenuating samples.

Alternative to all these approaches is a full scale Monte Carlo calculation of k_{att} [Sima and Arnold (1996), Sima (1996), Pérez-Moreno et al. (2002), Vargas et al. (2002)]. The advantage of this approach is that it can reproduce any sample-detector geometry and minimize experimental work. The limitation of this method is that it can be used only when the bulk density and the elemental composition of the samples are known accurately. It also requires a detailed description of sample-detector geometry. Monte Carlo calculation of k_{att} is computationally very time consuming.

Recently, a hybrid Monte Carlo method has been used to calculate detector efficiency [Yalcin et al. (2007)] and self-attenuation correction factors [Badawy et al. (2000)] where analytical expressions are used in Monte Carlo simulation. This leads to considerable reduction in computation time. García-Talavera and Peña (2004) also proposed a Hybrid approach that combines the experimental measurements and MC simulations can be applied to any unknown composition.

3.2.3 Aim of this Work

From the above discussion, it can be concluded that although there are several approaches available in the literature but none is valid at all sample-detector geometries. Also it is not easy to decide which formula to use as it not only depends upon the sample-to-detector distance but also on the sample-detector dimensions. For eg. a distance of 10 cm may be a far-field for 20 ml vial but not for a 200 L drum. Therefore, in spite of so many approaches available in literature, for laboratories where attenuation correction is a part

of routine analysis, a simple, convenient method is still very much required which can be applied without bothering much about sample-detector geometry.

In this work, a Hybrid Monte Carlo (HMC) method has been developed for obtaining attenuation correction factors. This method avoids any simplified assumption used for near or far-field geometry formulae. Moreover, unlike the far-field and near-field approaches, the detector is not considered to be a point detector. This method does not require detailed information about detector dimensions excepting the radius of the detector crystal (considered to be a cylinder). In the present work, this method has been used to obtain attenuation correction factors for the three sample geometries i.e. cylinder, sphere and box at different sample-to-detector distances as a function of transmittance and these results are compared with the analytical expressions available in the literature. MCNP calculations [Briesmeister (2000)] have also been performed to validate the prediction of our calculation for samples of varied transmittance and sample-to-detector distance. This method has been further validated by comparing the results of calculation with the experimentally obtained k_{att} 's. The experiment was done for three sample geometries – 1) cylindrical sample with axis collinear with the detector axis (disc geometry), 2) cylindrical sample with axis perpendicular to detector axis (cylindrical geometry) and 3) box shaped sample. In all the cases, the centre of gravity of the sample was fixed on the detector axis. All the three geometrical set-ups are shown in Figure 3.3.

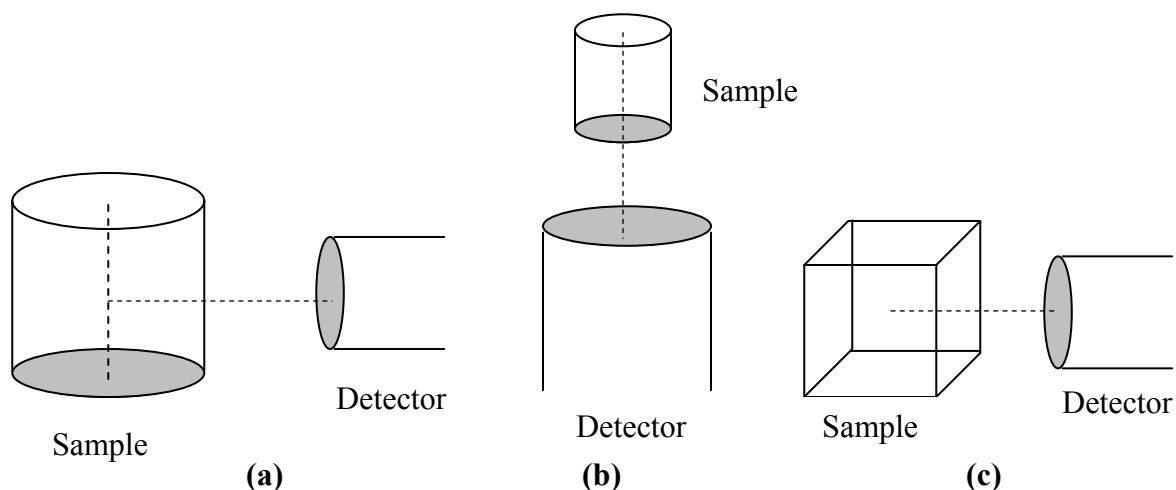


Figure 3.3 The geometrical arrangement of the sample and detector (a) Cylindrical geometry (b) Disc geometry and (c) Box geometry.

3.3 Hybrid Monte Carlo Method

In equation 3.2, as already emphasized above, all the factors cancel out except ε and the exponential term. As mentioned before, ε is the efficiency of the detector for particular sample-detector geometry and so is inversely proportional to $1/r^2$ where r is the distance the gamma ray travels from the point of origin in the sample to the detector surface. So, attenuation correction factor for a particular path followed by a gamma ray can be simplified as:

$$k_{att} = \frac{1/r^2}{\exp(-\mu t)/r^2} \quad (3.8)$$

where t is the distance the gamma ray travels in the sample. The exponential term in the denominator corrects for the gamma ray attenuation in the sample. Both ε and t will vary depending upon the point of origin of the gamma ray in the sample and also on its path followed to reach the detector. In the case of an attenuating container wall, an additional

factor in equation 3.8 in the exponential will come ($\mu_c t_c$, where μ_c and t_c are the linear attenuation coefficient and path length of the gamma ray in the sample wall respectively). As demonstrated below, t_c can be found out by the same procedure as t . Two representative paths of gamma ray originating in a cylindrical sample whose axis is perpendicular to the detector axis are shown in Figure 3.4. Consider the origin is fixed at the centre of gravity of the sample, which lie on the detector and sample axis. Suppose a random point is generated within the sample having co-ordinate (a, b, c) and another random point $(a1, d, c1)$ on the detector surface which is at a distance d from the origin. Suppose the line connecting (a, b, c) and $(a1, d, c1)$ intersect the sample cylinder at (x, y, z) . Then r and t for this representative path is given by:

$$r = \sqrt{(a1-a)^2 + (d-b)^2 + (c1-c)^2} \quad (3.9)$$

$$t = \sqrt{(x-a)^2 + (y-b)^2 + (z-c)^2} \quad (3.10)$$

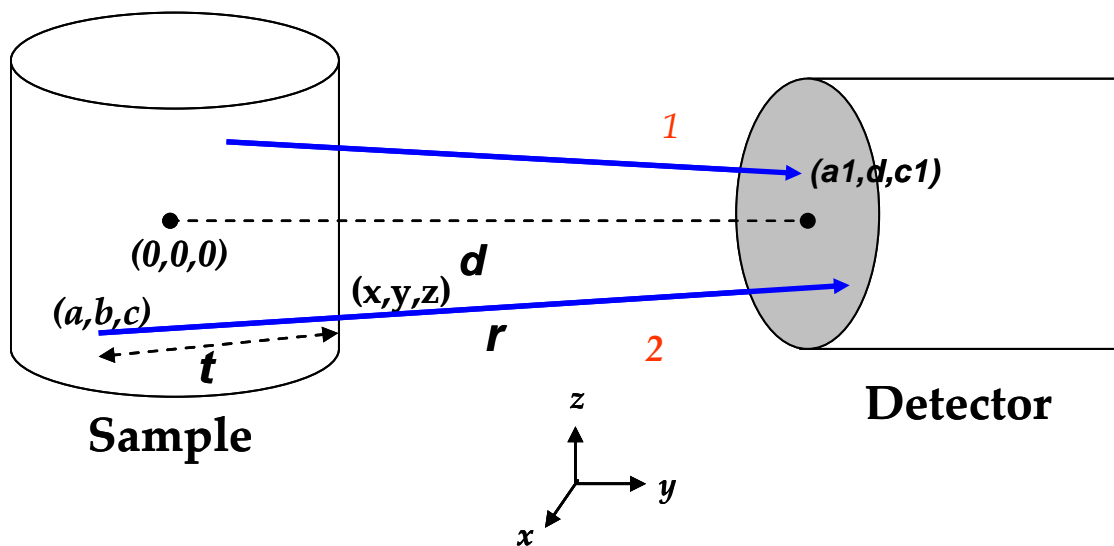


Figure 3.4 Representative paths of two gamma rays from sample to the detector surface.

From equation 3.9, r can be calculated since the point of gamma ray origin and the point at which it reaches the detector is known. But for calculating t , the co-ordinate of the point of intersection (x, y, z) of the line connecting (a, b, c) and $(a1, d, c1)$ and the sample cylinder need to be known. The procedure for calculating (x, y, z) is given below. The equation of the straight line joining (a, b, c) , (x, y, z) and $(a1, d, c1)$ is given by:

$$\frac{x-a}{a1-a} = \frac{y-b}{d-b} = \frac{z-c}{c1-c} \quad (3.11)$$

The value of (x, y, z) can be obtained from the point of intersection of this straight line and the circle defined by the equation

$$x^2 + y^2 = r_{sample}^2 \quad (3.12)$$

where r_{sample} is the radius of the cylindrical sample. Similarly, r and t can be obtained for any pair of points lying on the detector surface and in the sample volume. In the present numerical approach, a large number of pair of random points are generated which are lying on the detector surface and in the sample volume, the actual k_{att} for the sample will be given by the following equation:

$$k_{att} = \frac{\frac{1}{n} \sum_{i=1}^n 1/r_i^2}{\frac{1}{n} \sum_{i=1}^n \exp(-\mu t_i)/r_i^2} \quad (3.13)$$

$$= \frac{\langle 1/r_i^2 \rangle}{\langle \exp(-\mu t_i)/r_i^2 \rangle} \quad (3.14)$$

where $\langle \rangle$ sign represents the average of the quantity concerned. The approach is hybrid since Monte Carlo principle is combined with the analytical method.

3.4 PROGRAMS

In order to calculate attenuation correction factors, separate FORTRAN programs were written for different sample geometries. The description of the programs written for common sample geometries is given below:

3.4.1 Cylindrical Geometry

For cylindrical geometry, the attenuation correction program 'CYL.FOR' is given as program 1 in the Appendix II of this thesis. In this program, the linear attenuation coefficient (μ or μ) is kept fixed and transmittance of the gamma ray is given as an input in 'transm.txt'. The input of the program can be changed as required. An example of the input file is given in the input as Input 1 in the Appendix II of this thesis. This file gives the list of transmittance of the gamma ray for which k_{att} values are to be calculated. The radius of the cylindrical sample corresponding to the given transmittance values given are calculated in the program itself. The diameter of the detector surface, which is an input in the calculations, was given as 5 cm. This corresponds to the manufacturer supplied diameter of the detector used in the experiments. The length of the crystal does not enter in the calculations. The function 'aphasa' is used to generate random numbers in both the sample volume and on the detector surface. For example, for a cylindrical sample (with radius and half-height of the cylinder as f and h respectively), three random

numbers (a, b, c) are first generated within a cuboid of dimensions $2f \times 2f \times 2h$. Then all the points which lie outside the cylinder are rejected by imposing the condition:

$$a^2 + b^2 \leq f^2 \quad (3.15)$$

Similarly, to generate random point on the circular detector surface of radius g , first random point is generated in a square of length g and then all the random points which lie outside the circle of radius g are rejected. These co-ordinates are then used to get the distance traveled by the gamma ray to reach the detector as given by equation 3.9. These co-ordinates are also then used to find the intersection point of the gamma ray with the sample surface i.e. (x, y, z) as given in Section 3.3 of this thesis. Once (x, y, z) is known then the distance traveled by the gamma ray in the sample (t) is calculated using equation 3.10. These are then used to get k_{att} . The output is stored in the file '**cylinder.out**'. The calculations were performed by generating approximately 10^5 particles, using a desktop PC. This program was run separately for different sample-to-detector distances.

3.4.2 Box Geometry

For a box shaped sample ($2f \times 2f \times 2f$), random points were generated within the dimension of the box. No additional conditions are required. The distance traveled by the gamma ray within the sample before reaching the detector (t) can be obtained by solving Eq. (3.11) and the equation defining the plane surface of the box from which the gamma ray is emerging:

$$y = f \quad (3.16)$$

k_{att} can then be obtained from the equation 3.14. The FORTRAN program for box shaped sample 'BOX.FOR' is given as program 2 in Appendix II. The symbols and

functions used in this program are similar to those used in program 1. The input and the output files are '**transm.txt**' and '**box.out**' respectively. Here also the attenuation correction factors have been calculated as a function of transmittance and sample-to-detector distances. The transmissions were varied by keeping the linear attenuation coefficient (μ) constant and varying the half-thickness of the box (*yy or f*).

3.4.3 Spherical Geometry

The random points in a spherical sample of radius f , are generated by first generating random points (a, b, c) within a cube of edge $2f$ and then rejecting all the points which lie outside the sphere. This is accomplished by imposing the following two conditions:

$$a^2 + b^2 \leq f^2 \quad (3.17)$$

$$a^2 + c^2 \leq f^2 \quad (3.18)$$

The distance traveled by the gamma ray to reach the detector is then obtained by using equation 3.9. The distance traveled by the gamma ray within the sample before reaching the detector (t) can be obtained by solving the equation 3.11 and the following equation defining the spherical surface:

$$x^2 + y^2 + z^2 = f^2 \quad (3.19)$$

k_{att} can then be obtained from equation 3.14. The FORTRAN program for spherical sample 'SPHERE.FOR' is given as program 3 in Appendix II. The description of this program is also similar to that of the previous two programs. The input and the output files are '**transm.txt**' and '**sphere.out**' respectively.

3.4.4 Disc Geometry

For the disc geometry, the random points are generated in the sample in a way similar to cylindrical geometry i.e. first random points are generated in a box of same dimensions and then all the points lying outside the disc are rejected by imposing the following condition :

$$a^2 + c^2 \leq f^2 \quad (3.20)$$

where f is the radius of the disc. Then, the distance traveled by the gamma ray within the sample before reaching the detector can be obtained by solving the equation 3.11 and the following equation:

$$y = h \quad (3.21)$$

where h is the half-thickness of the disc. k_{att} can then be obtained from equation 3.14. The FORTRAN program for disc geometry 'DISC.FOR' is given as program 4 in the Appendix II. In this program, proper correction for the gamma rays reaching the detector from the walls of the disc has been incorporated. Here, the diameter of the cylindrical detector was 6 cm which was chosen for the calculations to match with the experimental detector dimensions. Separate runs were taken for each sample-to-detector distance.

3.5 Validation of the Hybrid Monte Carlo Approach

3.5.1 Theoretical Validation

The hybrid Monte Carlo approach was validated by comparing its results with MCNP calculations and geometrical formulae available in literature. The comparison was done at different sample-to-detector distances and for different extents of attenuation. Three most

commonly used sample geometries namely sphere, box and cylindrical were considered. Since the calculation of attenuation correction factor by both the HMC method and far-field and near-field formulae require linear attenuation coefficient as an input, therefore firstly linear attenuation coefficients were measured experimentally.

Measurement of linear attenuation coefficient (μ)

To measure linear attenuation coefficient experimentally, uranium was chosen as the attenuating matrix. This was done owing to the high Z of uranium. The linear attenuation coefficients were obtained for four uranyl nitrate samples (100-390 mg/ml) at the energies of interest. These samples were prepared by dissolving the required amount of U_3O_8 in concentrated nitric acid, followed by dilution with 2M HNO_3 . The μ (cm^{-1}) were then obtained experimentally by transmission measurement of a collimated beam. For this, the transmission source was counted with and without the sample. The schematic of experimental set-up has already been shown in Figure 3.2. The ^{169}Yb was used as the transmission source as it has gamma rays close to the ^{235}U gamma rays used in our measurement. Table 3.1 gives the ^{169}Yb and ^{235}U gamma ray energies monitored. Here, the unattenuated count rate was obtained by replacing the sample with 2M HNO_3 solution.

The transmission curve as a function of gamma ray energy is shown in Figure 3.5. The highlighted points in the figure shows the gamma ray energies of ^{235}U monitored. The transmittance for ^{235}U energies was obtained by linear interpolation between the transmittance for ^{169}Yb energies. The linear attenuation coefficient was then obtained from equation 3.5.

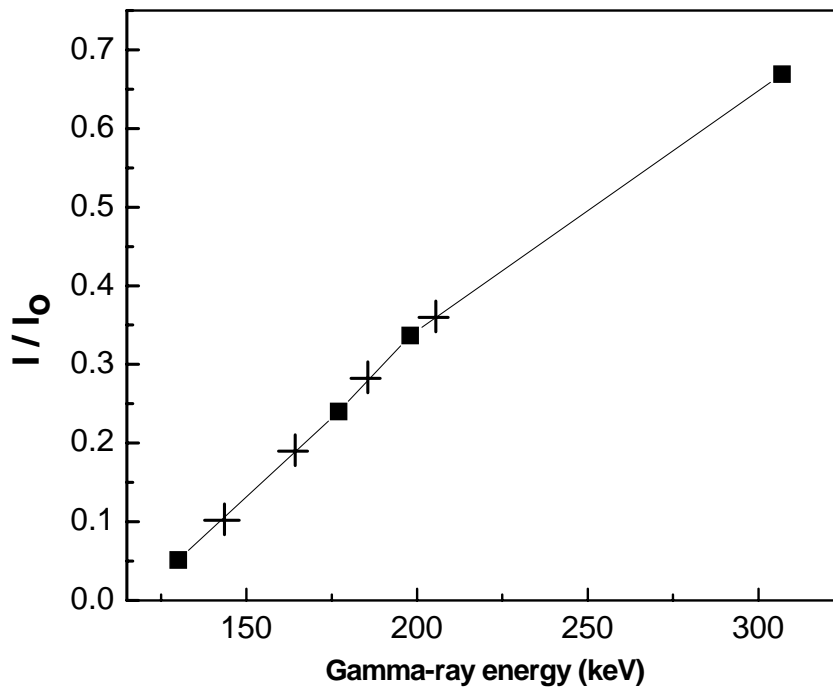


Figure 3.5 Transmission curve as a function of gamma ray energy using ^{169}Yb as transmission source.

Table 3.1 Gamma ray energies of ^{169}Yb and ^{235}U .

Gamma ray energy (keV)	
^{169}Yb	^{235}U
130.5	143.8
177.2	163.4
198.0	185.7
307.7	205.3

Comparison of HMC results with Far-field results

As a first step, all the calculations were done by keeping the sample-to-detector distance sufficiently large so that the results can be compared with the far-field correction factors available in the literature. To calculate attenuation correction factors for a wide range of transmittance, the linear attenuation coefficient was fixed at 0.5 cm^{-1} which corresponds to the value at 186 keV for one of the uranyl nitrate sample. The transmittance was varied by changing the dimension of the sample along the detector axis. For cylinder and sphere, the radius of the sample was changed and for a box, its length was changed. In the case of cylinder, the height was of the order of the diameter of the detector so that the path of the gamma ray reaching the detector from the top or bottom surface could be neglected. But practically, if the height of the sample to be analyzed is such that there is a finite probability of gamma rays reaching the detector from the top or bottom of the sample, then the corrections can be easily incorporated in the required program. Table 3.2 gives the results of the present k_{att} calculations for the three geometries using a sample-to-detector distance of 100 cm. It also gives the corresponding k_{att} values calculated from the following far-field analytical expressions [Parker (1991)]:

$$k_{att(cylinder)} = \frac{1}{2} \frac{\mu D}{[I_1(\mu D) - L_1(\mu D)]} \quad (3.22)$$

$$k_{att(box)} = \frac{\mu x}{[1 - \exp(-\mu x)]} \quad (3.23)$$

$$k_{att(sphere)} = \left(\frac{3/2}{\mu D} \left\{ 1 - \frac{2}{(\mu D)^2} + \exp(-\mu D) \left[\frac{2}{\mu D} + \frac{2}{(\mu D)^2} \right] \right\} \right)^{-1} \quad (3.24)$$

where D is the diameter of the cylinder and sphere, x is the half-thickness of the box, I_1 and L_1 are modified Bessel and modified Struve functions of order 1. The data in Table 3.2 show a good agreement between the present calculations and the literature for all geometries, but deviations upto 5% are observed at very low transmittance. This validates the method of present calculation of k_{att} at far-field geometry.

Table 3.2 Results of k_{att} calculations by the present method and comparison with values available in the literature for samples of different geometries.

T	Cylinder		Box		Sphere	
	k_{att}	k_{att}^*	k_{att}	k_{att}^*	k_{att}	k_{att}^*
0.01	3.74	3.79	4.43	4.65	3.36	3.37
0.09	2.29	2.30	2.60	2.65	2.10	2.11
0.17	1.90	1.91	2.11	2.13	1.78	1.78
0.25	1.68	1.69	1.84	1.85	1.59	1.59
0.33	1.53	1.54	1.65	1.65	1.46	1.46
0.41	1.42	1.42	1.51	1.51	1.36	1.37
0.57	1.25	1.26	1.31	1.31	1.22	1.22
0.73	1.14	1.14	1.17	1.17	1.12	1.12
0.89	1.05	1.05	1.06	1.06	1.04	1.04
0.97	1.01	1.01	1.02	1.02	1.01	1.01

*From Parker (1991)

In order to get an idea about the minimum sample-to-detector distance upto which far-field expressions available in literature can be applied, present calculations for all the

three geometries were performed at varying sample-to-detector distance. These results were compared with the results from literature formula. Figure 3.6(a) shows the ratio of k_{att} obtained by the present calculations to the k_{att} calculated from the far-field expressions at different sample-to-detector distances for cylindrical geometry. The results agree within 2% at almost all transmittance at higher distance (> 50 cm). The deviation starts at lower distance, particularly at lower transmittance. The lower value of k_{att} than predicted by far-field expression is expected at closer distance as the geometric efficiency becomes dependent on the position of emission of gamma ray within the sample.

Comparison of HMC results with MCNP results

In order to further confirm the result of the present calculations, Monte Carlo simulation for the given sample-detector geometry were performed using MCNP code. For this purpose, company supplied dimension of the detector was used. In this case also uranium solution with experimentally determined $\mu = 0.5 \text{ cm}^{-1}$ at 186 keV was chosen as the matrix and its density was given as an input in the calculations. The transmittance of the solution was varied by changing the radius of the cylinder and sphere and length of the box. The unattenuated count rate was obtained by replacing the sample solution by air. The k_{att} was calculated from the ratio of unattenuated to attenuated count rates. The results of the present calculations relative to MCNP calculations for cylindrical geometry are shown in figure 3.6(b). It is observed that the ratio no longer shows the kind of systematic distance dependence as observed in figure 3.6(a). This shows that the result of our calculations is applicable at all sample-to-detector distance. However, the ratio in figure 3.6(b) shows about 10% deviation at lowest transmittance independent of sample-

to-detector distance. This may be due to inherent uncertainty involved in the MCNP calculations.

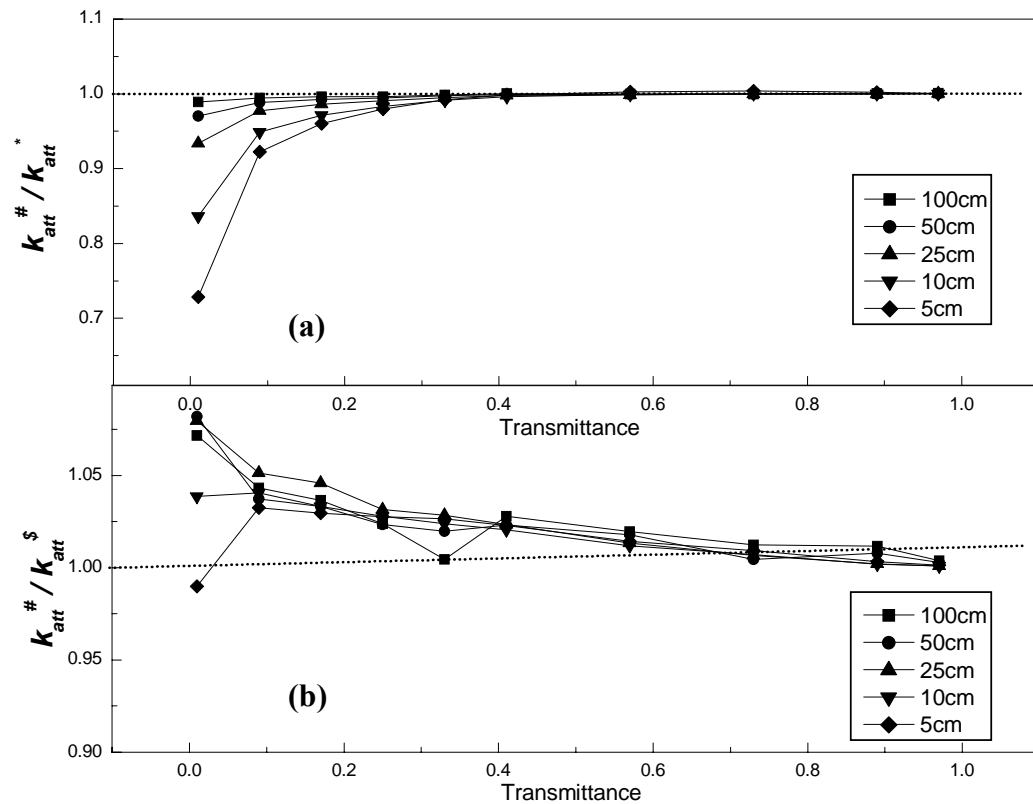


Figure 3.6 Ratio of attenuation correction factors at different distances as a function of transmittance for cylindrical geometry. **(a)** $k_{att}^{\#} / k_{att}^{*}$

(b) $k_{att}^{\#} / k_{att}^{\$}$

Present calculation

\$ MCNP calculation

* From Reilly et al. (1991)

Comparison of HMC results with Near-field results

To see whether the present calculation converges with the prediction of near-field formula, the HMC results along with the far-field and MCNP results, were compared

with the results of near-field expressions (two dimensional model) as given below [Parker (1991)] for cylindrical geometry:

$$k_{att} = \frac{\sum_{m=1}^M \sum_{n=1}^N \Delta A(m,n) / L^2(m,n)}{\sum_{m=1}^M \sum_{n=1}^N \{\exp[-\mu t(m,n)]\} \Delta A(m,n) / L^2(m,n)} \quad (3.25)$$

where $\Delta A(m,n)$ is the area element of a circular cross-section of the sample, $L(m,n)$ is the distance of the area element from the point detector, $t(m,n)$ is the distance traveled by the gamma ray in the sample as shown in Figure 3.7.

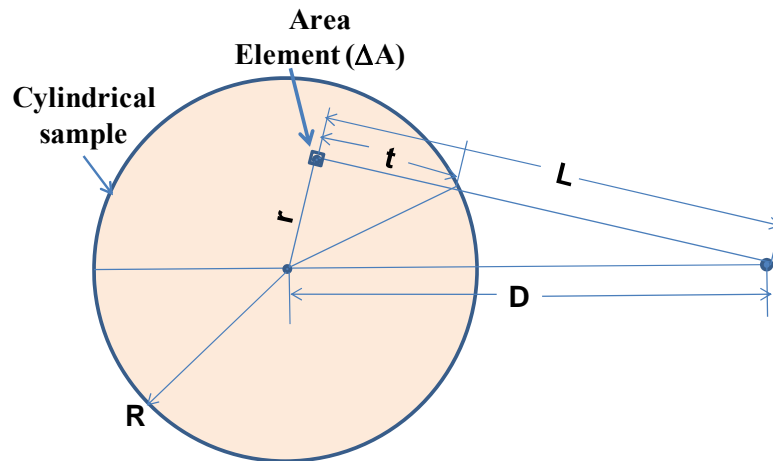


Figure 3.7 Two dimensional model for computing k_{att} for a cylindrical sample.

Figure 3.8(a) shows the two dimensional model k_{att} relative to k_{att} values obtained from far-field expressions for cylindrical geometry. Here also, it was observed that the near-field formula match reasonably well at longer distances at all transmittance with the far-field values and as expected, the deviation starts at shorter sample-to-detector distance at

lower transmittance. The increasing importance of geometric efficiency at less sample-to-detector distance is apparent from the increasing deviation of far-field formula from near-field values as the distance decreases.

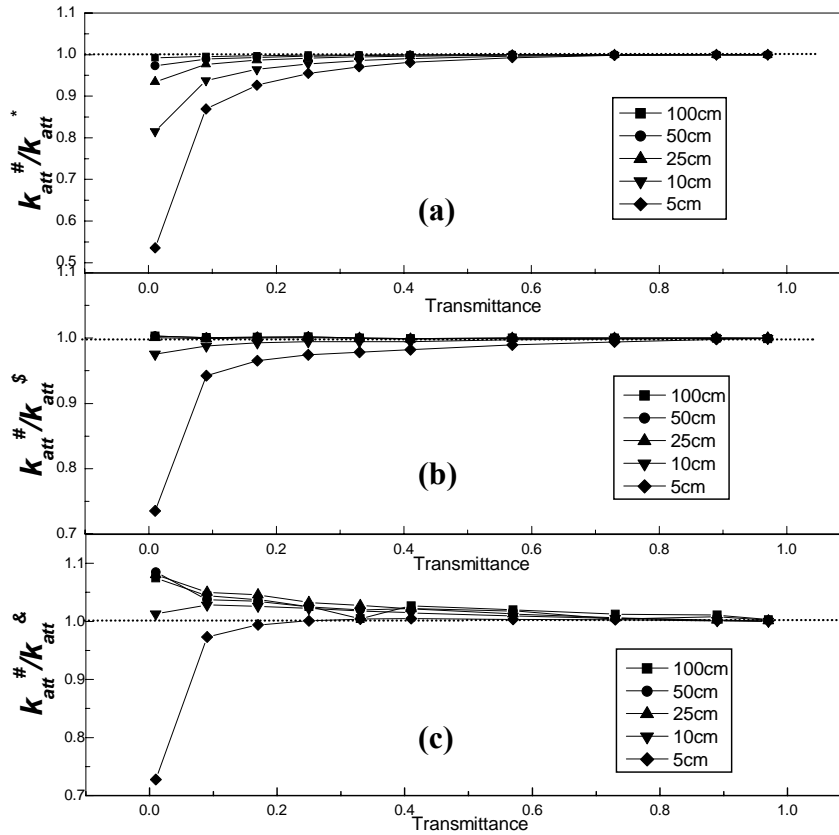


Figure 3.8 Ratio of attenuation correction factors at different distances as a function of transmittance for cylindrical geometry. (a) $k_{att}^{\#}/k_{att}^*$
 (b) $k_{att}^{\#}/k_{att}^{\$}$
 (c) $k_{att}^{\#}/k_{att}^{\&}$

[#] Two-dimensional model [Parker (1991)] calculation

^{\$} Present calculation

^{*} From Parker (1991)

[&] From MCNP calculations

The comparison of the present result with the two dimensional model has been shown in Figure 3.8(b). It is observed that the values match within 2% at all transmittance even at 10 cm sample-to-detector distance. The deviation observed at shorter distance may indicate the failure of the near-field formula at very close sample-to-detector distance and needs further investigation. For quantitative comparison, the k_{att} values at 10, 5 and 3.5 cm sample-to-detector distance, calculated based on two-dimensional model, present calculations and MCNP calculations are given in Table 3.3.

Table 3.3 Results of k_{att} calculations by the present method and comparison with values available in the literature and MCNP values for cylindrical sample.

T	$d = 10$ cm			$d = 5$ cm			$d = 3.5$ cm*		
	$k_{att}^{\$}$	$k_{att}^{\#}$	$k_{att}^{\&}$	$k_{att}^{\$}$	$k_{att}^{\#}$	$k_{att}^{\&}$	$k_{att}^{\$}$	$k_{att}^{\#}$	$k_{att}^{\&}$
0.01	3.09	3.17	3.05	2.03	2.76	2.79	2.27	3.10	3.06
0.09	2.16	2.19	2.10	2.00	2.12	2.06	2.03	2.22	2.13
0.17	1.84	1.86	1.80	1.77	1.83	1.78	1.78	1.89	1.82
0.25	1.65	1.66	1.61	1.61	1.65	1.61	1.62	1.69	1.63
0.33	1.51	1.52	1.49	1.49	1.52	1.48	1.49	1.55	1.50
0.41	1.41	1.42	1.39	1.39	1.42	1.39	1.40	1.44	1.40
0.57	1.25	1.25	1.24	1.25	1.26	1.24	1.25	1.27	1.25
0.73	1.14	1.14	1.13	1.14	1.14	1.13	1.14	1.15	1.14
0.89	1.05	1.05	1.05	1.05	1.05	1.05	1.05	1.05	1.05
0.97	1.01	1.01	1.01	1.01	1.01	1.01	1.01	1.01	1.01

^{\\$} From 2D model

^{\#} From present calculations

^{\&} From MCNP calculations

*These calculations were done with a higher μ so as to reduce the radius of the sample so that sample does not overlap with the detector.

As seen from the table, there is excellent agreement of the results of all the three calculations but for lowest transmittance values where agreement is seen between the present calculation and MCNP. Thus, it is seen that the present method is independent of any approximations regarding sample-to-detector distance for calculating k_{att} for cylindrical geometry.

Similar calculations were performed for box and spherical geometry. Figure 3.9(a) shows the comparison of the present calculation with far-field expressions for box geometry. Again, the deviation from the literature expression is observed at lower transmittance and at shorter distance. The corresponding results with respect to MCNP simulation are shown in Figure 3.9(b). The distance dependence of the deviation, as seen from figure 3.8(a) disappears in Figure 3.9(b). Also, the predictions of MCNP agree within 5-8% with our results at all distance and at all transmittance. Also, there is no near-field formula available for box shaped geometry.

Similar comparisons are shown in Figure 3.10(a) and (b) for spherical geometry. In this case, the results of HMC calculations and far-field formula agree within 1% for all transmittance at all distance except at highest transmittance and 5 cm distance. The MCNP results also show the similar trend. It appears that the far-field formula for spherical geometry is applicable at all sample-to-detector distance in the transmittance range considered in the present work. It is thus seen that the k_{att} values for common sample geometries, at all sample-to-detector distance, and in the transmittance range considered, can be calculated using the common approach developed in the present work. The MCNP calculations also provide a good estimate of the k_{att} . However, the calculations are involved, time consuming and require full description of the detector

geometry and exact sample composition which is not always available. The present calculations are simple, rapid and require only μ , detector diameter and sample dimensions as input. The calculations can be extended to disc-shaped and other common sample geometries.

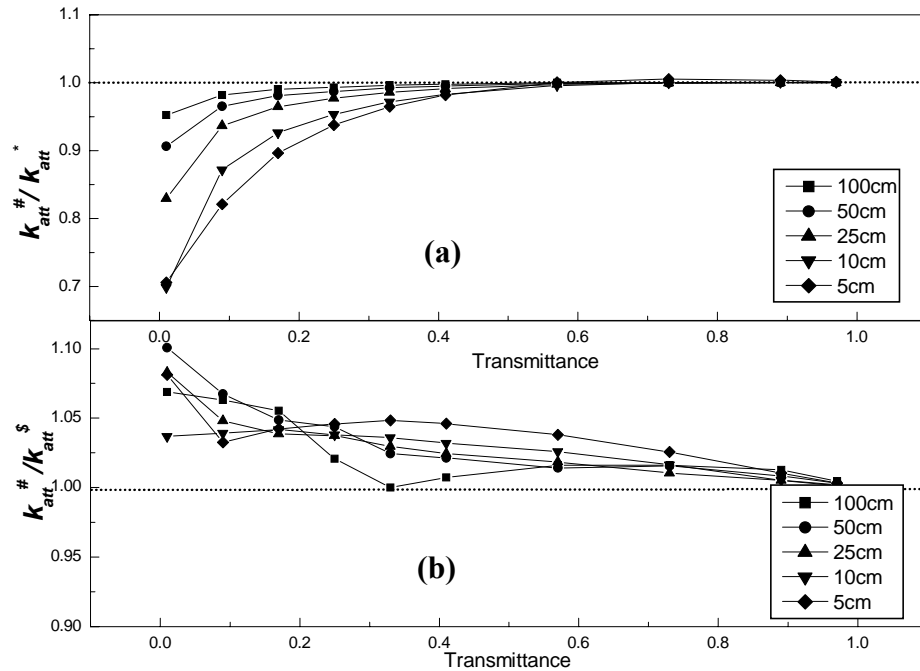


Figure 3.9 Ratio of attenuation correction factors at different distances as a function of transmittance for box-shaped sample. **(a)** $k_{att}^{\#} / k_{att}^{*}$

(b) $k_{att}^{\#} / k_{att}^{\$}$

[#] Present calculation

^{*} From Parker (1991)

^{\$} MCNP calculation

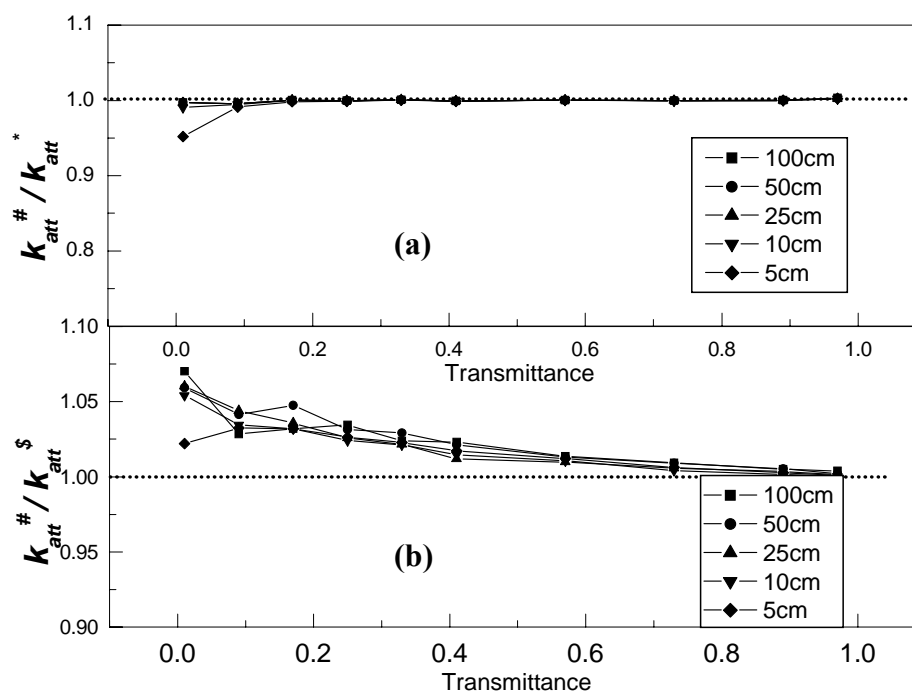


Figure 3.10 Ratio of attenuation correction factors at different distances as a function of transmittance for spherical geometry. **(a)** $k_{att}^{\#} / k_{att}^{*}$
(b) $k_{att}^{\#} / k_{att}^{\$}$

Present calculation

* From Parker (1991)

\$ MCNP calculation

3.5.2 Experimental Validation of the Hybrid Monte Carlo Approach

In order to validate the theoretical computations, attenuation correction factors were also determined experimentally for cylindrical, disc and box geometry.

I. Cylindrical and disc geometry

For cylindrical and disc geometry, uranium solution was chosen as the attenuating matrix.

For this purpose, the four 20 ml standard uranyl nitrate solutions prepared for the

theoretical validation study were used. The cylindrical and disc geometry as explained above in Figure 3.3 was realized by counting the same set of uranyl nitrate samples in a horizontal and a vertical HPGe detector. Both the detectors had a relative efficiency of 20% and a resolution of 2.2 keV at 1.33 MeV. The 143 and 186 keV gamma rays emitted by ^{235}U were monitored. The experimental disintegration rates (dps_{expt}) of a particular uranyl nitrate sample at the energy of interest (143 and 186 keV) was obtained by correcting the measured count rate of the sample with the efficiency at that energy and the intensity of the corresponding gamma ray, as given by:

$$dps_{\text{expt}} = \frac{CR_{\gamma}}{\varepsilon_{\gamma} a_{\gamma}} \quad (3.26)$$

where, CR_{γ} , ε_{γ} , a_{γ} is the count rate from sample, efficiency and abundance of the gamma ray concerned. For efficiency calibration, ^{152}Eu and ^{133}Ba were used in the same geometry. The experimental disintegration rates will not be constant for a particular sample and will show the increasing effect of attenuation as the gamma ray energy decreases. The experimental k_{att} 's at a particular energy was then determined by taking the ratio of the actual disintegration rate of the sample and the experimental disintegration rate at that energy:

$$k_{\text{att}(\text{exp})} = dps_{\text{calc}} / dps_{\text{expt}} \quad (3.27)$$

These measurements were also carried out at different sample-to-detector distances so as to check the applicability of the current approach over a wide range of sample-to-detector distances.

Comparison of HMC results with Experimental, Near-field and MCNP results

To calculate the attenuation correction factors from the HMC method, the sample dimensions and sample-to-detector distance were given as an input in the calculations. In all the calculations, the sample diameter and height were taken to be 2.54 cm and 4 cm respectively. The detector diameter was 5 cm for horizontal detector (cylindrical geometry) and 6 cm for vertical detector (disc geometry). Along with this, the linear attenuation coefficients obtained experimentally at the energies monitored for different samples were given as an input in the program. These calculations were also performed by generating approximately 10^5 particles, using a desktop PC.

To further confirm the result of the present calculations, Monte Carlo simulation for both the geometries was performed using MCNP code. In these calculations, apart from the precise information about the sample-detector geometry, the concentration of uranium in the sample was given as an input. The unattenuated count rate was obtained by replacing the sample solution by air. The k_{att} from MCNP was calculated from the ratio of unattenuated to attenuated count rates. Figure 3.11 shows the theoretical k_{att} values calculated from the given method compared with the experimental and MCNP results for cylindrical geometry at $d = 2.5, 4.5$ and 20 cm as a function of transmittance. It is seen from the figure that at $d = 4.5$ and 20 cm, the experimental and the MCNP k_{att} values matches well with the present method k_{att} and with the near-field formula. But at $d = 2.5$ cm, the near-field values shows a deviation from the experimental and the MCNP k_{att} values but the present approach values matches well. This shows that the near-field formula is not valid at very near sample-to-detector distances while the present calculation is valid at all sample-to-detector distances.

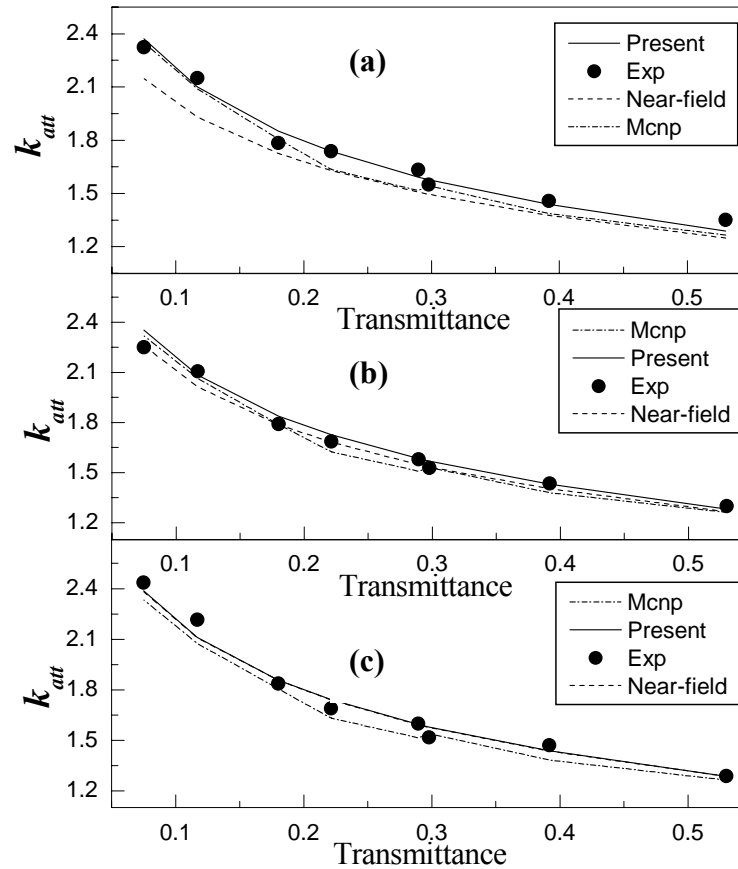


Figure 3.11 The attenuation correction factors computed using numerical approach for cylindrical geometry as a function of transmittance for different sample-to-detector distances (d) (a) $d = 2.5$ cm (b) $d = 4.5$ cm (c) $d = 20$ cm.

Figure 3.12 shows the comparison of theoretical, experimental and MCNP obtained k_{att} values for disc geometry at three sample-to-detector distances, $d = 2, 4, 5$ cm. Here also, the theoretical values match reasonably well with the MCNP and experimental k_{att} values at all the distances. This validates the numerical approach explained above over a wide range of sample-to-detector distances. Figure 3.12 also shows the k_{att} values calculated from a near-field one dimensional model given in Parker (1991):

$$k_{att} = \left[\frac{D}{d(d+D)} \right] / \sum_{I=1}^N \frac{\{\exp[-\mu(I-0.5)\Delta x]\} \Delta x}{[d+(I-0.5)\Delta x]^2} \quad (3.28)$$

Here $\Delta x = D/N$ where D is the sample depth, N is the number of intervals for the numeric integration and d is the distance from the sample surface to the detector surface. The model approximates the sample to be a line sample of depth ‘ D ’ and detector to be a point detector.

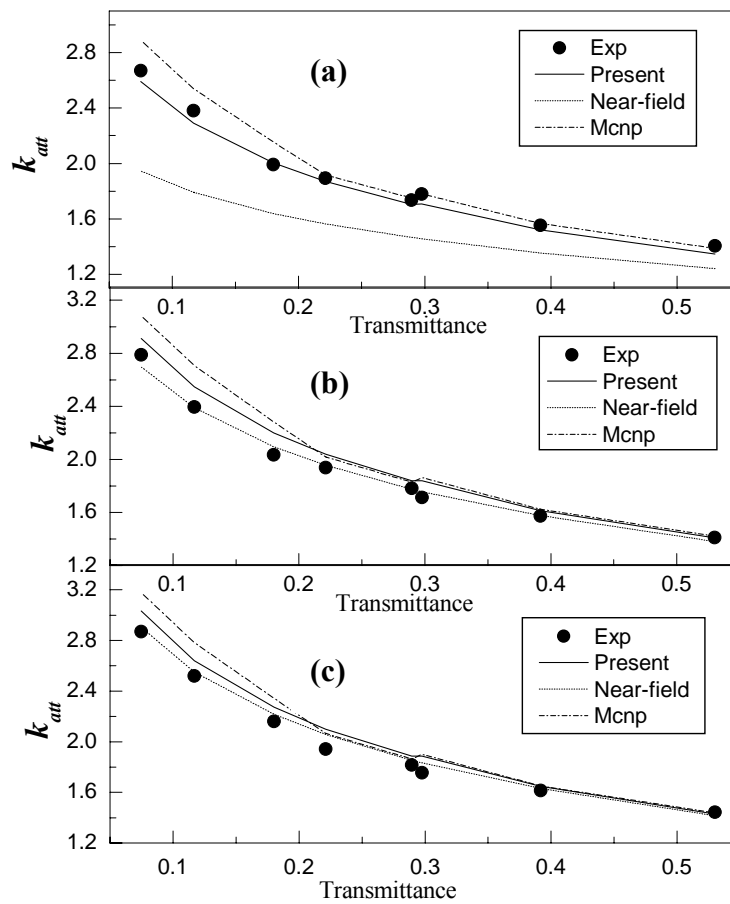


Figure 3.12 The attenuation correction factors computed using numerical approach for disc geometry as a function of transmittance for different sample-to-detector distances (d) (a) $d = 2$ cm (b) $d = 4$ cm (c) $d = 5$ cm.

As seen from the figure, the near-field formula values deviates significantly at very close sample-to-detector distance i.e. when the sample is almost in the touching configuration with the detector. This implies that the near-field formula although said to be valid at close sample-detector geometry, starts working only after certain sample-to-detector distance, whereas the numerical approach is found to be applicable at all sample-to-detector distance.

II. Box geometry

For box shaped samples, lead acetate solutions were used as the attenuating matrix, keeping in mind the high Z of lead and high solubility of lead acetate. These solutions in the concentration range of 10 - 400 mg/ml were prepared by dissolving required amount of lead acetate in water. The linear attenuation coefficients of these samples were measured by using ^{57}Co as the transmittance source by the method described above. To get experimental attenuation correction factors, known amount of ^{57}Co activity was added to the samples. Known amount of activity was also added to a water sample which was chosen as a blank. These samples along with the blank were then counted in a 20% HPGe with a resolution of 2.2 keV at 1332 keV.

Figure 3.13 shows the experimental count rate per gram for ^{57}Co activity as a function of lead acetate concentration for box samples. The straight line in the figure shows the expected count rate per gram as a function of lead acetate concentration. Here also, due to gamma ray attenuation, there is increasing deviation from linearity with increasing lead acetate concentration increases.

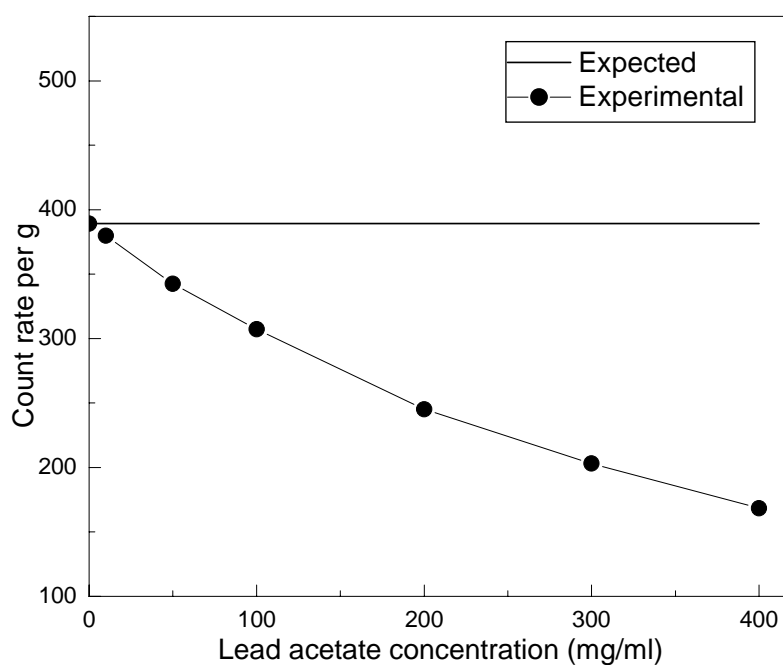


Figure 3.13 Count rate per gram of ^{57}Co activity at 122 keV as a function of lead acetate concentration. The straight line shows the expected count rate per gram as a function of lead acetate concentration.

Comparison of HMC results with Experimental, Near-field and MCNP results

For box samples, experimental k_{att} were determined by taking the ratio of count rate per gram of blank to the count rate per gram of sample. These k_{att} were compared with the far-field k_{att} as given by equation 3.23 and with the k_{att} calculated from present approach. Figure 3.14 shows the experimental, far-field and present method k_{att} for box-shaped sample at sample-to-detector distances, $d = 2.6, 5.0$ and 20.1 cm. As expected, at close distance i.e. at $d = 2.6$ and 5.0 cm, the experimental k_{att} deviates significantly from far-field values but matches quite well with the present approach k_{att} . When the sample-to-detector distance is 20.1 cm, all the three attenuation correction factors match well. This again shows that the present approach is valid at all sample-to-detector distances.

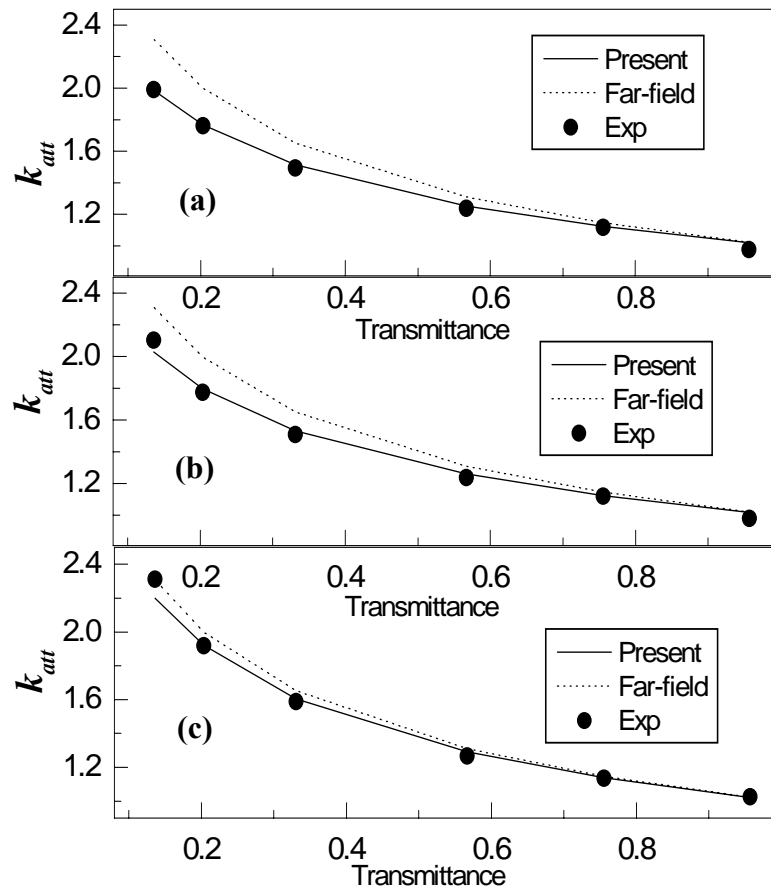


Figure 3.14 The attenuation correction factors computed using numerical approach for box geometry as a function of transmittance for different sample-to-detector distances, **(a)** $d = 2.6$ cm **(b)** $d = 5.0$ cm **(c)** $d = 20.1$ cm.

3.6 Conclusion

A hybrid Monte Carlo method has been developed for calculation of attenuation correction factors for samples of varied geometries. The method has been theoretically and experimentally validated. It was observed that the near-field formulas available in literature are applicable only after certain sample-to-detector distance. The results of the

present calculation show the possibility of using a simplified common approach to calculate the k_{att} for the simple geometries considered, over wide range of transmittance. The advantage of the HMC method is that it is free of any assumptions regarding sample-detector geometry. Also, the present approach is common to all sample geometries and sizes. The calculations will be particularly useful for attenuation corrections at shorter sample-to-detector distance where analytical formulae are not available. Also, these calculations will be useful when collimator geometry is involved for which no analytical expressions are available. The present calculation can also be extended to other geometries.

Apparent mass method for nonstandard source geometry

- 4.1 Introduction
- 4.2 Apparent mass method: *Basic principle*
- 4.3 Standardization of Apparent Mass Method
 - 4.3.1 *Uranium assay*
 - 4.3.2 *Plutonium assay*
- 4.4 Applications
 - 4.4.1 *Empty stainless steel boxes*
 - 4.4.2 *Sludge samples*
 - 4.4.3 *Enriched uranium sample*
- 4.5 Conclusion

4.1 Introduction

Nonstandard samples do not have a standard geometry (shape or size) and hence gamma ray standards are not available for them. In nondestructive assay of nuclear materials, the samples can be of diverse shapes and sizes, and the possibility of encountering samples with nonstandard geometry commonly exists. Waste packets or drums, PuO₂ powder distributed inhomogeneously in a sealed packet or in a box are examples of the samples having nonstandard geometry. Gamma ray spectrometry based nondestructive assay procedures, generally applied for samples with standard geometry, cannot be used here due to difficulty in efficiency calibration of the detector. Apart from this, there can be further limitation in the assay of these samples due to self-absorption taking place in the samples. Finding μ for such samples is difficult as compositions and spatial distributions are uncertain. Also, usual attenuation correction procedures cannot be used as these methods are applicable to standard geometries like cylinder, disc, box, sphere only. There is no well defined method available for the assay of such samples and it is a very challenging task.

In this chapter, the basic principle of an empirical approach [Venkataraman and Croft (2003)] called “apparent mass method” has been explained and the work carried out to standardize this method for the assay of uranium and plutonium in attenuating samples has been discussed. Also, work carried out to apply this method to a variety of samples eg. empty stainless steel containers used to store plutonium, sludge samples and enriched uranium samples have been presented.

4.2 Apparent Mass Method: *Basic Principle*

The apparent mass method takes advantage of the multi-gamma rays emitted by the nuclide monitored and relies on the empirical relation between apparent mass of the nuclide and gamma ray energy to get the nuclide amount. The method involves the measurement of several gamma ray peak areas corresponding to different energies of the radionuclide monitored, and the determination of “apparent mass” at each of the measured gamma ray energies. The apparent mass, $m(E)$ is defined as the mass of the element in the sample that had not been corrected for the gamma ray attenuation through the sample and is given by:

$$m(E) = \frac{C_{net}}{\varepsilon_{\gamma} I_{\gamma} w_A S_A} \quad (4.1)$$

where C_{net} is the net count rate of the gamma ray peak, I_{γ} is the intensity of the gamma ray, w_A is the weight fraction of the radioisotope in the sample and ε_{γ} is the peak efficiency of the detector for the required sample geometry and S_A is the specific activity of the isotope concerned. Ideally, all the gamma ray energies should give the same mass, $m(E)$ of the element. This will be true for samples with no self-attenuation. But for attenuating samples, the apparent masses will not be constant and will be an inverse function of absorption or scattering of gamma rays within the sample. Since the attenuation is a function of gamma ray energy and decreases with increase in gamma ray energy, therefore the apparent masses will also increase with gamma ray energy. The apparent mass will correspond to the true mass only for gamma ray energy tending to

infinity (or $1/E \rightarrow 0$) i.e. when there is no self-attenuation taking place in the sample. Therefore, the apparent mass is fitted to the functional form:

$$m(E) = m_o(1 - B/E) \quad (4.2)$$

where m_o is the quantity of interest and is the true mass of the element obtained as intercept, in the limit $1/E \rightarrow 0$ for which attenuation correction becomes unity and B is treated as a free parameter in the fitting procedure. The m_o is obtained by the extrapolation of fitted curve between $m(E)$ and $1/E$ to infinite photon energy. Therefore, this method correlates the variation of apparent mass with gamma ray energy and provides actual mass of the sample (zero photon attenuation condition).

4.3 Standardization of Apparent Mass Method

4.3.1 Uranium Assay

Work was carried out to standardize the apparent mass method for the assay of samples containing uranium.

Gamma spectrometric measurements

To standardize the method for uranium assay, standard uranyl nitrate solutions were chosen as the attenuating matrix. These solutions in the concentration range of 12 mg/ml to 400 mg/ml were prepared by dissolving required amount of U_3O_8 powder in conc. HNO_3 , followed by dilution with 2M HNO_3 . These solutions were taken in standard 20 ml glass vials and care was taken so that solution volume in all the vials is same (20 ml) so that geometry of the samples remains same during counting. Samples were counted in 20% co-axial HPGe detector coupled to a 4k channel analyzer. The resolution of the

detector was 2.0 keV at 1332 keV. Counting time was varied depending upon the count rate to keep the error in the peak area below 1% for all the samples with a maximum counting time of 50000s for samples upto 12 mg/ml of uranium. The gamma ray spectra were analyzed using the PHAST software developed at Electronics Division, BARC [Mukhopadhyaya, 2001]. The energy of the gamma rays that was used in the analysis of uranium spectra and their intensities are given in Table 4.1 [Reus and Westmeier, 1983].

Table 4.1 ^{235}U gamma ray peaks used in the analysis.

Energy (keV)	Gamma ray intensity (%)
143.8	11
163.4	5.16
185.7	57.4
205.3	5

Results and Discussion

For concentration below about 30 mg/ml, the cps obtained from the different gamma ray energies were found to increase linearly with uranium concentration, indicating practically no self-absorption in the samples. Taking one of these samples as standard, gamma ray efficiencies at the four energies considered in this work were obtained. The efficiency values are shown in Figure 4.1. The solid line is the eye guide only. Using these efficiencies, the apparent disintegrations per second (*dps*) in all the samples were calculated and the values are plotted as a function of uranium concentration in Figure 4.2

for different gamma ray energies. In this figure, the solid squares show the plot of expected dps of ^{235}U in the samples over the entire range of concentration used in the present work. The expected dps was calculated using the known half-life and the uranium amount. The effect of self-absorption is visible from the deviation of the apparent dps from linearity with increasing concentration of uranium, the deviation increasing with decrease in the gamma ray energies. The apparent mass of the samples at the given energy E were obtained using the equation 4.1. The C_{net} is the net count rate of the concerned gamma ray peak of ^{235}U , w_A in the equation corresponds to the weight fraction of the ^{235}U in uranium (taken as 0.0072 corresponding to natural uranium samples) and ε_γ is the peak efficiency of the detector at the standard sample geometry, obtained using non-attenuating standard uranium sample as described earlier.

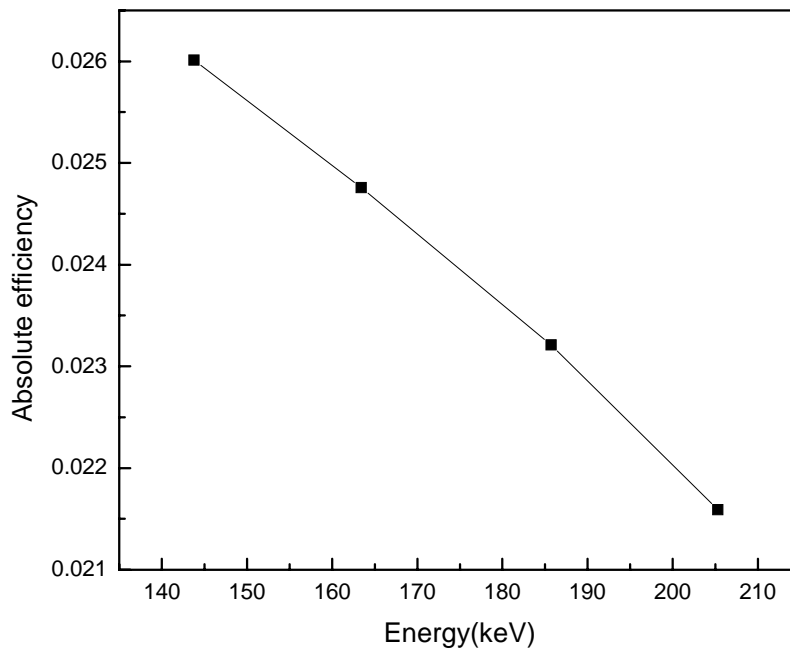


Figure 4.1 Absolute efficiency as a function of gamma ray energy (keV) of ^{235}U .

The apparent masses in Venkataraman and Croft (2003) were fitted to the functional form of equation 4.2. This equation is based on general observation that, in the energy range of interest, the attenuation varies inversely with the photon energy. The apparent masses at different energies obtained in the present work for samples of different concentration were fitted to equation 4.2 to obtain true mass of uranium present in different samples. The values were found to be grossly over-estimated. On observing the general trend of the data for different samples, the equation 4.2 was modified in this work by changing the exponent of 'E'. It was observed that best fit for all the samples is obtained with:

$$m(E) = m_0(1 - B / E^{1.35}) \quad (4.3)$$

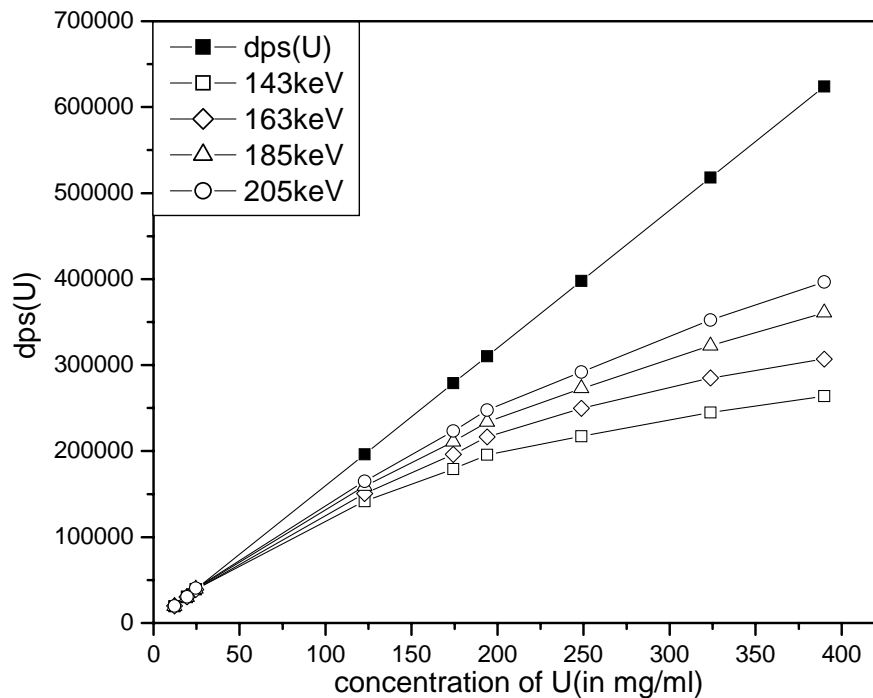


Figure 4.2 The plot of disintegration rate vs. concentration of uranium (mg/ml) at different energies.

The plots of $m(E)$ vs. $1/E^{1.35}$ for the different samples are shown in Figure 4.3. The error bars in the figure are of the size of the symbols. Errors given are due to counting statistics. It was seen that a good straight line fit is obtained for all the samples. Also, the slope of the curves systematically decreased with decreasing concentration of the sample, ultimately becoming parallel to x-axis for non-attenuating samples. The slopes parallel to x-axis indicate no attenuation taking place in the sample for the gamma ray energies of interest. The values of m_o obtained for different samples and the expected values are given in Table 4.2.

Table 4.2 The expected and obtained uranium concentration in aqueous samples.

Uranium concentration (mg/ml)	Uranium concentration obtained (mg/ml)	% deviation
390.0	381.0 ± 12.3	2.3
323.8	326.8 ± 5.6	-0.9
248.8	257.3 ± 2.5	-3.4
193.9	206.3 ± 1.5	-6.4
174.3	183.1 ± 2.5	-5.1
122.7	126.3 ± 1.0	-3.0
24.5	26.4 ± 1.2	-7.5
19.4	19.6 ± 0.4	-1.2
12.3	12.3 ± 0.5	-0.2

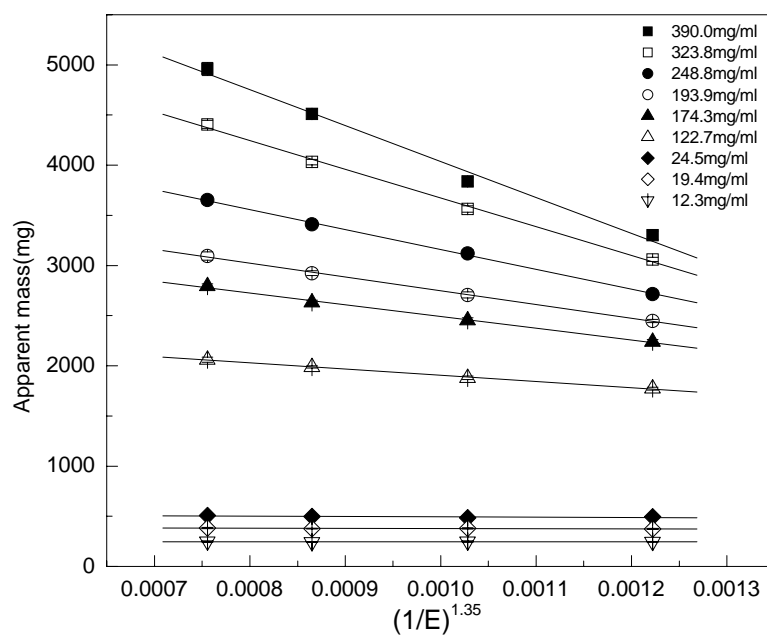


Figure 4.3 Apparent mass of uranium as a function of $1/E^{1.35}$ for different samples where E is the gamma ray energy in keV.

It is seen that the values of the true mass (m_o) of the radionuclide are mostly within 2-5% of the expected values. The results show the validity of the approach in Venkataraman and Croft (2003) for aqueous uranium samples. However, the empirical equation needs adjustment of the exponent of E from 1.00 to 1.35. Thus it is feasible to determine concentration of unknown aqueous uranium samples rapidly by the present method, without going through the transmission corrected gamma ray counting method, provided high accuracy <1% is not needed. Also method can be applied to cases when sample geometry and composition is not well defined.

4.3.2 Plutonium Assay

Gamma spectrometric measurements

To standardize the apparent mass method for the assay of plutonium, packets of standard plutonium oxide powder were used. A series of known amount of pure plutonium oxide powder samples were wrapped in paper and doubly sealed in polyethylene packets. The standards were prepared on weight basis. No independent analytical method was used to verify the amount of plutonium in the sample. The samples were rectangular in shape (3cm x 4cm). The powders were distributed within the packet and there was no knowledge about the distributions. Hence, the density and thickness of the samples were not known. These plutonium standards were counted in a 20% co-axial HPGe detector coupled to 4k channel analyzer. The samples were rotated manually by 180° in steps of 45° and counting was done at each geometry to average out any asymmetry in the actual distribution of the oxide powders in the samples. Cd filters (1 mm) were used to reduce the count rate of 59.54 keV ^{241}Am gamma rays. Also, due to the unavailability of the standard of same geometry, the sample-to-detector distance was kept about 30 cm so that standard point source of ^{152}Eu and ^{133}Ba could be used for the determination of efficiency of the detector. Since the sample-to-detector distance was large compared to the dimension of the sample, it was assumed that the point source efficiency will represent the true efficiency. The gamma ray spectra were analyzed using the PHAST software [Mukhopadhaya, 2001].

Results and Discussion

The apparent mass of the plutonium samples ($m(E)$) at the given energy E were obtained using equation 4.1. Table 4.3 gives the gamma ray energies of the nuclides and their corresponding gamma ray intensities for which apparent masses were obtained. The gamma ray intensities were taken from the ref. [Reilly et al. (1991)]. The weight fraction (w_A) of the plutonium isotope in the sample emitting the gamma ray was obtained by determining the isotopic composition of the plutonium sample and are given in the last column of Table 4.3. This was obtained by using the relative efficiency method [Tripathi et al. (2002)].

Table 4.3 Gamma ray energies and intensities of the nuclides used in the analysis.

Nuclide	Energy (keV)	Gamma ray intensity (%)	Isotopic fraction
²³⁹Pu	129.29	6.31E-03	0.9416
	203.55	5.69E-04	
	345.01	5.56E-04	
	375.05	1.55E-03	
	413.71	1.47E-03	
²⁴¹Pu	208.00	5.34E-04	0.665 x 10 ⁻³
²⁴¹Am	125.30	4.08E-03	0.317 x 10 ⁻²

Figure 4.4 shows the plot of apparent masses ($m(E)$) vs. $1/E$ for the samples containing plutonium in the range of 346.65 to 3319.36 mg of plutonium. The apparent masses were

fitted to the functional form of equation 4.2. The error bars in the Figure 4.4 are of the size of the symbols and are due to counting statistics. It is seen that a good straight line fit is obtained for all the samples. Also, the slope of the curves systematically decreases with decreasing amount of the sample, ultimately becoming parallel to x-axis for less-attenuating samples. The m_o for a particular sample was obtained from the intercept of the corresponding fitted curve. The values of m_o obtained for different samples and the expected values are given in Table 4.4. The error on the measured plutonium amount reflects the error on the intercept. It is seen that the m_o values are mostly within 10% of the expected values. However, the deviations cannot be accounted for by the statistical uncertainty on the data, indicating some bias. Slight adjustment of the exponent of E in equation 4.2 could remove this uncertainty which was not attempted. This method is very useful for the determination of small quantities of plutonium samples where appropriate standard cannot be used due to inhomogeneous distribution of plutonium in the sample matrix.

Table 4.4 The expected and the obtained plutonium amount in the samples.

Expected amount (mg)	Amount obtained (mg)	% Deviation
640.06	611.48 ± 3.25	4.5
543.77	496.27 ± 5.19	8.7
346.65	335.44 ± 3.15	3.2
1453.03	1307.63 ± 9.32	10.0
2714.64	2409.17 ± 10.39	11.3
3319.36	2806.57 ± 18.48	15.4

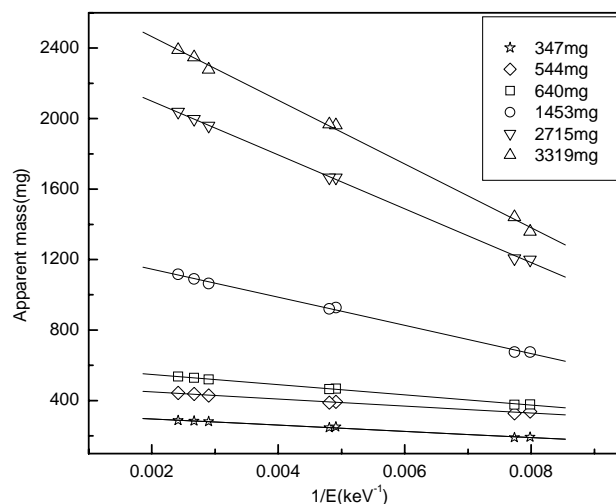


Figure 4.4 The apparent mass of plutonium as a function of $1/E$ for different samples, where E is the gamma ray energy in keV.

4.4 Applications

The apparent mass method developed for the assay of uranium and plutonium has been applied to a variety of uranium and plutonium samples with unknown concentrations.

The details are given below:

4.4.1 Empty Stainless Steel Boxes

Plutonium in the form of powders is stored in stainless steel containers. For accounting the total plutonium, the amount of plutonium left in the stainless steel boxes after complete transfer must be checked. Since there is no knowledge of distribution of plutonium in the empty boxes, the apparent mass method was used to assay the left over plutonium amount. These samples were counted in a 20% co-axial HPGe detector coupled to 4k channel analyzer. Cd filters of 1 mm thickness were used to reduce the count rate of 59.54 keV ^{241}Am gamma rays. The samples were counted at a distance of 30

cm from the detector surface. Such a large sample-to-detector was chosen so that standard point source of ^{152}Eu and ^{133}Ba could be used for the determination of plutonium amount. The counting of these point sources was carried out in a fresh stainless steel container so as to correct for the attenuation of the plutonium gamma rays in the steel container. The gamma ray spectra were analyzed using the PHAST software [Mukhopadhaya, 2001]. Figure 4.5 shows the efficiency calibration curve obtained using ^{152}Eu and ^{133}Ba standard sources.

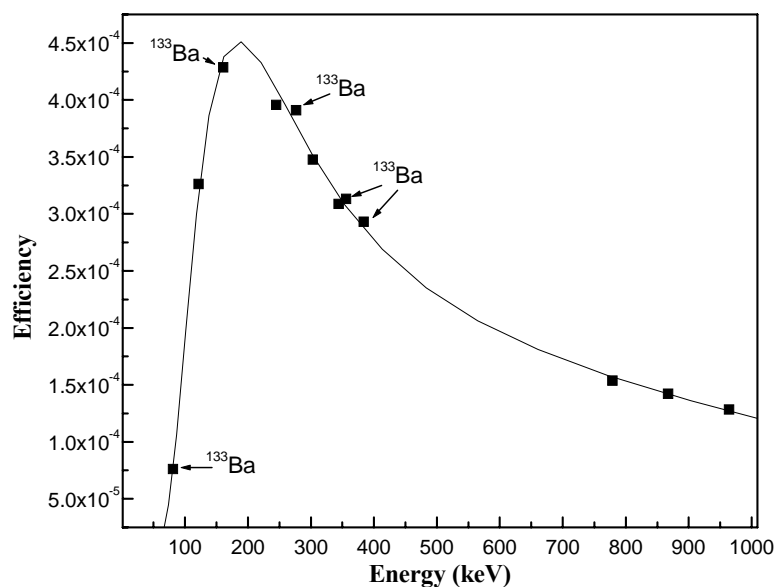


Figure 4.5 The ^{152}Eu - ^{133}Ba efficiency curve as a function of gamma ray energy.

The apparent mass was obtained for different gamma rays of plutonium (given in Table 4.3) for a series of samples. The isotopic composition used in the apparent mass determination has been given in Table 4.5. The plot of apparent mass as a function of $1/E$ is shown in Figure 4.6 and is fitted into a straight line to get the actual plutonium amount in different samples from the intercept. The lines with zero slopes in the figure indicate

no self-attenuation within the sample. The actual plutonium amounts obtained from apparent mass method have been given in Table 4.6.

Table 4.5 Isotopic composition of one of the representative empty stainless box.

Nuclide	Isotopic composition (%)
^{238}Pu	0.135
^{239}Pu	77.94
^{240}Pu	17.70
^{241}Pu	3.820
^{242}Pu	0.405
^{241}Am	0.272

Table 4.6 The plutonium amount obtained in different stainless steel samples.

Sample No.	Plutonium amount (mg)	
	Apparent mass method	Neutron coincidence counting
1	101±10	111±11
2	36±4	39±4
3	27±3	29±3
4	27±3	29±3

To check the reliability of the values, the samples were also assayed by neutron coincidence counting. For neutron coincidence counting, samples were counted using a shift-register based Neutron Well Coincidence Counter (NWCC) having 24 ^3He counters of 2.54 cm diameter and 50 cm length arranged in an annular geometry. In NWCC, the counters are embedded in HDPE (moderator) of thickness 10.5 cm. The absolute efficiency of the counter is 15%. The last column of Table 4.6 gives the results of neutron coincidence counting. It can be seen that both the results match within 10% indicating the reliability of the apparent mass results.

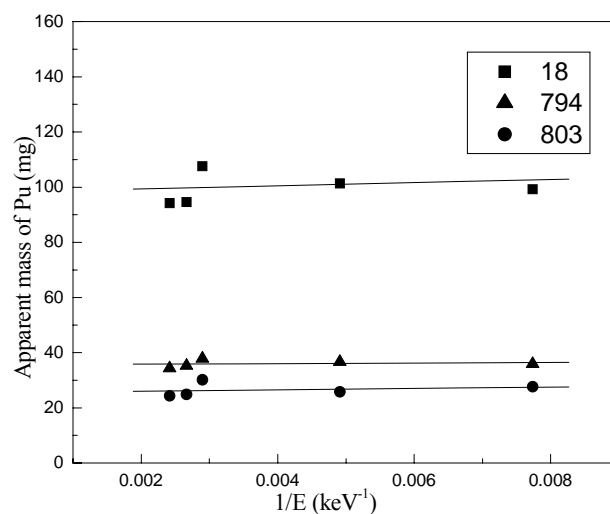


Figure 4.6 Apparent mass of plutonium as a function of $1/E$ for different samples where E is the gamma ray energy.

4.4.2 Sludge samples

The sludge of uranium is generated during the processing of uranium from its mining and milling stage to pelletization stage. The assay of uranium in such samples is required for nuclear material accounting. Two such sludge samples from the settling tank of AFD were analyzed for their uranium content. These samples were non-homogeneous due to

the settling of sludge in tank. Due to this non-homogeneity, no uranium standards can serve the purpose. Therefore, the apparent mass method was used to get the total uranium amount. For this, these samples were counted in HPGe detector at a sample-to-detector distance of 20 cm and apparent masses were obtained using equation 4.1. The efficiencies required for obtaining apparent mass calculation was obtained by using 5 ml of ^{152}Eu - ^{133}Ba efficiencies. The apparent masses were then fitted into a straight line using equation 4.3 taking the exponent of $1/E$ as 1.35 as found from the standardization of apparent mass method for uranium assay using standard uranyl nitrate solutions. Figure 4.7 shows the apparent mass curve for the two sludge samples. A finite slope in both the cases indicates nonzero attenuation within the samples. The actual mass of uranium obtained from the intercept of the curves in Figure 4.7 is given in Table 4.7.

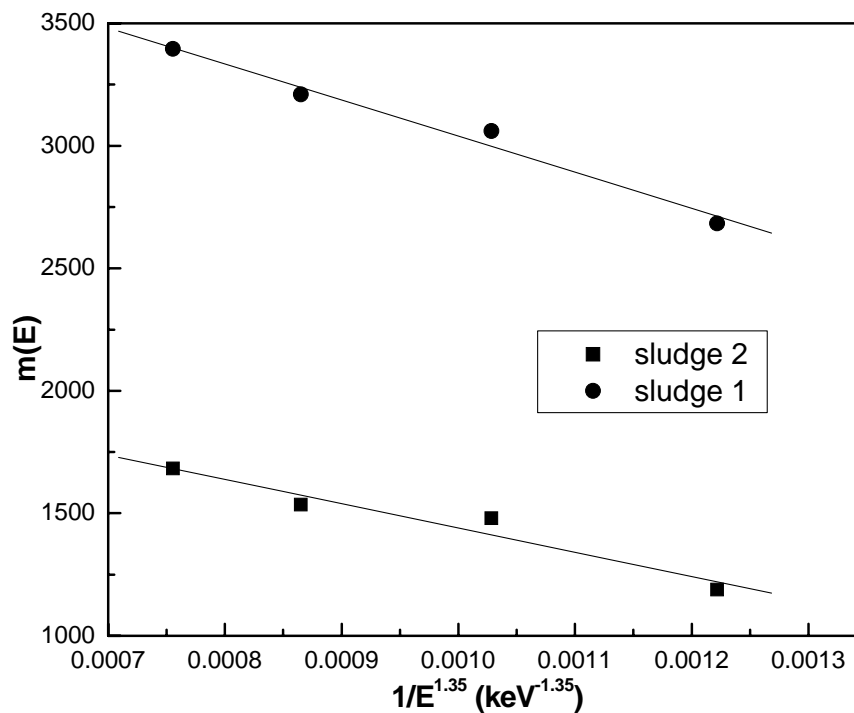


Figure 4.7 The apparent mass curve for the two sludge samples.

Table 4.7 The results of uranium assay in the sludge sample.

Sample	Uranium amount (g) present in sample
Tank 1	4.51 ± 0.45
Tank 2	2.43 ± 0.24

4.4.3 Enriched Uranium Sample

A 100 ml volumetric flask containing 47 ml of enriched uranium solution with 96% of ^{235}U has been assayed by apparent mass method. This method was used as standards of such geometry are not generally available. The sample was counted at a distance of about 20 cm to ensure the validity of the 5 ml liquid source efficiencies. ^{152}Eu and ^{133}Ba sources were used to get efficiencies at the energies of interest. To check the reliability of the results given by the apparent mass method, 5 ml aliquot of the sample was taken in a standard glass vial and counted at a distance of 7 cm from the detector along with the 5 ml ^{152}Eu and ^{133}Ba sources for efficiency. The uranium amounts were obtained by correcting the count rate obtained with the corresponding peak efficiency, gamma ray abundance, weight fraction of ^{235}U and its specific activity. The results from both the methods are presented in Table 4.8.

Table 4.8 The results of enriched uranium assay by apparent mass method and by simple gamma counting.

Method employed	Uranium concentration (mg/ml)
Apparent Mass Method	20.09
Simple Counting	20.23
% RSD	0.69

It can be seen from the table that the results are in excellent agreement with each other. This validates the apparent mass approach. In the present case the apparent mass method was better in a sense no aliquoting was required as needed by the simple counting methodology.

4.5 Conclusion

The apparent mass method is very useful method for the assay of uranium and plutonium in samples with nonstandard geometry. It can be used to estimate these elements in samples where there is no knowledge about the distribution of source and also when the distribution is nonhomogeneous.

Full Energy Peak Efficiency Calibration of HPGe detector by MCNP

- 5.1 Introduction
- 5.2 Efficiency calibration: Different methods
- 5.3 Monte Carlo method
 - 5.3.1 *Detector parameters determination*
 - 5.3.2 *Effect of detector parameters on the FEP efficiency*
 - 5.3.3 *Optimization of detector geometry*
- 5.4 Objective of the work
 - 5.4.1 *Gamma spectrometric measurements*
 - 5.4.2 *Monte Carlo Simulation*
 - 5.4.3 *Comparison of MCNP and experimental efficiencies*
- 5.5 Optimization of different detector parameters
 - 5.5.1 *Detector crystal geometry*
 - 5.5.2 *Detector end cap thickness and end cap to crystal distance*
- 5.6 Efficiency transfer to volumetric sources
- 5.7 Conclusion

5.1 Introduction

As emphasized in Chapter 2, calculation or measurement of full energy peak (FEP) efficiency for particular source-detector geometry is essential for quantitative analysis of any radionuclide by gamma ray spectrometry. Efficiencies at a particular gamma ray energy E is experimentally obtained by using a gamma ray source (emitting photon of energy E) of known disintegration rate. The calibration of FEP efficiency as a function of gamma ray energy is known as FEP efficiency calibration of a gamma ray detector. Since no two detectors can have exactly the same sensitive volume, their efficiencies can never exactly match so that each gamma ray detector has to be individually calibrated for its efficiency to get reliable results.

5.2 Efficiency calibration: *Different methods*

For routine gamma spectrometric analysis, efficiency calibration of a gamma ray detector is carried out using a set of standards emitting gamma rays over the energy range of 50-1500 keV. Full energy peak efficiency calibration is preferably done using the monoenergetic gamma ray sources e.g. ^{241}Am , ^{109}Cd , ^{57}Co , ^{139}Ce , ^{203}Hg , ^{51}Cr , ^{113}Sn , ^{85}Sr , ^{137}Cs and ^{65}Zn . The gamma ray energies and abundances along with the half-lives of these radionuclides are given in Table 5.1. However, the availability of monoenergetic primary standards is a constraint. Moreover, some of these sources are not very long lived e.g. ^{203}Hg ($t_{1/2}$ -46.6 d), ^{51}Cr ($t_{1/2}$ -27.7 d), so they need to be replaced periodically.

Table 5.1 Monoenergetic sources used as calibration sources.

Nuclide	Energy (keV)	Gamma ray Abundances (%)	Half-life
¹⁰⁹ Cd	88.04	3.6	462.2 d
⁵⁷ Co	122.06	85.6	271.8 d
¹³⁹ Ce	165.86	79.9	137.6 d
²⁰³ Hg	279.2	81.5	46.6 d
⁵¹ Cr	320.1	98.6	27.7 d
¹¹³ Sn	391.7	64.0	115.1 d
⁸⁵ Sr	514.0	95.7	64.9 d
¹³⁷ Cs	661.6	85.1	30.2 y
⁶⁵ Zn	1115	50.6	244.3 d

Multi-gamma ray sources like ¹⁵²Eu (13.5 y), ¹³³Ba (10.5 y), ¹¹⁰Ag^m (249.9 d), ²²⁶Ra (1.6 x 10³ y) and ⁵⁶Co (78.8 d) are often preferred for efficiency calibration as they cover a wide energy range and are longer lived. The gamma ray energies of these radionuclides are given in Table 5.2. However, these sources emit gamma rays in cascade and for close sample-to-detector distances, there may be substantial coincidence summing leading to inaccuracy in efficiency calibration. Therefore, standard multi-gamma sources cannot be used for efficiency calibration of a detector at close sample-to-detector distance. However, gamma spectrometric analysis of low level samples needs to count the samples

as close as possible to the detector. These difficulties can be circumvented using Monte Carlo simulation for full energy peak efficiency.

Table 5.2 Multi-energetic sources used as calibration sources.

Nuclide	Energy (keV)	Gamma ray abundance (%)	Nuclide	Energy (keV)	Gamma ray abundance (%)
¹⁵² Eu	121.78	28.4	¹³³ Ba	81	34.1
	244.69	7.5		160.6	64.5
	344.28	26.6		276.4	7.16
	444.0	2.8		302.9	18.33
	778.9	13.0		356	62.05
	964.05	14.6		383.9	8.84
	1112.0	13.5	⁵⁶ Co	846.8	99.9
	1408.03	20.8		1037.8	14.0
¹¹⁰ Ag^m	657.7	94.0		1238.3	67.6
	677.6	10.3		1771.4	15.7
	706.7	16.3		2598.6	17.3
	763.9	22.1	²²⁶ Ra	295.2	18.5
	884.7	75.9		351.9	35.8
	937.5	34.1		609.3	44.8
	1384.3	24.1		1120.3	14.8
	1505.0	12.9		1764.5	15.4

5.3 Monte Carlo Method

It is a powerful tool to simulate the detector response and is applicable to a variety of sample matrices and geometries [Sima and Arnold (2009), Vidmar et al. (2008), Tzika et al. (2004), Ródenas et al. (2003), Ewa et al. (2001)]. The basic principle of this method has been discussed in Chapter 1. Monte Carlo methods were first used by Wainio and Knoll (1966) and De Castro Faria and Levesque (1967) for full energy peak efficiencies calculations. Bronson and Wang (1996) have given an extensive description on the use of the Monte Carlo method for efficiency determination at various source–detector geometries (on and off detector axis), complex source shapes and Marinelli beaker models. General Monte Carlo codes like MCNP [Wang et al. (1994), Kamboj and Kahn (1996), Fehrenbacher et al. (1996), Glouvas et al. (1998), Rodenas et al. (2000)], GEANT [Glouvas et al. (1998), Sanchez et al. (1991), Decombaz et al. (1992), Garcia-Talavera (2000), Korun et al. (1997)], EGS4 [Fehrenbacher et al. (1996)], CYLTRAN [Ludington and Helmer (2000)] are also being tested extensively. These codes are increasingly used to simulate efficiency for cases where experimental determination is impossible or difficult such as samples of nonstandard geometry and for large sized samples e.g. environmental samples [Nakamura and Suzuki (1983)] and waste drums where standards are not easily available. Also, these simulation methods are decay scheme independent and are consequently free of any coincidence summing. Therefore, these methods can be used to obtain FEP efficiency at closest sample-to-detector distance where multi-gamma ray sources cannot be used. Additionally, these simulation codes can be used to get total efficiency required for coincidence summing correction. However, as reported in most of the literature, there is often a mismatch between the simulated and experimental

efficiencies. This is due to the inaccuracy of the detector geometry specifications given by the manufacturer. The dimensions provided by the manufacturer correspond to the time of assembly of the detection system at room temperature. But there can be changes in the mechanical support of the crystal due to contractions at low temperature leading to changes in the detector configuration [Johnston et al. (2006)]. Also, there can be uncertainty in the parameters e.g. dead layer thickness, detector end cap to Ge crystal distance etc. The problem can be overcome by either determining the dimensions of detector or by adjusting the detector parameters such that the simulated efficiencies match with the experimental efficiencies. The studies in literature available for both the methods have been discussed in the subsequent sections.

5.3.1 Detector Parameters Determination

Crystal parameters and position

There are reports in literature in which the physical characteristics of the detector have been measured experimentally to minimize these uncertainties [Helmer et al. (2003), Hardy et al. (2002), Dryak and Kovar (2006), Budja'sˇ et al. (2009)]. The shape, dimensions and location of the crystal have been found out using gamma or X-ray radiography [Dryak and Kovar (2006), Budja'sˇ et al. (2009), Johnston (1985), Boson (2008)]. Typical X-ray and gamma ray radiographs have been shown in Figure 5.1. A number of photographs from different directions are needed to get the detector position and its displacement from the crystal axis. The length of the sensitive region of the detector has also been determined by scanning the detector along its axis and accuracy less than 1% has been achieved between experimental and calculated efficiency [Helmer

et al. (2003), Hardy et al. (2002), Debertain and Grosswendt (1982)]. The energy of the gamma ray photon used for scanning is chosen in such a way that it should be high enough to penetrate the window and detector housing and it should be low enough to be sensitive to the thickness of any attenuating layers and is effectively collimated by the collimator. Debertain and Grosswendt (1982) used a collimated beam of gamma ray from ^{241}Am source with a 20 mm long lead collimator with a 1 mm hole in diameter. The source-collimator assembly was moved in 1 mm steps and the counts at 59.5 keV peak were monitored. Several scans, along different diameters or along lines parallel to one another, were carried and the position, diameter, and thickness of the sensitive volume could thus be determined with a resolution of 1 mm. The diameter of the insensitive core of the true co-axial detector has also been measured in this way.

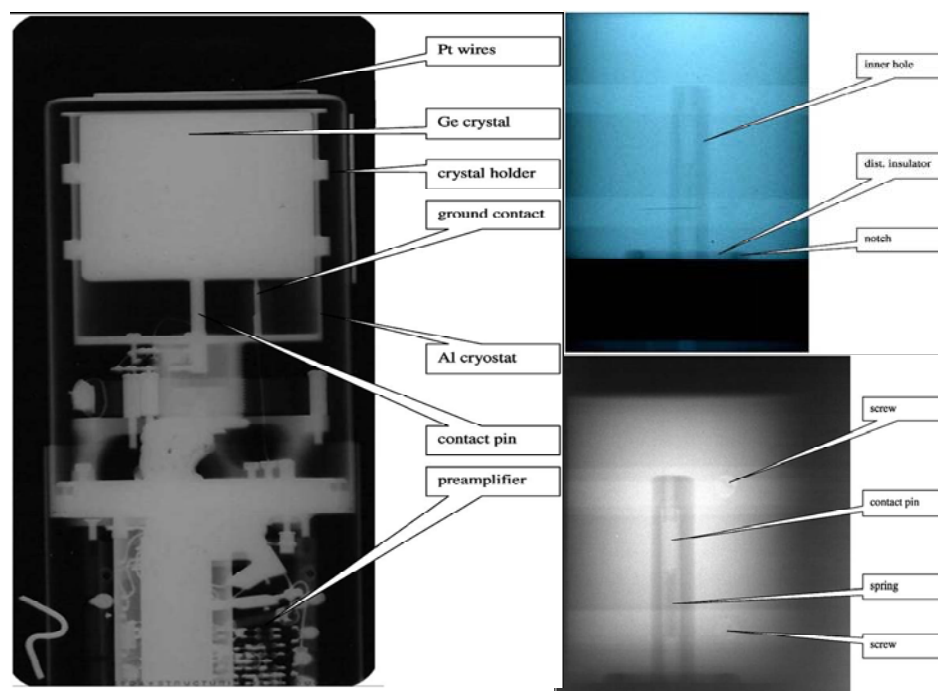


Figure 5.1 X-ray and gamma ray radiographs of an HPGe detector [Dryak and Kovar (2006)].

Windows and dead layers

The photons before reaching the detector have to pass through the detector window and dead layer in front of the crystal and are subjected to attenuation in these materials depending upon their Z . This absorption or scattering of the gamma ray in these materials are the ones responsible for the peaked nature of the efficiency curve. This is because although the interaction probability of a gamma ray decreases with increasing gamma ray energy but the lower energy gamma rays are absorbed in the detector window and dead layers, due to which the probability of low energy gamma rays reaching the crystal decreases. Due to this, as gamma ray energy increases, the efficiencies first increases, reaches a maximum and then decreases. The dead layer thickness specified by the manufacturer is frequently inaccurate. Also, it has been observed that there can be increase in dead layer thickness from 0.35 mm to 1.16 mm after 9 years of operating time [Huy et al. (2007)]. The inhomogeneity in the dead layer thickness has also been shown by Debertain and Grosswendt (1982) and Keyser (2004). The average dead layer thickness is generally measured by measuring the attenuation of a collimated photon beam. The average dead layer thickness on front face and on the cylindrical side of the crystal has been measured by using ^{241}Am source [Budja's et al. (2009)]. Another method [Forcinal (1973), Pessara (1983)] to measure the thickness of a material takes advantage of the abrupt change in the mass attenuation coefficient near the K-edge of the material. The ratio of the peak counts of photons just above the K-edge and just below the K-edge is used to calculate the thickness of the dead layer, assuming that the change in efficiency in such a small energy range is negligible. This method has been used to determine the thickness of Ge dead layer. The mass attenuation coefficient of Ge changes from $\mu/\rho =$

27 cm²g⁻¹ below the K-edge at 11.1 keV to 209 cm²g⁻¹ above it. ⁷⁵Se source is used as it emits As X-rays with the K_α lines at 10.5 keV slightly below and the K_β lines at 11.7 keV slightly above the Ge K-edge and the thickness can be obtained from the equation:

$$\frac{N_\alpha}{N_\beta} = 6.55e^{0.073t} \quad (5.1)$$

where N_α and N_β are the counts in the K_α and K_β peaks and t is the thickness of Ge dead layer in μm . Baker et al. (1987) determined the Be-window and Si-dead layer thickness by making measurements at several energies, above and below the Si K-edge, with well-collimated X-ray beams, incident normal to the detector surface and at an angle of 38.5° to the normal. Another method available in literature for measuring gold contact and silicon dead layer of a Si(Li) detector is by exciting the gold and silicon dead layer atoms with photons of energy greater than the gold L- and silicon K-absorption edges and measuring the characteristic Au L, and Si K X-rays [Maenhaut & Raemdonck (1984), Shima (1980)]. Another method for determining the thicknesses of different absorbing layers including end-cap thickness is based on positioning the source collimator at two places such that photon beam could hit the detector surface at two different angles of incidence relative to the crystal surface, 45° and 90° [Dryak and Kovar (2006), Van Riper et al. (2002), Boson (2008)]. The thickness of the absorbing layers can then be calculated from the relative change in the count rate between the two angles. Nir-El and Sima (2001) have also used ultrasound probe measurements to verify the thickness of the end cap.

5.3.2 Effect of Detector Parameters on the FEP Efficiency

The effect of different detector parameters on the FEP efficiency has been studied in literature [Vargas et al. (2002), Kamboj and Kahn (2003)]. Vargas et al. (2002) varied detector parameters such as crystal diameter, crystal length, diameter of the internal core, and the position of the crystal with respect to the Be window and observed that the efficiency varies significantly with the crystal diameter and its position. It has been observed that it is the detector overall volume and not the detector diameter or length that has a major effect on the FEP efficiency [Kamboj and Kahn (2003)]. Bochud et al. (2006) observed that along with the crystal diameter and length, it is the dead layer in front of the detector surface which affects largely the detector's efficiency. The influence of dead layer thickness on the detector efficiency response has also been studied [Ródenas et al. (2003)]. They observed that increase of dead layer thickness leads to the decrease in the detector's efficiency, not only due to attenuation of gamma rays in the dead layer but also due to the reduction of the active volume of the detector.

5.3.3 Optimization of Detector Geometry

Due to the uncertainty in the detector parameters, which may result in uncertainty in efficiency calculation by Monte Carlo method, a general approach has evolved whereby the different detector parameters are optimized to reproduce the experimental point source efficiencies as a function of energy. Subsequently, efficiency for other geometries can be obtained accurately using the optimized detector parameters. Crystal dimensions such as the crystal diameter, length and crystal front dead layer thickness has been adjusted and results have been obtained with a relative deviation of 5-10% [Liye et al.

(2004), Binqun et al. (2005), Bochud et al. (2006)]. Tzika et al. (2010) optimized the detector geometry by changing the dead layer thickness and could get an overall agreement of 10%. Karamanis (2003) also increased Ge-Al end cap distance by 8 mm and the entrance Li dead layer by 600 μm to get results within 5%. In EUROMET exercise [Lepy et al. (2001)], it was concluded that most of the simulation codes can be used for routine measurements where uncertainties of 5-10% in efficiencies are acceptable. There is literature where much better accuracy ($< 2\%$) has been obtained by optimizing the detector geometry [Helmer et al. (2003), Hardy et al. (2002), Wang et al. (2002)]. Budjas et al. (2009) could obtain an accuracy of $\sim 3\%$ by adjusting the dead layer thickness and inner hole radius of a p-type detector.

5.4 Objective of the Work

The aim of this work was to optimize the HPGe detector parameters that is routinely used in our lab for gamma spectrometric measurements. This was done by using experimental efficiencies for standard geometries such as point sources. The optimized detector parameters have been used for efficiency transfer to other geometries. Results are discussed in the light of existing observations in the literature.

5.4.1 Gamma Spectrometric Measurements

The detector used in the present work was a closed end co-axial p-type DSG HPGe detector. The detector had a 20% relative efficiency and a resolution of 2.1 keV for the ^{60}Co gamma ray at 1332 keV. The schematic diagram of the detector geometry as specified by the manufacturer is shown in Figure 5.2.

The detector was first calibrated for its efficiency by counting point sources of standard ^{133}Ba and ^{152}Eu at 21.7 cm from the detector end cap. Such a large distance was chosen for efficiency calibration with these multi-gamma sources so as to avoid any uncertainty in the efficiency curve due to coincidence summing. The counting of the samples was done for a sufficiently long time so as to keep statistical uncertainty less than a percent.

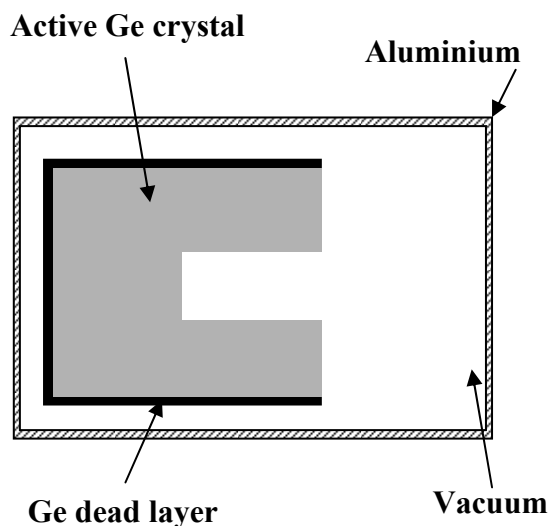


Figure 5.2 Schematic diagram of the detector geometry supplied by the manufacturer.

All the spectra were analyzed by PHAST software [Mukhopadhyaya (2001)], the detail of which is given in Chapter 2. The Eu-Ba efficiencies were fitted into a fourth order log-log polynomial curve by non-linear least square fitting. These efficiencies were then used to obtain dps of point sources of ^{109}Cd , ^{57}Co , ^{203}Hg , ^{51}Cr , ^{137}Cs and ^{65}Zn prepared from the activities procured from Board of Radiation and Isotope Technology, Mumbai. For this, these sources were also counted at $d = 21.7$ cm. The monoenergetic sources were then used to determine FEP efficiencies (ϵ_γ) at closer distances ($d = 1.7$ and 12.6 cm) by using the experimentally determined disintegration rate (dps) given by:

$$\varepsilon_{\gamma} = \frac{cps}{I_{\gamma} \times dps} \quad (5.2)$$

where *cps* is the count rate at the energy of interest and I_{γ} is the gamma ray emission probability taken from Table of Isotopes [Firestone (1996)]. The count rates were corrected for the background peak counts in all the cases.

Similarly, 5 ml sources of ^{109}Cd , ^{57}Co , ^{203}Hg , ^{137}Cs and ^{65}Zn were calibrated using standard 5 ml sources of ^{152}Eu and ^{133}Ba in same HPGe detector at $d = 10.3$ cm. Such a large distance was chosen so that the coincidence summing effects are negligible. These sources were then used to obtain efficiencies at $d = 2.0$ cm. Also, 100 ml standard source of ^{152}Eu taken in a glass bottle was counted in the same HPGe detector at $d = 19.8$ cm and FEP efficiencies were determined.

5.4.2 Monte Carlo Simulation

In this work, the version MCNP4c [Briesmeister (2000)] was used to simulate the HPGe detector response. This code tracks the particle from its origin to the point of its complete absorption. All primary as well as secondary interactions are taken into account. The efficiency was obtained with *F8* tally which is a pulse height tally without any variance reduction. Mode *P* was used. The description of the detector geometry was given in detail in the cell and surface cards of the MCNP input file. The detector housing including the absorbing materials (aluminum end cap, germanium dead layer), were all included in the geometry. In each run $\sim 10^8$ particles were sampled to reduce statistical uncertainties.

5.4.3 Comparison of MCNP and Experimental Efficiencies

Initial MCNP simulations were performed for point source geometry with the dimensions of the detector obtained from manufacturer as given in the second column of Table 5.3. The MCNP simulated and experimental values of the FEP efficiencies are shown in Figure 5.3. The error on experimental efficiencies is also shown in the figure and is obtained by propagating the error on peak areas, abundances and efficiency fitting error. The error bars are of the size of the symbol.

Table 5.3 Detector parameters provided by manufacturer and optimized by MCNP simulation.

Description	Manufacturer supplied value (mm)	Optimized value (mm)
Crystal radius	24.55	23.65
Crystal length	49.9	49.9
Front Ge dead layer thickness	0.6	0.7
Side Ge dead layer thickness	0.6	0.6
Inner hole radius	4.25	4.25
Inner hole depth	38.4	38.4
Al end cap thickness	0.7	0.7
Al end cap to crystal distance	3	9

At all sample-to-detector distances ($d = 1.7$ cm, 12.6 cm and 21.7 cm), the MCNP efficiencies were found to be higher than the experimental values indicating the inadequacy of the manufacturer supplied detector dimensions. Similar observations have

also been made in literature [Helmer et al. (2003), Budja'sˇ et al (2009), Vargas et al. (2002), Laborie et al. (2000)]. A more detailed comparison of the MCNP and experimental efficiencies at $d = 1.7$ cm, 12.6 cm and 21.7 cm has been given in Table 5.4. At a particular distance, the ratios of MCNP to experimental efficiencies were observed to be constant within 2-4% over the energy range of 88-1115 keV. But, these ratios were found to vary strongly from one distance to other with the MCNP to experimental ratio being higher at closer distance. It can be seen from the table that the average MCNP to experimental ratio at $d = 21.7$ cm is 1.14 while it increases to 1.20 at $d = 12.6$ cm and to 1.46 at $d = 1.7$ cm. This indicates that the detector parameters have to be adjusted such that the constancy of ratio of efficiency over the energy range is not disturbed but the strong dependency on the sample-to-detector distance is removed.

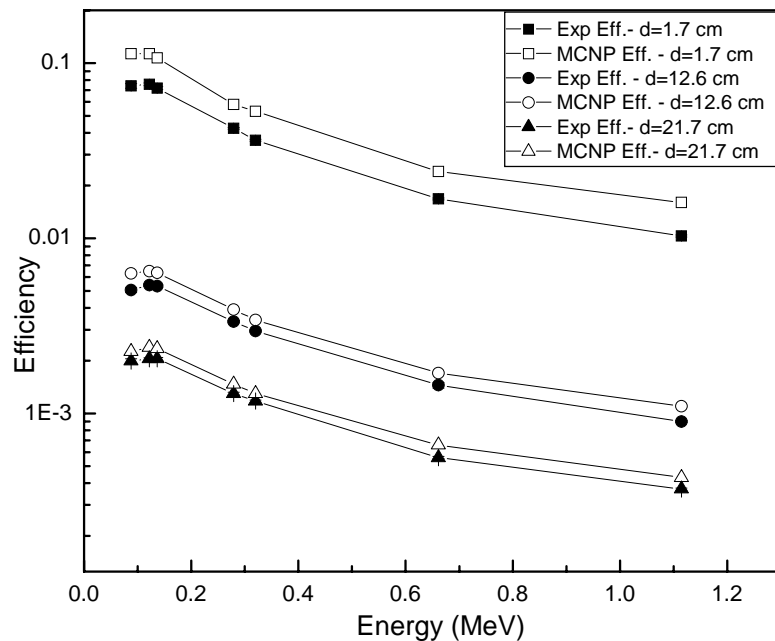


Figure 5.3 Experimental and MCNP simulated FEP efficiency for point source geometry using the manufacturer supplied detector geometry at three sample-to-detector distances, $d = 1.7$ cm, 12.6 cm and 21.7 cm.

5.5. Optimization of different detector parameters

There are a number of geometrical parameters which can be uncertain like detector crystal radius, its length, inner hole radius and length, dead layer thickness, Al end cap thickness, the Al end cap to detector crystal distance. The effect of systematic change in these parameters on the FEP efficiency is discussed in the following.

Table 5.4 The comparison of experimental and MCNP efficiencies at three sample-to-detector distances, $d = 1.7$ cm, 12.6 cm and 21.7 cm. The detector geometry used has been provided by the manufacturer.

Energy (MeV)	d = 1.7 cm			d = 12.6 cm			d = 21.7 cm		
	MCNP eff	Exp eff	MCNP /Exp	MCNP eff	Exp eff	MCNP /Exp	MCNP eff	Exp eff	MCNP /Exp
0.088	0.1132	0.0741	1.53	0.0063	0.0051	1.24	0.0023	0.0020	1.14
0.122	0.1126	0.0757	1.49	0.0065	0.0054	1.20	0.0024	0.0020	1.16
0.136	0.1073	0.0720	1.49	0.0064	0.0053	1.19	0.0023	0.0020	1.14
0.279	0.0579	0.0424	1.36	0.0039	0.0033	1.17	0.0015	0.0013	1.13
0.320	0.0525	0.0363	1.44	0.0034	0.0030	1.16	0.0013	0.0012	1.11
0.661	0.0238	0.0168	1.41	0.0017	0.0015	1.17	0.0007	0.0006	1.17
1.115	0.0155	0.0103	1.50	0.0011	0.0009	1.22	0.0004	0.0004	1.15
		Avg.	1.46		Avg.	1.20		Avg.	1.14
		Std.	0.06		Std.	0.03		Std.	0.02
		Dev.			Dev.			Dev.	
		% RSD	3.92		% RSD	2.52		% RSD	1.90

5.5.1 Detector Crystal Geometry

Since crystal dimensions have been reported to have major effect on the detector efficiency, the radius of the detector was reduced by 1 mm and detector efficiency was computed by MCNP at $d = 1.7$ and 21.7 cm. Table 5.5 gives the comparison of FEP experimental and MCNP efficiency results. The average efficiency ratio has reduced from 1.46 to 1.36 at 1.7 cm and from 1.14 to 1.03 at $d = 21.7$ cm. The detector radius was further reduced by 1 mm, to see if the ratio further reduces and approaches unity. As given in Table 5.5, although at $d = 1.7$ cm, the ratio has reduced to 1.16 but it became less than 1 at $d = 21.7$ cm. Thus, it can be concluded that the reduction in crystal radius by 1 mm can reproduce the experimental efficiency at long distance, but at shorter distance ($d = 1.7$ cm), the discrepancy still exists. Since the MCNP to experimental ratio should be close to unity at all sample-to-detector distance, variation of crystal radius alone is not sufficient to match MCNP and experimental efficiency.

Since the crystal length can also have appreciable effect on efficiency, as a next step, it was reduced by 4.9 mm keeping the inner hole length constant, and as given in Table 5.5, the average MCNP to experimental ratio at both the distances decreased by about 2-3% only even after a reduction of detector length by 10%. Since the value of length quoted by the manufacturer could not be erroneous by more than 10%, this parameter was not further changed and its original value was restored. The increment in inner hole radius to 5.75 mm and thereby reduction in the overall detector volume, as given in Table 5.5, introduced energy dependence which was earlier not present with the manufacturer supplied detector geometry. This was expected as the lower energy gamma rays will be absorbed in a small detector length and so will not be affected by increasing the inner

hole radius but some part of the high energy gamma rays will escape due to increase in the inner hole radius. Therefore, in the present case, this was not the parameter to be changed.

Table 5.5 The ratio of MCNP and experimental efficiencies at two sample-to-detector distances, $d = 1.7$ cm and 21.7 cm. The MCNP efficiencies are computed by changing some detector crystal parameters to see its effect on the detector efficiency.

Energy (MeV)	Crystal radius reduced by 1 mm	Crystal radius reduced by 2 mm	Crystal length reduced by 4.9 mm	Inner hole radius increased by 5.75 mm	Dead layer thickness increased by 0.4 mm					
						FEP efficiencies (MCNP/Exp)				
						d = 1.7 cm				
0.088	1.46	1.31	1.53	1.53	1.29					
0.122	1.41	1.25	1.49	1.44	1.37					
0.136	1.41	1.24	1.49	1.40	1.40					
0.279	1.27	1.08	1.35	0.95	1.33					
0.320	1.34	1.13	1.42	1.33	1.41					
0.661	1.29	1.05	1.36	1.22	1.39					
1.115	1.36	1.09	1.43	1.26	1.48					
Avg.	1.36	1.16	1.44	1.31	1.38					
Std. Dev.	0.07	0.10	0.07	0.19	0.06					
% RSD	5.04	8.58	4.69	14.36	4.37					
	d = 21.7 cm									
0.088	1.05	0.88	1.14	1.13	0.99					
0.122	1.07	0.89	1.16	1.14	1.09					
0.136	1.04	0.88	1.13	1.11	1.08					
0.279	1.03	0.84	1.10	1.02	1.11					
0.320	1.00	0.81	1.07	0.97	1.08					
0.661	1.06	0.83	1.11	0.97	1.17					
1.115	1.02	0.79	1.06	0.91	1.13					
Avg.	1.04	0.85	1.11	1.04	1.09					
Std. Dev.	0.02	0.04	0.04	0.09	0.06					
% RSD	2.26	4.48	3.22	8.72	5.06					

The detector efficiency also depends upon the dead layer thickness, as low energy photons may be highly attenuated in it. The influence of dead layer thickness on the detector efficiency was seen by increasing the dead layer thickness by 0.4 mm. There was a reduction of only 4-5% in the MCNP to experimental efficiency ratios as given in Table 5.5 after an increase in dead layer thickness by 67%. From this, it was concluded that, in our case the detector crystal parameters are not the one responsible for such a high efficiency ratio of 1.46 at $d = 1.7$ cm.

5.5.2 Detector End Cap Thickness and End Cap to Crystal Distance

Since the effect of increasing the thickness of Al end cap will be similar and less in magnitude to increasing the Ge dead layer thickness, the Al thickness was not changed. The distance between the Al end cap and detector crystal (d_{alc}) was increased by 3 mm and MCNP efficiencies were computed at $d = 1.7$ and 21.7 cm. Table 5.6 gives the MCNP and experimental efficiency values and their ratios. The MCNP efficiencies at 1.7 cm decreased by about 13% while the efficiencies at $d = 21.7$ cm reduced by only 2%. Since in our case, there is distance dependence in the MCNP to experimental ratio with the ratio being higher at closer distance, the Al end cap to crystal distance was identified as the main cause of discrepancy between MCNP and experimental efficiency values. This is in accordance with Hardy et al. (2002) who observed an uncertainty of ~36% in the Al end cap to crystal distance. The d_{alc} was then systematically changed and the results are presented in Table 5.6. When the Al end cap to crystal distance is kept as 8 mm, the ratio of efficiencies was further decreased, but still a difference between the efficiency ratios at $d = 1.7$ cm and 21.7 cm could be seen. The principle of efficiency

transfer says that this difference should not exist, the Al end cap to crystal distance was further incremented in steps to 1 mm. The results are given in Table 5.6. It could be seen that as the Al end cap to crystal distance was increased, the ratios of MCNP to experimental efficiencies at $d = 1.7$ cm and 21.7 cm came closer and almost coincided at Al end cap to crystal distance of 9 mm and after that again diverged. This indicates that the Al end cap to crystal distance should be taken as 9 mm instead of 3 mm (quoted by the manufacturer) to get a MCNP to experimental efficiency ratio independent of sample-to-detector distance.

Experimental validation

To experimentally verify the deviation in Al end cap to crystal distance from the manufacturer supplied value, the detector was axially scanned. For this a ^{109}Cd source was used and its count rate was measured through a 3 mm collimator in touching configuration with detector. Figure 5.4 gives the axial profile from the surface of the detector. It can be seen that the count rate is minimum at 3 mm from the detector surface and increases only after 5 mm and becomes maximum at 15 mm so that the average distance of Al end cap to crystal distance can be roughly considered as 10 mm. However a better estimate is expected if the collimator diameter is reduced to 1 mm.

But, the MCNP efficiencies were still found to be 10% higher than the experimental values at both the sample-to-detector distances. Further optimization was carried out to bring this factor close to unity. Previously, from Table 5.5, it was observed that when the detector radius is reduced by 1 mm, the efficiency ratio also reduces by about 7-9% at the two sample-to-detector distances. This will bring the efficiency ratio close to 1 if the

optimized Al end cap to detector crystal distance is used for MCNP calculation. Thus, the radius of the detector crystal was systematically reduced; keeping the optimized Al end cap to crystal distance as 9 mm and efficiency ratios at two distances were obtained. Initially, when the radius was reduced by 0.8 mm, the efficiency ratio at the two distances, $d = 1.7$ and 21.7 cm, reduced to 1.03 and 1.01 respectively (Table 5.7). This indicates that the ratio is approaching 1 as desired.

Table 5.6 The comparison of experimental and MCNP efficiencies at two sample-to-detector distances, $d = 1.7$ cm and 21.7 cm. The MCNP efficiencies are computed by changing the Al end cap to detector crystal distance (d_{alc}) to see its effect on the detector efficiency.

Energy (MeV)	$d_{alc} = 3$ mm	$d_{alc} = 6$ mm	$d_{alc} = 8$ mm	$d_{alc} = 8.5$ mm	$d_{alc} = 9$ mm	$d_{alc} = 10$ mm
FEP efficiencies (MCNP/Exp)						
d = 1.7 cm						
0.088	1.53	1.32	1.21	1.18	1.15	1.10
0.122	1.49	1.28	1.17	1.14	1.11	1.07
0.136	1.49	1.29	1.17	1.14	1.12	1.07
0.279	1.36	1.18	1.08	1.06	1.03	0.99
0.320	1.44	1.25	1.14	1.11	1.09	1.04
0.661	1.41	1.22	1.12	1.10	1.07	1.03
1.115	1.50	1.30	1.19	1.16	1.14	1.09
Avg.	1.46	1.26	1.15	1.13	1.10	1.05
Std. Dev.	0.06	0.05	0.04	0.04	0.04	0.04
% RSD	3.92	3.86	3.77	3.76	3.78	3.71
d = 21.7 cm						
0.088	1.14	1.11	1.09	1.08	1.08	1.07
0.122	1.16	1.13	1.11	1.11	1.10	1.10
0.136	1.14	1.12	1.10	1.09	1.09	1.07
0.279	1.13	1.11	1.09	1.09	1.08	1.07
0.320	1.11	1.08	1.06	1.05	1.05	1.04
0.661	1.17	1.15	1.13	1.13	1.12	1.13
1.115	1.15	1.12	1.10	1.10	1.10	1.09
Avg.	1.14	1.12	1.10	1.09	1.09	1.08
Std. Dev.	0.02	0.02	0.02	0.02	0.02	0.03
% RSD	1.90	2.02	2.02	2.03	2.02	2.48

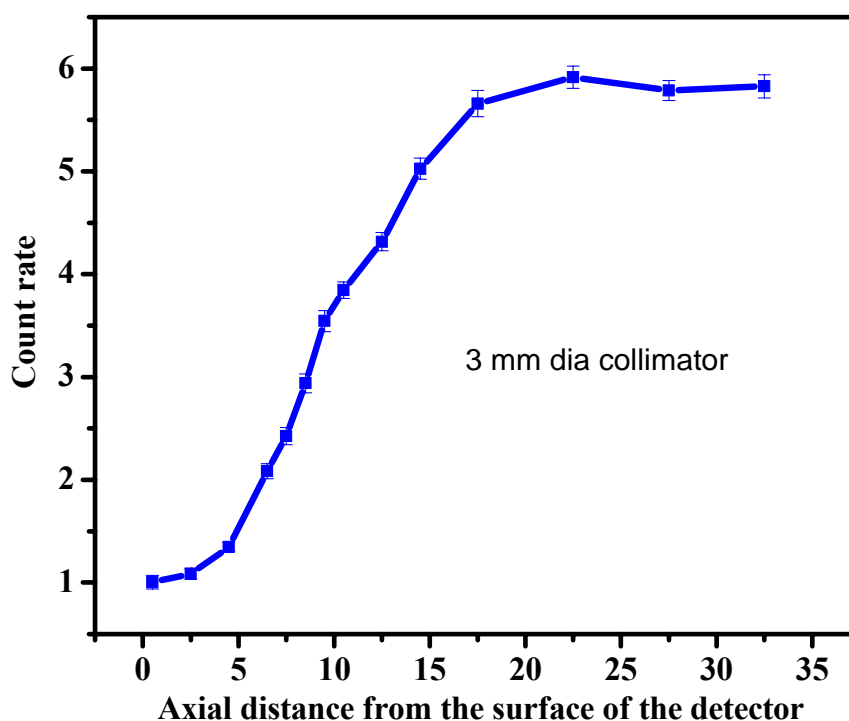


Figure 5.4 Axial profile of a collimated ^{109}Cd source from the surface of the detector.

Therefore, the radius was further reduced systematically in steps of 0.1 mm and the results are given in Table 5.7. When the radius is reduced by 0.9 mm, the average ratio at $d = 1.7$ cm and 21.7 cm was found to be close to unity, indicating that the manufacturer supplied crystal radius should be reduced by 0.9 mm to match the MCNP efficiencies with experimental efficiencies. But still at $d = 1.7$ cm, a slight systematic bias showing its dependence on energy was observed. The ratio of MCNP and experimental efficiencies was found to be higher at lower energies (1.10 at 88 keV) compared to higher energies (1.00 at 1115 keV). To remove this slight energy dependence, the dead layer thickness was increased by 0.1 mm. These calculations were done using the optimized Al end cap

to crystal distance and the optimized detector crystal radius. With this variation, the efficiency ratios were found to be within 5% at all energies and over all sample-to-detector distances. The experimental and the MCNP efficiencies calculated using this optimized geometry has been shown in Figure 5.5. The detector parameters for the optimized geometry have been given in the last column of Table 5.3.

Vargas et al. (2002) reported the effect of systematic variation of detector parameters on the simulated efficiencies of point and volumetric sources. The study showed that slight variation of detector parameters could lead to significant variation in detector efficiency. Of particular importance in the context of the present work, is the variation of efficiencies with the Al end cap to crystal distance for different source geometries. It has been observed [Vargas et al. (2002)] that this distance is critical for volumetric sources, but less important for point sources. However, our studies show that there is a strong distance dependence of simulated efficiencies with respect to experimental efficiencies for point sources also when manufacturer supplied detector parameters are used. It was also observed that this can be eliminated by adjusting the Al end cap to crystal distance.

Table 5.7 The comparison of experimental and MCNP efficiencies at two sample-to-detector distances, $d = 1.7$ cm and 21.7 cm. The MCNP efficiencies are computed by taking the optimized Al end cap to detector crystal distance as the basis and carrying out further optimization by changing the detector radius and dead layer thickness.

Energy (MeV)	Al end cap to crystal distance, $d_{alc} = 9$ mm			
	Nominal values of all other detector parameters	Crystal radius reduced by 0.8 mm	Crystal radius reduced by 0.9 mm	Crystal radius reduced by 0.9 mm and dead layer increased by 1 mm
	FEP efficiencies (MCNP/Exp)			
	d = 1.7 cm			
0.088	1.15	1.10	1.10	1.05
0.122	1.11	1.06	1.05	1.03
0.136	1.12	1.06	1.06	1.04
0.279	1.03	0.97	0.96	0.95
0.32	1.09	0.98	0.97	0.96
0.661	1.07	1.00	0.99	0.98
1.115	1.14	1.01	1.00	0.99
Avg.	1.10	1.03	1.02	1.00
Std. Dev.	0.04	0.05	0.05	0.04
% RSD	3.78	4.96	5.10	3.97
	d = 21.7 cm			
0.088	1.08	1.01	1.00	0.97
0.122	1.10	1.03	1.02	1.00
0.136	1.09	1.01	1.00	0.99
0.279	1.08	1.00	0.99	0.98
0.32	1.05	0.97	0.96	0.96
0.661	1.12	1.03	1.01	1.01
1.115	1.10	1.00	0.99	0.98
Avg.	1.09	1.01	1.00	0.98
Std. Dev.	0.02	0.02	0.02	0.02
% RSD	2.02	1.84	1.87	1.77

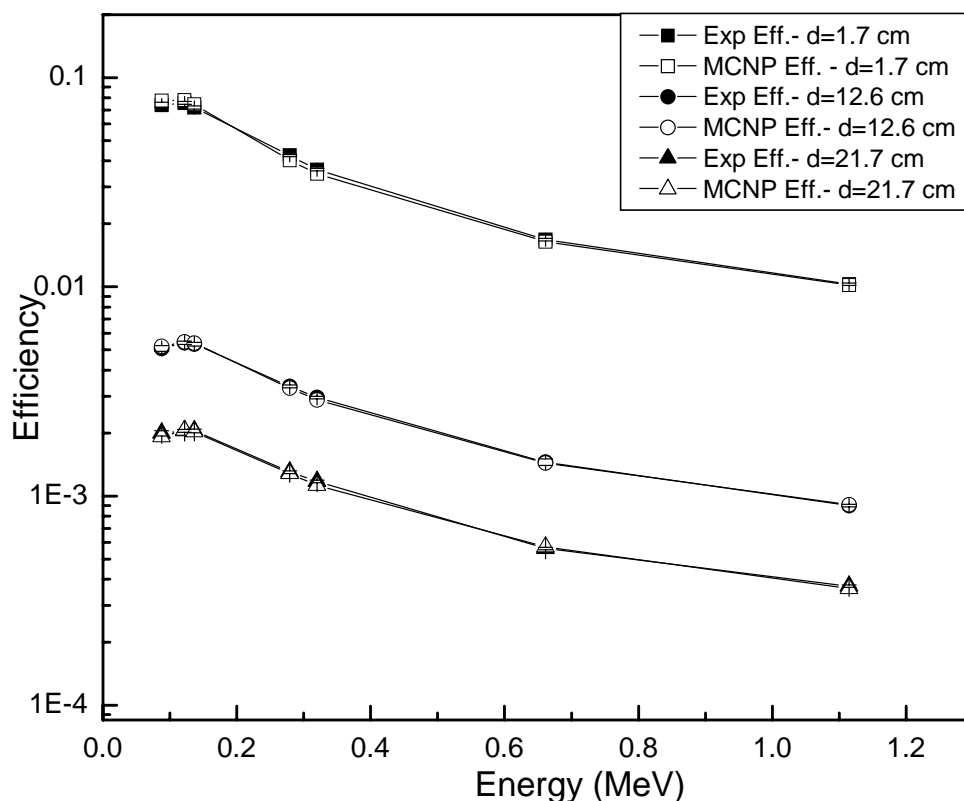


Figure 5.5 Experimental and MCNP simulated FEP efficiency for point source geometry using the optimized detector geometry at three sample-to-detector distances, $d = 1.7$ cm, 12.6 cm and 21.7 cm.

5.6 Efficiency Transfer to Volumetric Sources

In accordance with the principle of efficiency transfer, this optimized geometry should be valid for all the extended sample geometries. As a check of the optimized geometry, the efficiencies of 5 ml aqueous solutions of ^{109}Cd , ^{57}Co , ^{203}Hg , ^{137}Cs and ^{65}Zn in cylindrical vials at $d = 2.0$ and 10.3 cm were compared with the MCNP calculated efficiencies. The MCNP efficiencies for these samples were calculated using the optimized detector geometry and the detailed sample geometry. Table 5.8 gives the ratio of experimental and

MCNP efficiencies for 5 ml sources. The two efficiencies differ by about 7% at $d = 2.0$ cm and by 3% at $d = 10.3$ cm for this extended geometry.

Table 5.8 Ratios of MCNP to experimental efficiencies for 5 ml sources of ^{109}Cd , ^{57}Co , ^{203}Hg , ^{137}Cs and ^{65}Zn and for 100 ml ^{152}Eu source.

Energy (MeV)	5 ml		Energy (MeV)	100 ml
	d=2.0 cm	d = 10.3 cm		d=19.8 cm
0.088	1.11	1.07	0.122	1.04
0.122	1.07	1.05	0.244	1.03
0.136	1.06	1.01	0.344	1.01
0.279	1.12	1.03	0.779	1.03
0.661	1.01	1.02	0.867	1.02
1.115	1.01	1.02	0.964	1.01
			1.112	1.04
			1.408	1.02
Avg.	1.07	1.03	Avg.	1.02
Std. Dev.	0.05	0.02	Std. Dev.	0.01
% RSD	4.46	2.06	% RSD	1.21

The validity of the optimized geometry was also checked for another extended source of standard 100 ml ^{152}Eu . The experimental efficiencies at $d = 19.8$ cm for this geometry were compared with the efficiencies calculated by using MCNP. The ratios of the two efficiencies are given in the last column of the Table 5.8. In this case also, the two efficiencies are within 3-4%. The slight difference in the efficiencies for volumetric samples at closer distance can be due to some inaccuracy in sample geometry such as its radius, glass thickness, its density and height. This has also been observed by Johnston et al. (2006) and Vargas et al. (2002) where it was concluded that the sample dimensions could have a significant effect on the detector efficiency. However our results of

simulated efficiencies using adjusted detector parameters based on point source efficiencies can be used for volumetric sources also and one can get results within 5%.

5.7 Conclusion

The MCNP can be used to get efficiencies for any sample geometry, once the detector geometry has been optimized to match the experimental and MCNP efficiencies. It is particularly useful when the standards are not available.

True Coincidence Summing Corrections

- 6.1 Introduction
- 6.2 True Coincidence Summing
 - 6.2.1 *General Overview*
 - 6.2.2 *Factors affecting true coincidence summing*
 - 6.2.3 *Methods for coincidence correction*
- 6.3 Objective of the work
- 6.4 Gamma spectrometric measurements
 - 6.4.1 *Standardization of gamma sources*
 - 6.4.2 *Efficiencies of point sources at different distances*
- 6.5 Coincidence summing correction for point source geometry
 - 6.5.1 *Coincidence summing correction factors by analytical method*
 - 6.5.2 *Validation of the analytical method*
 - 6.5.3 *Application of the method*
- 6.6 Coincidence summing correction for volumetric sources
- 6.7 Conclusion

6.1 Introduction

As discussed in Chapter 1 of this thesis, true coincidence summing (TCS) is one of the factors which may lead to non-proportionality between the measured count rate and the mass of the nuclide monitored. True coincidence summing takes place when two or more gamma rays (or a gamma ray and an X-ray) which are emitted in a cascade from an excited nucleus are detected within the resolving time of the detector. As a result, the detector cannot distinguish between the two interactions, and treats them as a single event, the energy transfer being the sum of the two interactions. This leads to a loss in count from the peaks corresponding to two gamma rays and addition of count at the sum of two energies. This results in inaccurate count rate and hence erroneous results. The coincidence correction factor (k_{TCS}) is defined as the ratio of the count rate in absence of the coincidence to the count rate in presence of coincidence:

$$k_{TCS} = \frac{\text{Count rate (or } \varepsilon \text{) in absence of coincidence}}{\text{Count rate (or } \varepsilon \text{) in presence of coincidence}} \quad (6.1)$$

6.2 True Coincidence Summing

6.2.1 General Overview

If two gamma rays with energies E_1 and E_2 are in coincidence with each other, then there may be summing in and summing out effects resulting from the addition of counts at the energy corresponding to the sum of two energies ($E_1 + E_2$) and loss of counts from the two peaks (E_1, E_2) respectively. For example, ^{60}Co decays by β^- to ^{60}Ni and emits 1173 and 1332 keV gamma rays in cascade (Figure 6.1). These two gamma rays may reach the detector at the same time and can sum up to give counts at 2505 keV in the spectrum. The

loss in count rate at 1173 keV and 1332 keV is known as summing out event. In this case since a peak at 2505 keV already exists although the probability is very low, so there will be an increase in counts at that peak and this is known as summing in event. When there is no gamma ray corresponding to E_1+E_2 then new peak may appear at this energy. In the former case, the correction factor (as given by equation 6.1) will be less than unity and in the latter case it will be greater than unity.

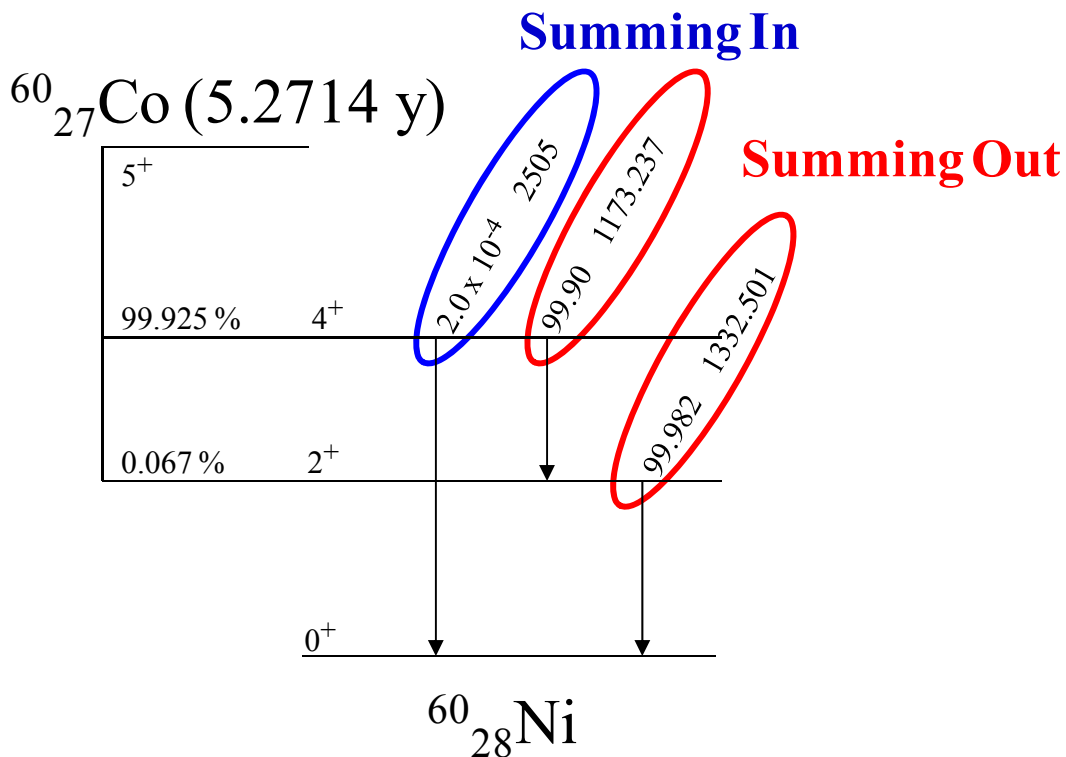


Figure 6.1 True coincidence summing effects in the beta decay of ^{60}Co .

Each sum peak represents only a small part of the total counts lost from the full energy peaks. This is because there will be a chance of summing of a particular gamma ray with each and every gamma ray in the cascade whether or not fully absorbed. In fact, since only a minority of gamma rays is fully absorbed, the summing of a gamma ray destined for a full energy peak with an incompletely absorbed gamma ray is more likely.

Therefore, the coincidences with partially absorbed gamma rays must be taken into account if a TCS correction is to be done.

6.2.2 Factors Affecting True Coincidence Summing

The extent of coincidence summing depends upon the probability that two gamma rays emitted simultaneously will be detected simultaneously [Gilmore (2008)]. Therefore, these effects are independent of count rate of the source and depend solely on the emission probabilities and detection efficiencies of the cascade gamma rays. The emission probabilities of different gamma rays are characteristic of the radionuclide under study. The detection efficiencies are function of the solid angle subtended by the source at the detector i.e., the source-to-detector distance and the area of the detector front face. As shown in Figure 6.2, if there are two sources $S1$ and $S2$ of equal strengths with $S1$ placed on the detector end cap and $S2$ placed at some distance, since the solid angle subtended by $S1$ will be greater than $S2$, the probability of the two gamma rays reaching the detector simultaneously will be more in the former case leading to significant coincidence corrections at closer distance.

6.2.3 Methods for Coincidence Correction

The coincidence summing corrections can be avoided by counting the sample far from the detector, so that the probability of two gamma rays reaching the detector at the same time is negligible. This is quite impractical for samples with low activity eg. environmental samples where the samples are required to be counted as close as possible to the detector. Another way to avoid coincidence summing corrections is to use a gamma ray standard of the same radionuclide as the one monitored. This may be practical

for a routine lab where few radionuclides are monitored and one can have a set of standards corresponding to those nuclides. But if a variety of samples are to be analyzed such as environmental, fission product, activation product samples etc. then to have gamma ray standards of all the radionuclides is next to impossible and it is better to apply true coincidence summing correction. As an example, the importance of TCS corrections has been discussed in ref. [Garcia-Talavera et al. (2001)] for the measurement of radionuclides in natural decay series using gamma ray spectrometry.

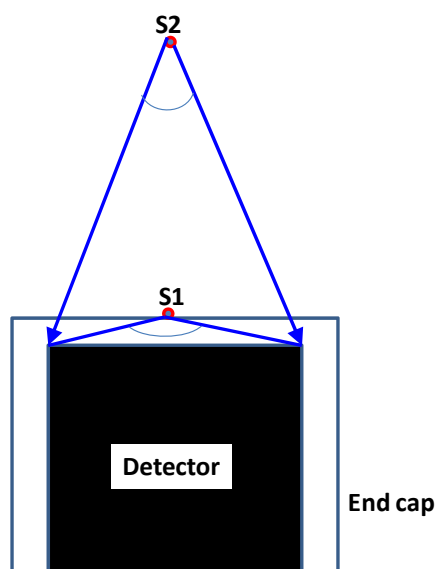


Figure 6.2 Effect of solid angle on true coincidence summing effects.

Analytical approach

A general method for computing coincidence correction factors was first demonstrated by Andreev et al. (1972) and has been further developed and applied in practice by other authors [Andreev et al. (1973), Debertin and Schotzig (1979), McCallum and Coote (1975), Sinkko and Aaltonen (1975), Schima and Hoppes (1983), Dryak and Kovar

(2009), Corte and Freitas (1992), Montgomery and Montgomery (1995), Kafala (1995), Sundgren (1993), Richardson and Sallee (1990)]. This is an analytical approach which requires the use of full energy peak and total efficiencies and information about the nuclear decay parameters such as the mode of parent nuclide decay, energies of gamma transitions, gamma ray emission probabilities, K-capture probabilities (in electron capture decay), mean energy of K X-rays, fluorescence yield, total and K conversion coefficients etc. All these factors are used to calculate the probability of simultaneous emission of two or more cascade gamma rays.

In this method, the true coincidence correction (k_{TCS}) is, in general given by:

$$k_{TCS} = \frac{1}{1 - \sum_{i=1}^{i=n} p_i \varepsilon_{ii}} \quad (6.2)$$

where, n is total number of gamma rays in coincidence with gamma ray of interest, p_i represents the probability of simultaneous emission of i^{th} gamma and the gamma ray of interest and ε_{ii} represents the total efficiency of i^{th} gamma ray. In order to calculate k_{TCS} by this method, the probability p_i is calculated by taking into account appropriate parameters obtained from the published decay schemes of the radionuclides [Dias et al. (2002)]. This method can be understood in a better way by the following example:

Consider a nuclide X decaying to Y by beta decay as shown in Figure 6.3.

The nuclide X decays to the two excited states of Y . The two excited states deexcite by emission of three gamma rays γ_1 ($2 \rightarrow 1$), γ_2 ($1 \rightarrow 0$) and γ_3 ($2 \rightarrow 0$) with their respective probabilities as p_1 , p_2 and p_3 . In absence of coincidence summing, the count rate is given by:

$$N_{10} = Ap_1\varepsilon_1 \quad (6.3)$$

where A is the disintegration rate of the source and ε_l is the FEP efficiency at energy corresponding to γ_l .

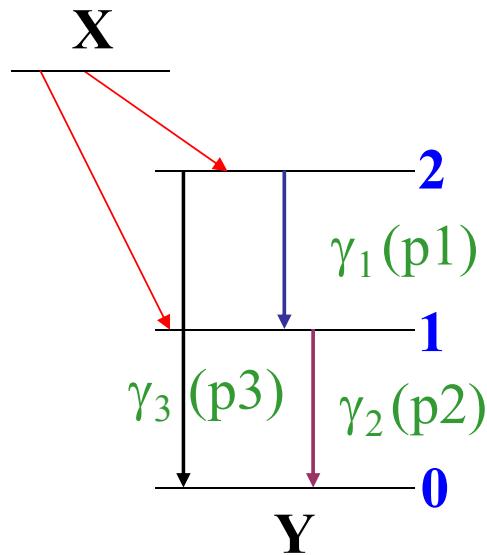


Figure 6.3 A typical decay scheme of a nuclide X decaying to Y.

But, as seen from the figure, in this case, γ_1 and γ_2 are in coincidence with each other. In presence of coincidence summing, the observed count rate N_l will be smaller than N_{l0} :

$$N_l = Ap_1\varepsilon_1 - Ap_1\varepsilon_1\varepsilon_{i2} \quad (6.4)$$

where the last factor denotes the probability of the two gamma rays γ_1 and γ_2 to reach the detector simultaneously. ε_{i2} is the total efficiency of detection of γ_2 . As explained earlier, the loss of counts from the full energy peak of γ_1 may occur due to coincidence with events involving full as well as partial energy deposition of the second gamma ray. Thus the total efficiency ε_{i2} , appears in the equation 6.4. The coincidence correction factor for gamma 1 is given by:

$$C_1 = \frac{N_{10}}{N_1} = \frac{1}{1 - \varepsilon_{t2}} \quad (6.5)$$

Similarly, for gamma 2, the observed count rate N_2 is given by:

$$N_2 = Ap_2\varepsilon_2 - Ap_1\varepsilon_2\varepsilon_{t1} \quad (6.6)$$

Coincidence correction factor for gamma 2:

$$C_2 = \frac{N_{20}}{N_2} = \frac{1}{1 - \left(\frac{p_1}{p_2}\right)\varepsilon_{t1}} \quad (6.7)$$

For gamma 3, the observed count rate N_3 is increased due to summation of γ_1 and γ_2 and is given by:

$$N_3 = Ap_3\varepsilon_3 + Ap_1\varepsilon_1\varepsilon_2 \quad (6.8)$$

Here the second term corresponds to the probability of the two gamma rays γ_1 and γ_2 to simultaneously deposit their full energies in the detector. Therefore, the coincidence correction factor for γ_3 is given by:

$$C_3 = \frac{N_{30}}{N_3} = \frac{1}{1 + \left(\frac{p_1\varepsilon_1\varepsilon_2}{p_3\varepsilon_3}\right)} \quad (6.9)$$

This is the simplest decay scheme where only two gamma rays in coincidence with each other have been considered. Practically the decay schemes can be very complex and a large number of parameters need to be accounted. For example, apart from gamma emission, a nuclide in its excited state may de-excite by internal conversion. So, whatever fraction of γ_1 decays to the level 1 of the decay scheme (Figure 6.3), only a fraction of it

may lead to γ_2 emissions. The rest of the fraction may lead to emission of internal conversion electrons. The probability of γ_2 emission per γ_1 is $1/(1+\alpha_2)$ where α_2 is the internal conversion coefficient defined as the ratio of probability of internal conversion to the probability of gamma emission given as:

$$\alpha = \frac{\text{probability of internal conversion electron emission}}{\text{probability of gamma ray emission}} \quad (6.10)$$

This leads to modification of equation 6.4 as:

$$N_1 = Ap_1\varepsilon_1 - Ap_1 \left(\frac{1}{(1+\alpha_2)} \right) \varepsilon_1\varepsilon_{i2} \quad (6.11)$$

where the additional factor $(1/(1+\alpha_2))$ in the last term indicates the probability of gamma emission in the transition $1 \rightarrow 0$.

Also, there can be loss from the full energy peak of the gamma ray (γ_1) due to coincidence of the gamma ray with the X-rays followed by internal conversion. Therefore probability of gamma and K X-ray to be detected in the detector simultaneously i.e. $\alpha_k \omega_K \varepsilon_1\varepsilon_{iX}/(1+\alpha_T)$ adds in equation 6.11, where α_k and α_T are the K-shell and total internal conversion coefficients respectively and ω_K is the K-shell fluorescence yield defined as the probability that the filling of a hole in the K-shell results in an X-ray emission and not an Auger emission, i.e.

$$\omega_K = \frac{N(X_K)}{N_o} \quad (6.12)$$

where $N(X_K)$ and N_o are the number of emitted X_K rays and K-shell vacancies respectively. Also, since electron capture decay is always accompanied by X-ray emissions, these X-rays are also in coincidence with the gamma rays originating from the level fed by electron capture. The probability of coincidence in this case is given by $P_K \omega_K \varepsilon_I \varepsilon_{IX}$, where P_K is the K-electron capture probability. In this way, depending upon the decay scheme and the gamma ray monitored, the expressions for the coincidence correction factors will be modified.

Along with the nuclear decay parameters, this analytical method also needs full energy peak and total efficiencies over the entire energy range. FEP efficiencies can be obtained by using a set of monoenergetic gamma ray standards or by using a multi-gamma ray standard having non-coincident gamma rays eg. ^{125}Sb . But measurement of the total efficiency is more complicated than full energy peak (FEP) efficiency measurement since the spectrum cannot be decomposed into well-defined components belonging to gamma rays with distinct energies [Korun (2004)]. For this purpose only single gamma ray emitters can be used in the case of detectors insensitive to X-rays. Therefore total efficiency calibration over the entire energy range needs numerous monoenergetic standards which make the process very cumbersome and time consuming. Availability of monoenergetic sources over wide energy range is also a constraint. Moreover, these sources are not very long lived, so they need to be replaced periodically. The other method reported in literature to get peak and total efficiency is to simulate the gamma ray spectra at each energy and for each geometry by using Monte Carlo Methods [Haase (1993a), Haase(1993b), Wang (2002), Dias(2002), García-Toraño (2005), Decombaz et al. (1992), Sima and Arnold (1995)]. This method requires the accurate knowledge of

internal as well as external components of the detector geometry such as crystal radius, crystal length, dead layer thickness, inner hole radius, Al end cap thickness and its distance from the crystal surface. This method can be used only if the efficiencies computed from Monte Carlo method matches with the experimental efficiencies.

6.3 Objective of the Work

The aim of the work was to obtain coincidence correction factors (k_{TCS}) of ^{152}Eu , ^{133}Ba , ^{134}Cs and ^{60}Co for point source geometry by using the analytical approach. The FEP and total efficiencies required for analytical calculation have been calculated by using the Monte Carlo code. The simulations were carried out using the optimized HPGe detector geometry given in Chapter 5 of this thesis. The method was validated by comparing the correction factors computed by this method with the correction factors obtained experimentally. The method was also applied to get the coincidence correction factors of long lived nuclides like ^{106}Ru , ^{125}Sb , ^{134}Cs and ^{144}Ce present in a fission product sample obtained from plutonium reprocessing plant. The optimized method has also been used for getting coincidence correction factors for volumetric samples.

6.4 Gamma Spectrometric Measurements

6.4.1 Standardization of Gamma Sources

The point sources of ^{60}Co and ^{134}Cs , were prepared from 1 ml solutions of these radioisotopes obtained from Board of Radiation and Isotope Technology, Mumbai, India. These sources were then standardized by counting standard ^{152}Eu and ^{133}Ba point sources along with these sources at a distance of 21.7 cm. Such a large sample-to-detector

distance was chosen so as to ensure negligible coincidence summing in the gamma rays of standard sources. The Eu-Ba efficiencies were fitted into a fourth order log-log polynomial curve by non-linear least square fitting and the disintegration rates of the other point sources were obtained by interpolating the efficiencies from this calibration curve. Similarly, 5 ml liquid sources of ^{134}Cs and ^{60}Co , were standardized using 5 ml standards of ^{152}Eu and ^{133}Ba at $d = 10.3$ cm. In this study, the detector used was the one whose geometry has been optimized in the previous work (given in Chapter 5). It is a closed end co-axial p-type DSG HPGe detector with a 20% relative efficiency and a resolution of 2.1 keV at 1332 keV.

6.4.2 Efficiencies of Point Sources at Different Distances

These standardized point sources along with the standard ^{109}Cd , ^{57}Co , ^{203}Hg , ^{137}Cs and ^{65}Zn sources were counted at different sample-to-detector distances, $d = 1.7, 6.5$ and 12.6 cm. The efficiencies at these distances were obtained by using the experimentally determined disintegration rates using the equation:

$$\varepsilon_{\gamma} = \frac{cps}{I_{\gamma} x dps} \quad (6.13)$$

where cps is the count rate at the energy of interest and I_{γ} is the gamma ray emission probabilities taken from Table of Isotopes [Firestone (1996)]. The efficiency curves at the three sample-to-detector distances, $d = 12.6, 6.5$ and 1.7 cm have been shown in figure 6.4(a-c) respectively. The efficiencies determined from non-coincident sources like ^{137}Cs , ^{109}Cd , ^{57}Co , ^{203}Hg , ^{51}Cr , ^{65}Zn have been fitted to a fourth order log-log polynomial at all

the three distances to obtain efficiency curve which is free of coincidence summing and has been shown as solid lines in figure 6.4(a-c).

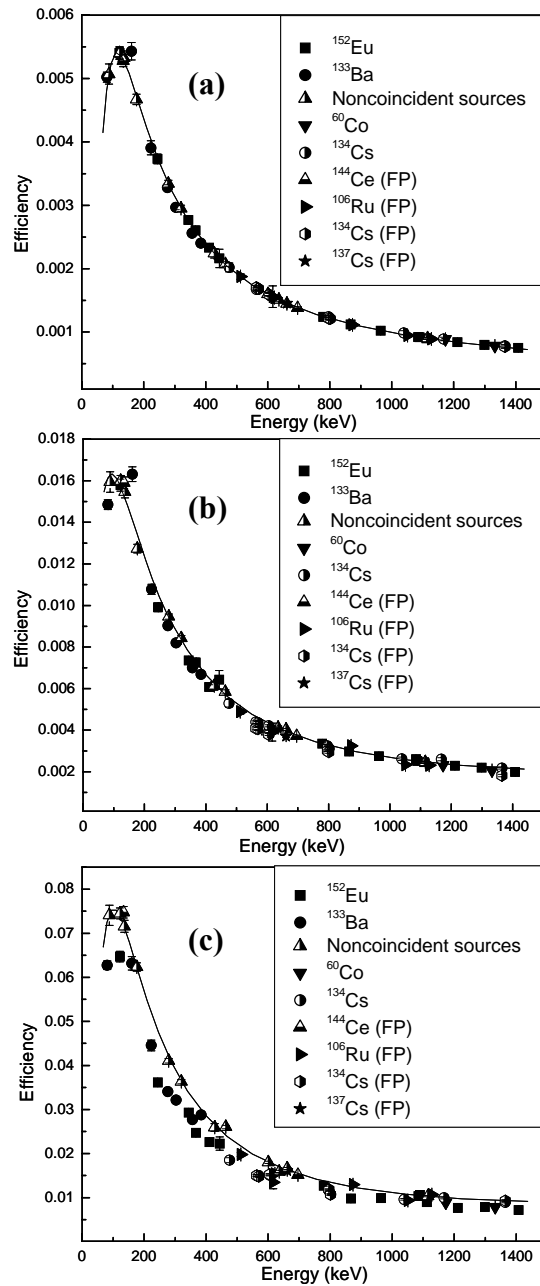


Figure 6.4 Full energy peak (FEP) efficiencies as a function of gamma ray energy for point source geometry at sample-to-detector distances, $d =$ (a) 12.6 cm, (b) 6.5 cm and (c) 1.7 cm. The solid line corresponds to the fourth order log-log fitting of efficiencies of monoenergetic sources. The nuclides marked with FP in the figure shows the nuclides present in the fission product sample.

As seen from the Figure 6.4, at $d = 12.6$ cm and 6.5 cm, the efficiencies obtained from the multi-gamma sources lie on the fitted curves. This shows that in this case even at $d = 6.5$ cm, the coincidence summing corrections are negligible for point source geometry. However, the efficiencies obtained from these multi-gamma ray sources at $d = 1.7$ cm, do not lie on the fitted efficiency curve drawn using monoenergetic sources. This indicates the effect of true coincidence summing at this distance and shows the need to obtain these correction factors when quantitative estimation of these radionuclides are required.

6.5 Coincidence Summing Correction for Point Source Geometry

6.5.1 Coincidence Summing Correction Factors by Analytical Method

The coincidence correction factors for the different gamma rays of ^{152}Eu , ^{133}Ba , ^{134}Cs and ^{60}Co were calculated at $d = 1.7$ cm using the analytical approach as discussed above. In order to calculate k_{TCS} by this method, the probability p_i was calculated by taking into account appropriate parameters obtained from the published decay schemes of these radionuclides [Firestone (1996)]. These decay schemes along with the numerical expressions used for calculation of coincidence correction factors are given in the Appendix III of this thesis. The internal conversion coefficient data were taken from Be et al. (2006). The peak (ϵ_i) and total efficiencies (ϵ_{ti}) required by this method have been obtained by performing Monte Carlo simulations for point source geometry. For this, the *F8* tally of the version MCNP4c has been used. Mode *P* was used. The simulations were done with the optimized detector geometry as given in detail in the Chapter 5 of this thesis, so as to remove any bias between the experimental and MCNP efficiencies. For getting total efficiencies, separate MCNP runs were performed for all the energies in

coincidence with the gamma ray peak of interest. In each run $\sim 10^8$ particles were sampled to reduce statistical uncertainties. The p_i , ε_i , ε_{ii} were then used in equation 6.2 to get the coincidence correction factors at different energies. The values of correction factors calculated at $d = 1.7$ cm for point source geometry have been given in the third column of Table 6.1.

6.5.2 Validation of the Analytical Method

The analytical method was also verified by other method. Since MCNP is decay scheme independent, the efficiency computed from MCNP for a monoenergetic source is free of any coincidence summing whereas as shown in Figure 6.4, the efficiencies determined experimentally are affected by coincidence summing effects. The true coincidence summing correction factor as defined in equation 6.1 can be expressed as the ratio of MCNP efficiency to the experimental efficiency:

$$k_{TCS} = \frac{\text{MCNP efficiency}}{\text{Experimental efficiency}} \quad (6.14)$$

The values of these experimental correction factors and their ratios with the correction factors computed by analytical method are given in Table 6.1. It can be seen that for all the nuclides, the factors from both the methods are matching within 1-5%. This validates the analytical approach. Figure 6.5 shows the plot of efficiencies corrected for the true coincidence summing correction factor obtained by the analytical method as a function of energy at $d = 1.7$ cm. Here, practically all the points which were lying below the efficiency curve before correction, are lying on the curve after correction giving rise to a good efficiency curve after correction.

Table 6.1 Coincidence correction factors for different nuclides at $d = 1.7$ cm by the analytical and experimental method for point source geometry.

Nuclide	E_γ (keV)	Coincidence correction factor		Ratio	% Error on experimental method
		Analytical method	Experimental method		
^{60}Co	1173	1.13	1.10	0.98	1.24
	1332	1.13	1.10	0.98	1.31
^{133}Ba	81	1.17	1.19	0.98	1.54
	160.6	1.08	1.15	0.94	1.48
	223.1	1.15	1.09	1.06	1.52
	276.4	1.15	1.17	0.98	1.53
	302.9	1.11	1.11	1.00	1.50
	356	1.09	1.09	0.99	1.48
	383.9	0.99	0.99	1.00	1.41
^{134}Cs	475.4	1.26	1.27	1.00	3.00
	563.2	1.30	1.28	0.99	1.32
	569.3	1.30	1.28	0.99	1.37
	604.7	1.17	1.21	1.04	1.21
	795.8	1.16	1.19	1.03	1.31
	801.9	1.26	1.29	1.02	1.34
	1038.6	1.08	1.14	1.06	1.82
	1167.4	0.97	0.99	1.01	1.99
	1365.1	0.91	0.96	1.05	1.95
^{152}Eu	121.8	1.15	1.18	1.02	1.84
	244.3	1.22	1.27	1.05	2.05
	344	1.09	1.12	1.02	1.33
	367	1.29	1.24	0.97	2.05
	411	1.21	1.22	1.00	1.55
	444	1.19	1.13	0.95	6.78
	778.9	1.12	1.10	0.98	1.36
	867	1.20	1.28	1.07	2.43
	964	1.08	1.14	1.05	1.82
	1085	0.97	0.99	1.02	1.94
	1089	1.11	0.96	0.87	1.91
	1112	1.05	1.12	1.06	1.87
	1212	1.19	1.20	1.01	2.02
1299	1.06	1.12	1.06	2.05	
1408	1.06	1.15	1.08	1.46	

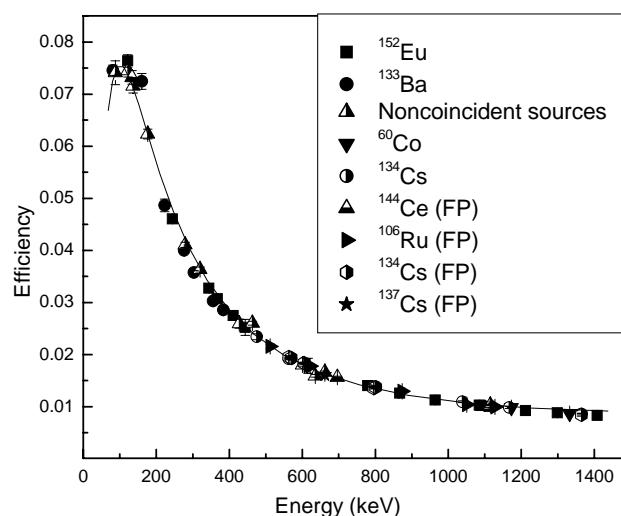


Figure 6.5 Corrected Efficiencies as a function of gamma ray energy for point source geometry at $d = 1.7$ cm. The solid line corresponds to the fourth order log-log fitting of efficiencies of monoenergetic sources.

6.5.1 Application of the Method

A fission product sample in point source geometry was counted at $d = 1.7$ cm to get the activity of different fission products such as ^{106}Ru , ^{125}Sb , ^{134}Cs and ^{144}Ce present in the sample. The fission product spectrum is shown in Figure 6.6. Since these radionuclides have gamma rays in cascade and at $d = 1.7$ cm, the true coincidence summing can be appreciable, therefore TCS correction factors were obtained for these nuclides by both the analytical and experimental method. These factors and their ratios are given in Table 6.2 and are found to match reasonably well. ^{137}Cs was also present in the fission product sample and as expected, its correction factor has been found to be close to unity. It can be seen that there are practically no coincidence corrections for ^{125}Sb and ^{144}Ce . Since ^{125}Sb is a multi-gamma ray source, this is a very good candidate for efficiency calibration. ^{144}Ce can also add to a point in efficiency curve in the low energy region which is very

sensitive to the quality of fitting. The uncorrected and corrected efficiencies at gamma ray energies of these radionuclides are also shown in Figure 6.4 and 6.5 respectively. The corrected efficiencies at the gamma energies of ^{106}Ru , ^{134}Cs are found to lie on the fitted curve of monoenergetic sources.

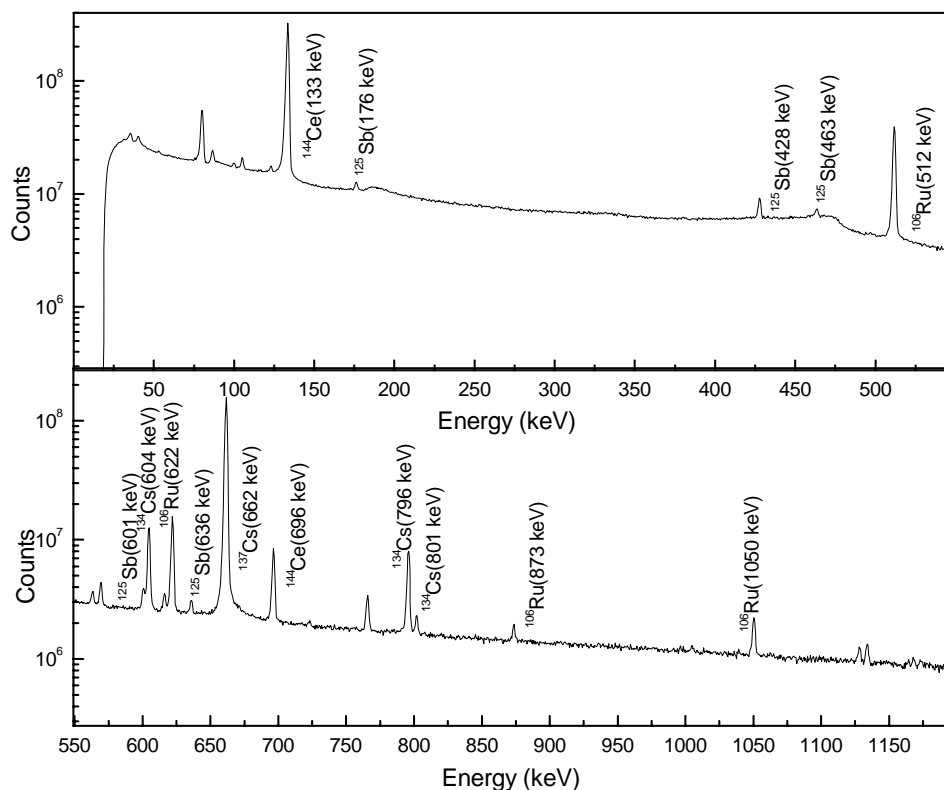


Figure 6.6 The gamma ray spectra of a fission product sample.

6.6 Coincidence summing correction for volumetric sources

Similarly, coincidence correction factors were obtained by both the methods for 5 ml sources of ^{152}Eu , ^{133}Ba , ^{134}Cs , ^{60}Co , ^{22}Na , ^{137}Cs , ^{109}Cd , ^{57}Co , ^{203}Hg , ^{65}Zn and for nuclides present in fission product solution. For this, these samples were counted at $d = 10.3$, 6.8 , 4.4 , and 2.0 cm respectively and the FEP efficiencies at these distances were obtained by

using the determined disintegration rates of these sources. The FEP efficiency values of all the sources at $d = 10.3, 6.8, 4.4$ and 2.0 cm are plotted in Figure 6.7(a-d) respectively. The efficiencies from monoenergetic sources were fitted to a fourth order log – log polynomial. The coincidence correction factors by analytical method were also obtained. Here also, peak and total efficiencies required for the analytical method were calculated by MCNP using the optimized detector geometry. As seen from Figure 6.7, for 5 ml sources, even at $d = 4.4$ cm, the efficiencies obtained from the multi-gamma sources lie on the fitted curves. This shows that even at $d = 4.4$ cm, the coincidence summing corrections are negligible for 5 ml geometry. However, the coincidence summing effect is more clearly seen at $d = 2.0$ cm where the efficiencies are not lying on the noncoincident efficiency curve. This indicates the effect of true coincidence summing at this distance and shows the need to obtain these correction factors. Table 6.3 and 6.4 lists the coincidence correction factors obtained for the 5 ml mononuclide and fission product sources by both the methods. The present method values are found to match within 1-5% with the analytical method values. Figure 6.8 gives the FEP efficiencies corrected for TCS obtained by the present method at $d = 2.0$ cm. All the points corresponding to multi-energetic sources after correction lie on the FEP efficiency curve from monoenergetic sources showing the validity of correction method for point and volumetric sources as well.

Table 6.2 Coincidence correction factors for nuclides present in fission product sample at $d = 1.7$ cm for point source geometry.

Nuclide	E_γ (keV)	Coincidence correction factor		Ratio	% Error on experimental method
		Analytical method	Experimental method		
^{137}Cs	661.6	1.00	1.02	0.98	1.21
^{144}Ce	133.5	1.00	0.98	1.02	1.75
^{125}Sb	176.3	1.01	0.98	1.03	1.51
	427.9	1.00	1.02	0.99	3.28
	463.4	1.00	0.92	1.08	1.40
	600.6	1.00	1.02	0.98	1.40
	635.9	1.00	1.09	0.91	1.71
^{106}Ru	511.9	1.08	1.09	0.99	2.27
	616.2	1.20	1.32	0.90	10.91
	621.9	1.14	1.15	0.98	1.71
	1050.3	1.13	1.11	1.02	2.03
	1128	0.99	0.93	1.06	2.37
^{134}Cs	563.2	1.30	1.30	1.00	1.56
	569.3	1.30	1.30	0.99	1.50
	604.7	1.17	1.20	0.97	1.24
	795.8	1.16	1.14	1.01	1.34
	801.9	1.26	1.28	0.99	1.66
	1365.1	0.91	0.91	1.00	2.63

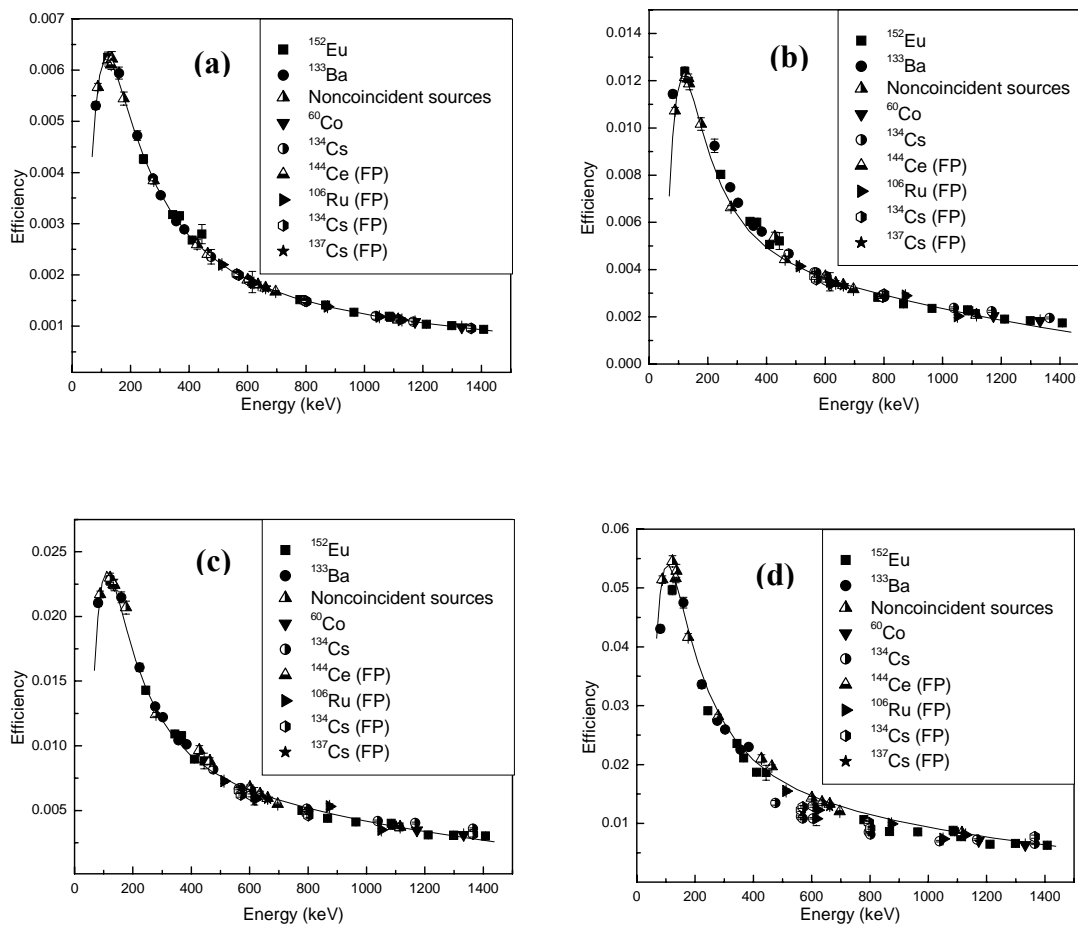


Figure 6.7 Efficiencies as a function of gamma ray energy for point source geometry at sample-to-detector distances, $d =$ (a) 10.3 cm, (b) 6.8 cm, (c) 4.4 cm and (d) 2.0 cm. The solid line corresponds to the fourth order log-log fitting of efficiencies of monoenergetic sources. The nuclides marked with FP in the figure shows the nuclides present in the fission product sample.

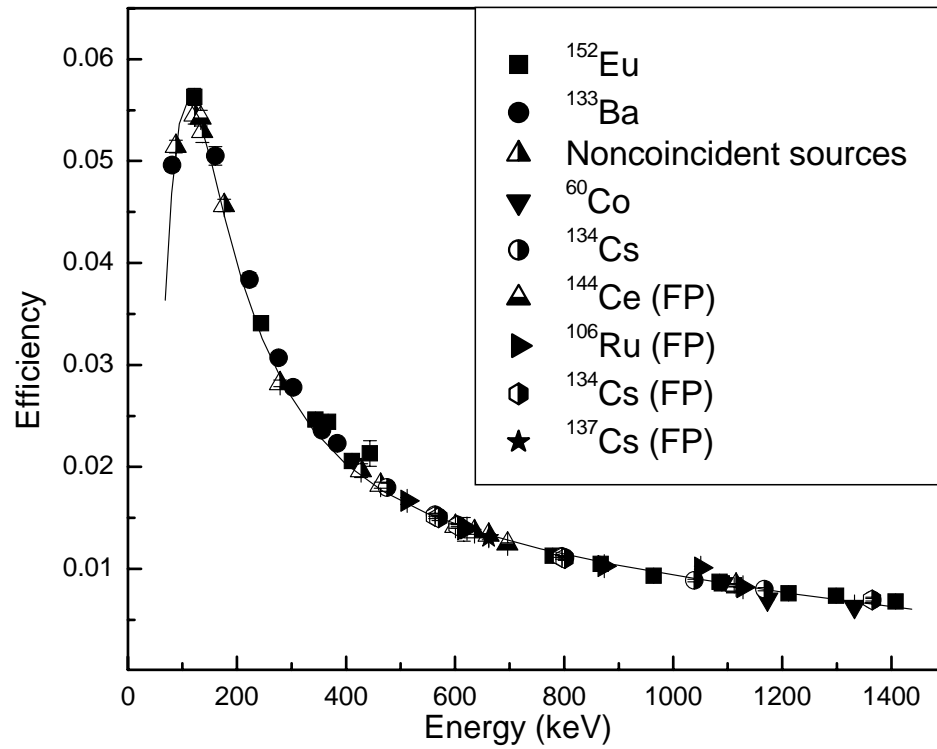


Figure 6.8 Corrected efficiencies as a function of gamma ray energy for 5 ml geometry at sample-to-detector distances, $d = 2.0$ cm. The solid line corresponds to the fourth order log-log fitting of efficiencies of monoenergetic sources. The nuclides marked with FP in the figure shows the nuclides present in the fission product sample.

Table 6.3 Coincidence correction factors for different nuclides at $d = 2.0$ cm by the analytical and experimental method for 5 ml source geometry.

Nuclide	E_γ (keV)	Coincidence correction factor		Ratio	% Error on present method
		Analytical method	Experimental method		
^{60}Co	1173	1.11	1.13	1.02	1.25
	1332	1.11	1.13	1.02	1.32
^{152}Eu	121.8	1.13	1.13	1.00	1.63
	244.3	1.18	1.17	0.99	2.02
	344	1.08	1.05	0.97	1.30
	444	1.16	1.14	0.99	6.79
	778.9	1.11	1.06	0.96	1.30
	867	1.17	1.22	1.04	2.45
	964	1.07	1.09	1.02	1.79
	1085	0.98	0.99	1.01	1.95
	1089	1.10	1.00	0.91	2.14
	1112	1.04	1.08	1.04	1.88
	1212	1.16	1.18	1.02	2.40
	1408	1.05	1.08	1.03	1.55
^{133}Ba	81	1.11	1.15	1.04	1.38
	160.6	1.01	1.06	1.06	1.89
	223.1	1.02	1.14	1.12	1.93
	276.4	1.06	1.12	1.06	1.18
	302.9	1.03	1.07	1.04	1.15
	356	1.02	1.05	1.02	1.13
	383.9	0.95	0.97	1.02	1.18
^{134}Cs	475.4	1.22	1.11	0.91	2.99
	563.2	1.25	1.17	0.94	1.26
	569.3	1.25	1.14	0.91	1.30
	604.7	1.14	1.08	0.94	1.13
	795.8	1.13	1.09	0.96	1.20
	801.9	1.22	1.13	0.93	1.24
	1038.6	1.06	1.05	0.98	1.83
	1167.4	0.97	0.92	0.94	2.01
	1365.1	0.92	0.87	0.95	2.00

Table 6.4 Coincidence correction factors for nuclides present in fission product sample at $d = 2.0$ cm for 5 ml geometry.

Nuclide	E_{γ} (keV)	Coincidence correction factor		Ratio	% Error on present method
		Analytical method	Experimental method		
^{137}Cs	661.6	1.00	1.01	1.01	1.03
^{144}Ce	133.5	1.00	1.01	0.99	1.49
^{125}Sb	176.3	1.01	1.10	1.09	1.44
	427.9	1.00	0.94	0.93	3.28
	463.4	1.00	0.93	0.93	1.49
	600.6	1.00	0.99	0.99	1.45
	635.9	1.00	1.00	1.00	1.80
^{106}Ru	511.9	1.07	1.08	1.01	2.24
	616.2	1.17	1.29	1.11	10.92
	621.9	1.12	1.15	1.03	1.66
	1050.3	1.11	1.38	1.25	2.05
	1128	0.99	1.03	1.03	2.55
	1562	0.81	0.86	1.07	3.53
^{134}Cs	563.2	1.25	1.24	0.99	2.06
	569.3	1.25	1.17	0.94	1.97
	604.7	1.14	1.1	0.96	1.58
	795.8	1.13	1.1	0.97	1.67
	801.9	1.22	1.2	0.98	2.11
	1365.1	0.92	0.9	0.98	3.53

6.7 Conclusion

Coincidence summing becomes very important at closer sample-to-detector geometry. Correction factors as high as 30% have been observed. MCNP calculated FEP and total efficiencies with optimized detector geometry can be effectively used to obtain coincidence correction factors using the analytical approach.

Summary and Conclusions

Passive nondestructive assay techniques based on gamma ray spectrometry rely on the measurement of spontaneous emissions from the nuclide monitored. The energy of the gamma ray characterizes the nuclide present and the count rate at the gamma ray monitored is related to the amount of the radionuclide. These techniques play very important role at different steps of the nuclear fuel cycle. These techniques are used for process control, nuclear materials accounting and safeguards. The reason for the wide range of applications of NDA techniques is their versatility with respect to the physical and chemical characteristics of the sample. These techniques are most useful for heterogeneous samples when it is difficult to get a representative sample for analysis such as waste packets and scraps. It is also important when sampling is not desired at all like for sealed containers and finished products. These techniques are particularly preferred when prior knowledge about the sample composition is not available [Carchon et al. (2000)]. The samples encountered in NDA are of diverse nature, in terms of size, shape and composition. Due to this, non-proportionality between the measured count rate and the nuclide amount may exist. In such a case, the measured count rate has to be multiplied by a number of correction factors (equation 1.7) such as attenuation correction factor, coincidence summing correction factor and correction factor related to the electronic losses to get correct results.

In this thesis work, procedures for obtaining the attenuation and true coincidence summing correction factors have been developed. Attenuation correction procedures have been developed for samples with both standard and nonstandard geometries. The coincidence correction approach has been applied for both point and extended source geometry. Major achievements and conclusions of this work pertaining to the

development of these correction procedures in gamma ray based NDA of nuclear materials have been summarized as follows.

For homogenous samples with standard geometry (i.e. where standards are available and getting efficiency for the concerned source-detector geometry is not a problem), a Hybrid Monte Carlo method has been developed to compute attenuation correction factors. This method involves generation of uniform random points within the sample volume and on the detector surface. The line connecting these two points reflects the path followed by the gamma ray to reach the detector. The attenuation correction factor is then obtained by calculating the distance traveled by the gamma ray in the sample and to reach the detector surface. This is done analytically by solving the intersection of the line connecting the points and the sample surface. Since this technique involves both random number generation which is a part of Monte Carlo method combined with the analytical approach, therefore this method is named as Hybrid Monte Carlo method. This method has been developed for some of the common sample geometries such as cylinder, disc, sphere and box. The attenuation correction factors have been obtained for a wide range of transmittances and sample-to-detector distances. The approach has been validated theoretically as well as experimentally. For theoretical validation, the attenuation correction factors have been calculated using the MCNP code. The results from both the methods were found to be reasonably matching, thereby validating the approach for all the sample geometries and at all sample-to-detector distances. The results were also compared with the attenuation correction factors for far-field and near-field expressions available in literature for these geometries. The results of our calculation had an excellent agreement with the far-field expression at far distance. The near-field expressions

although expected to be valid at close sample-detector geometries were not found to work at very close sample-detector distances. The HMC approach was validated by determining the correction factors experimentally. This was done for cylinder, disc and box-shaped sample. The attenuation correction factors from HMC method were found to match quite well with the experimental k_{att} at all sample-to-detector distances and for all the sample shapes. This establishes the validation of Hybrid Monte Carlo approach for varied sample geometries. The HMC approach has been found to be very simple and is free of any assumptions regarding sample-to-detector distances. The approach is common to all the geometries and is easily extendable to any sample shape.

The samples encountered in the nondestructive assay of nuclear materials can often be of nonstandard shape and size. For these samples, the standards are not generally available so that the efficiencies are not known for the required sample-detector geometry. A semi-empirical approach [Venkataraman and Croft (2003)] is available in literature known as apparent mass method for samples of nonstandard geometry. This method is used to obtain the amount of the nuclide monitored and corrects for the self-attenuation taking place in the sample in a self-consistent way making use of the multi-gamma rays emitted by the nuclide monitored. This method makes use of the fact that the attenuation of the gamma rays decreases with the increase in gamma ray energies. So that when the apparent mass i.e. the mass of the nuclide obtained by correcting the measured count rate with the gamma ray intensities, efficiencies and the specific activity of the nuclide monitored is plotted as a function of inverse of gamma ray energy, a straight line is obtained with a finite slope indicating the effect of attenuation in the sample. Extrapolation of apparent mass to infinite photon energy gives actual mass of the sample

(zero photon attenuation condition). This method has been standardized for samples with uranium and plutonium as the analyte. This has been done using a series of uranyl nitrate samples and plutonium packets. It has been observed that for uranyl nitrate solutions, in all the cases, the uranium mass is overestimated and the exponent of E has to be modified from 1 to 1.35 to get results within 4-5% with no systematic bias whereas for PuO_2 samples the exponent of E is 1 as suggested by the Venkataraman and Croft (2003). These different exponents for uranium and plutonium can be explained based on the energy range monitored. This method has also been applied to real samples eg. stainless steel samples, sludge and enriched uranium.

FEP efficiency calibration of a gamma ray detector needs a set of monoenergetic gamma ray standards eg. ^{241}Am , ^{109}Cd , ^{57}Co , ^{203}Hg , ^{51}Cr , ^{137}Cs , ^{65}Zn or by using standard multi-gamma ray sources like ^{152}Eu , ^{133}Ba . The use of former is limited by its availability and frequent replacement and the latter is restricted by coincidence summing effects at closer sample-detector geometry. Monte Carlo simulation can be used to get FEP efficiencies at different energies. The advantage of this method is that it can be applied to a variety of sample shapes and sizes. But often there is inaccuracy in the detector dimensions provided by the manufacturer leading to mismatch in the MCNP and experimental efficiencies. In our case also, the MCNP code has been used for FEP efficiency calibration of HPGe detector. The MCNP efficiencies were found to be higher than experimental efficiencies. The detector geometry was optimized by systematically changing the detector geometry parameters eg. detector crystal radius, its length, inner hole radius, dead layer thickness and Al end cap to crystal distance. After optimization, for point source geometry, the MCNP and the experimental efficiency values were found

to be within 5% over the entire energy range. The optimized geometry was then checked by computing the MCNP efficiencies for extended geometries such as 5 ml and 100 ml cylindrical samples and comparing it with the corresponding experimental efficiencies. In this case also, the results are found to be within 5%.

As emphasized above, at close sample-detector distances, the results obtained in the case of gamma spectrometric measurements using multi-energetic sources, may be severely biased due to coincidence summing effects. This effect was observed in the experimental efficiencies obtained at different sample-to-detector distances. At the closest distance ($d = 1.7$ cm), the efficiencies from multi-energetic sources (^{152}Eu , ^{133}Ba , ^{134}Cs , ^{60}Co and ^{106}Ru) are found to be significantly deviated from the efficiencies obtained from monoenergetic sources (^{137}Cs , ^{109}Cd , ^{57}Co , ^{203}Hg , ^{51}Cr , ^{65}Zn). This is due to coincidence summing of gamma rays in cascade. It has been observed that if the sample-to-detector distance is greater than 5 cm, the coincidence summing corrections becomes negligible. The analytical approach [Andreev et al. (1972)] has been used to obtain coincidence summing correction factors at $d = 1.7$ cm. This method needs the probability of simultaneous emission of two or more gamma rays and total efficiencies at different gamma ray energies. The former is obtained by making use of the decay scheme and various nuclear decay parameters such as energies of gamma transitions, gamma ray emission probabilities, K-capture probabilities (in electron capture decay), mean energy of K X-rays, fluorescence yield, total and K conversion coefficients etc. The total efficiencies required by this method were computed using MCNP code. For computation, the optimized geometry of the detector has been used. Coincidence correction factors as high as 30% have been obtained. These correction factors have been validated by comparing

these correction factors with the experimentally obtained correction factors. Also, the efficiencies of the multi-energetic sources at $d = 1.7$ cm after applying coincidence summing corrections, are found to lie on the efficiency curve drawn using monoenergetic sources. Coincidence summing correction factors have also been computed for extended sources and were found to match with the experimental correction factors. These corrections become important for low level samples where sample has to be counted as close as possible to the detector. These corrections also become important in the case of well-type detectors where the samples are kept in the well of the detector and efficiency of the gamma rays reaching the detector is very high.

From the studies, it can also be concluded that the Monte Carlo simulations are very important in nondestructive assay of nuclear materials. It can be used to simulate a variety of sample-detector geometries. It can also be used to optimize the design of a nondestructive assay system before actually setting up the system. These simulations are very useful for verification of any experimental data or any method by simulating the basic facts involved in the experiment. They can be successfully applied to obtain robust estimates of the correction factors which should be applied to the efficiency in order to account for differences between the calibration measurement and the actual measurement.

Future Scope of the Work

In future, there is a scope to extend the hybrid Monte Carlo approach to obtain attenuation correction factors for large samples such as waste drums which are generally

collimated. Also, since in nondestructive assay of nuclear materials, the samples can be high count rate also, the effect of rate related losses can be further explored.

BIBLIOGRAPHY

A

Aguiar, J. C., Galiano, E. and Fernandez, J., *Applied Radiation and Isotopes* 64 (2006) 1643.

Aguiar, J. C., *Applied Radiation and Isotopes* 66 (2008) 1123.

Andreev, D.S., Erokhina, K.I., Zvonov, V.S. and Lemberg, I.Kh., *Instrum. Exp. Technol.* 15 (1972) 1358 (English translation).

Andreev, D.S., Erokhina, K.I., Zvonov, V.S. and Lemberg, I.Kh., *Izv. Akad Nauk, SSSR Ser. Fiz.*, 37 (1973) 1609.

Auguston, R. and Reilly, T.D., Los Alamos Scientific Laboratory, LA-5651-M (1974).

B

Bäcklin, A., Hakansson, A., Björkholm, P., Dyring, A. and Görsten K-G., Proceedings of the 13th ESARDA Symposium, Avignon, France (1991).

Badawy, I., Youssef, A.S., El-Kazzaz, S.H. and El-Gammal, W.A., *Nuclear Instruments and Methods in Physics Research A* 453 (2000) 621.

Baker, C.A., Batty, C.J. and Sakamoto, S., *Nuclear Instruments and Methods in Physics Research A* 259 (1987) 501.

Baumung, K., Bohnel, K., Klunker, J., Kuchle, M. and Wolff, J. Proceedings IAEA-Karlsruhe, Germany Symposium on Safeguards Techniques, 2 (1970) 177.

Be, M-M., et al., Monographie BIPM-5, Vol 1-4 (2006).

Berndt, R., *Kernenergie* 31 (1988) 58.

Binquan, Z., Jizeng, M.A., Jianping, C., Liye, L. and Yong, M., *Nuclear Electronics & Detection Technology* 25 (2005) 274 (in Chinese).

Black, W.W., *Nuclear Instruments and Methods* 71 (1969) 317.

Bochud, F., Bailat, C.J., Buchillier, T., Byrde, F., Schmid, E. and Laedermann, J.P., *Nuclear Instruments and Methods in Physics Research A* 569 (2006) 790.

Boson, J., Agren, G. and Johansson, L., *Nuclear Instruments and Methods in Physics Research A* 587 (2008) 304.

Briesmeister, J.F., MCNP – a general Monte Carlo N-particle transport code version 4C LA-13709-M, Los Alamos National Laboratory, USA (2000).

Bronson, F.L. and Wang, L., Waste Management '96, Tucson, AZ, USA (1996).

Budja's, D., Heisel, M., Maneschg, W. and Simgen, H., *Applied Radiation and Isotopes* 67 (2009) 706.

Bullock, R.J. and Large, N.R., Report AERE-R-6748, Atomic Energy Research Establishment, Harwell, UK (1971).

C

Carchon, R., Bruggeman, M. and Majkowski, I., *Applied Radiation and Isotopes* 53 (2000) 317.

Chard, P.M.J., Croft, S., Cruzate, J., Guardini, S., Hutchinson, I.G., Lamarche, A., Lebrun, A., Lee, Y.K., Maffra, O., Moshayev, A., Parker, D., Peerani, P., Rackham J., Thaurel, B., Laure – Weber, A. and Wright, G., *Esarda Bulletin*, 33 (2006) 26.

Chilton, A.B., Shultis, J.K. and Faw, R.E., Principles of Radiation Shielding, Prentice-Hall, Inc., New Jersey (1984).

Cline, J.E., Proceedings of ANS Topical Conference at Mayaguez, Puerto Rico (1978).

Conelly, A. L. and Black, W.W., *Nuclear Instruments & Methods* 82 (1970) 141.

Corte, F. De and Freitas, M.C., *Journal of Radioanalytical and Nuclear Chemistry*, 160 (1992) 253.

Cox, M.G. and Manneback, P.E., *IMA J. Numer. Anal.* 5 (1985) 275.

Croft, S., *Nuclear Geophysics* 9 (1993) 425.

Croft, S., Curtis, D. and Wormald M., Proc. of 46th Annual Meeting of the INMM (Institute of Nuclear Materials Management'04) Phoenix, Arizona, USA, Paper 341 (2005).

Clapham, M., Farese, N., Jaime, R., Lezzoli, L. and Schillebeeckx, P., Proc. of the 19th ESARDA Symposium on Safeguards and Nuclear Material Management, Montpellier (F), 13-15 May (1997).

Cobb, D.D., Phillips, J.R., Bosler, G.E., Eccleston, G.W., Halbig, J.K., Hatcher, C.R. and Hsue, S-T. , Los Alamos National Report, LA- 9041, vol I (1982).

Crane, T.W. and Baker, M.P., NUREG/CR-5550, LA-UR-90-732, Chapter 13 (1991) 379.

Czirr, J.B., *Nuclear Instruments & Methods* 88 (1970) 321.

D

Debertin, K. and Helmer, R.G., Gamma- and X-ray Spectrometry with Semiconductor Detectors, Elsevier Science Publishers, New York (1988).

- Debertin, K. and Grosswendt, B., *Nuclear Instruments & Methods* 203 (1982) 343.
- Debertin, K. and Jianping, R.E.N., *Nuclear Instruments & Methods A*, 278 (1989) 541.
- Debertin, K. and Schotzig, U., *Nuclear Instruments & Methods* 158 (1979) 471.
- De Castro Faria, N.V. and Levesque, R.J.A., *Nuclear Instruments & Methods* 46 (1967) 325.
- Decombaz, M., Gostely, J-J. and Laedermann, J-P., *Nuclear Instruments & Methods A* 312 (1992) 152.
- Dias, M.S., Tadeka, M.N. and Koskinas, M. F., *Applied Radiation and Isotopes* 56 (2002) 105.
- Dickens, J.K., *Nuclear Instruments & Methods* 98 (1972) 451.
- Dixon, W.R., *Nucleonics* 8 (1951) 68.
- Dragnev, T., *Atomic Energy Review*, 11 (1973) 341.
- Dryak, P. and Kovar, P., *Journal of Radionalytical and Nuclear Chemistry*, 279 (2009) 385.
- Dryak, P. and Kovar, P., *Applied Radiation and Isotopes* 64 (2006) 1346.

E

- East, L.V., *Nuclear Instruments & Methods* 93 (1971) 193.
- Ensslin, N., Reilly, D., Smith Jr., H., and Kreiner, S., editors. Los Alamos National Laboratory 111 (1991) NUREG/CR-5550 LA-UR-90-732. [Available from: <http://www.lanl.gov/orgs/n/n1/panda/>.]
- Estep, R.J., Los Alamos National Laboratory, LA-UR-90-2054 (1990).
- Evans, L.G., Ph.D Thesis, The University of Birmingham (2009).

Ewa, I.O.B., Bodizs, D., Czifrus, Sz. and Molnar, Zs, *Applied Radiation and Isotopes* 55 (2001) 103.

F

Fehrenbacher, G., Meckbach, R. and Jacob, P., *Nuclear Instruments & Methods A* 383 (1996) 454.

Firestone, R.B., *Table of Isotopes*, Wiley-Interscience Publishing, Eighth Edition (1996).

Fisher, P. and Engle, L., *Physics Review*, 134 (1964) 810.

Forcinal, G., *Nuclear Instruments & Methods* 107 (1973) 125.

Francois, J.P., *Nuclear Instruments & Methods* 117 (1974) 153.

G

Garcia-Talavera, M., Laedermann, J.P., Decombaz, M., Daza, M.J. and Quintana, B., *Applied Radiation and Isotopes* 54 (2001) 769.

García-Talavera, M. and Peña, V., *Applied Radiation and Isotopes* 60 (2004) 227.

Garcia-Talavera, M., Neder, H., Daza, M.J. and Quintana, B., *Applied Radiation and Isotopes* 52 (2000) 777.

García-Toraño, E., Pozuelo, M. and Salvat, F., *Nuclear Instruments and Methods in Physics Research A* 544 (2005) 577.

Gunnink R. and Niday, J.B., USAEC Rept. UCRL- 51061 (vol. 1), Univ. of California, NTIS (1972).

Gilmore, G and Hemingway, J.D., Practical Gamma Ray Spectrometry, John Wiley & Sons, ISBN 0471 951 501 (1995).

Glouvas, A., Xanthos, S., Antonopoulos-Domis, M., Silva, J., *Health Physics* 74 (1998) 216.

Gmar, M. and Capdevila, J., *Nuclear Instruments and Methods in Physics Research A* 422 (1999) 841.

Gosnell, T.B., Hall, J.M., Ham, C.L., Knapp, D.A., Koenig, Z.M., Luke, S.J., Pohl, B.A., Schach von Wittenau, A. and Wolford, J.K., UCRLID-127436, Lawrence Livermore National Laboratory (1997).

Gozani, T., United States Regulatory Commission, NUREG/CR-0602 (1981).

Gray, P.W. and Ahmad, A., *Nuclear Instruments and Methods in Physics Research A* 237 (1985) 577.

Guardini, S., (Editor), ESARDA Bulletin 31 (2003).

H

Haase, G., Tait, D. and Wiechen, A., *Nuclear Instruments and Methods in Physics Research A* 329 (1993a) 483.

Haase, G., Tait, D. and Wiechen, A., *Nuclear Instruments and Methods in Physics Research A* 336 (1993b) 206.

Hakkila, E.A., Sonnier, C.S. and Case, R.S., LA-UR-93-1483, September (1993).

Hardy, J.C., Iacob, V.E., Sanchez-Vega, M., Effinger, R.T., Lipnik, P., Mayes, V.E., Willis, D.K. and Helmer, R.G., *Applied Radiation and Isotopes* 56 (2002) 65.

Helmer R.G., Hardy J.C, Iacob V.E., Sanchez-Vega M., Neilson R.G. and Nelson J., *Nuclear Instruments and Methods in Physics Research A* 511 (2003) 360.

Helmer, R.G. and Lee, M.A., *Nuclear Instruments and Methods* 178 (1980) 499.

Henry, C.N., Los Alamos Scientific Laboratory, LA-8870-PR (1981).

Hollas, C.L., Close D.A. and Moss, C.E. *Nuclear Instruments and Methods in Physics Research B* 24/25 (1987) 503.

Hsue, S.T., *Atomic Energy Review* 16 (1978) 89.

Hsue, S.T., Crane, T.W., Talbert, W.L. Jr. and Lee, J.C., Los Alamos Scientific Laboratory, LA-6923 (1978).

Hubbell, J.H., *Int. J. Applied Radiation and Isotopes*, 33 (1982) 1269. These coefficients can be accessed from: <http://physics.nist.gov/PhysRefData/XrayMassCoef/cover.ihtml>

Jackel, B., Westmeier, W. and Patzelt, P., *Nuclear Instruments and Methods in Physics Research A* 261 (1987) 543.

Huy, N.Q., Binh, D.Q. and An, V.X., *Nuclear Instruments and Methods in Physics Research A* 573 (2007) 384.

J

Johnston, P.N., Thesis, School of physical sciences, La Trobe University, Australia (1985).

Johnston P.N., Hult, M. and Gasparro, J., Cascade summing effects in close geometry gamma ray spectrometry. *Applied Radiation and Isotopes* 64 (2006) 1323.

K

- Kafala, S.I., *Journal of Radioanalytical and Nuclear Chemistry* 191 (1995) 105.
- Kamboj, S. and Kahn, B., *Health Physics* 70 (1996) 512.
- Kamboj, S. and Kahn, B., *Radiation Measurements* 37 (2003) 1.
- Karamanis, D., *Nuclear Instruments and Methods in Physics Research A* 505 (2003) 282.
- Kelly, T.M., Merrigan, J.A. and Lambrecht, R.M., *Nuclear Instruments and Methods* 109 (1973) 233.
- Keyser, R.M., *Nuclear Instruments and Methods in Physics Research B* 213 (2004) 236.
- Korun, M., *Applied Radiation and Isotopes* 60 (2004) 207.
- Korun, M., Likar, A. and Vidmar, T., *Nuclear Instruments and Methods in Physics Research A* 390 (1997) 203.
- Kouzes, R.T., Siciliano, E.R., Ely, J.H., Keller, P.E. and McConn, R.J., *Nuclear Instruments and Methods in Physics Research A* 584 (2008) 383.
- Knoll, G.F., Third Edition, ISBN 0-471-073385, John Wiley & Sons, New York (2000).
- Kull, L.A., Bramblett, R.L., Gozani, T. and Rundquist, D.E., *Nuclear Science and Engineering*, 39 (1970) 163.

L

- Laborie, J-M., Petit, G.L., Abt, D. and Girard, M., *Applied Radiation and Isotopes* 53 (2000) 57.
- Lauterjung, J., Will, G. and Hinze, E., *Nuclear Instruments and Methods in Physics Research A* 239 (1985) 281.

Lepy, M.C., et al., *Applied Radiation and Isotopes* 55 (2001) 493.

Liye, L., Jizeng, M.A., Binqun Z. and Yueru, J. International Radiation Physics Society Workshop on Frontier Research in Radiation Physics and Related Areas, Chengdu, China Paper collection, 204 (2004).

Ludington, M.A. and Helmer, R.G., *Nuclear Instruments and Methods in Physics Research A* 446 (2000) 506.

Lynch, F., *IEEE Transactions on Nuclear Science*, NS-22 (1975) 58.

Lyons, P. and Stevens, J., *Nuclear Instruments and Methods*. 114 (1974) 313.

M

Maenhaut, W. and Raemdonck, H., *Nuclear Instruments and Methods in Physics Research B* 1 (1984) 123.

Martz, H.E., Roberson, G.P., Robert-Coutant, C., Schneberk, D.J. and Camp, D.C., Proc. 14th Annual ESARDA Meeting, Salamanca, Spain, May 44 (1992) 273.

Mariani, A., Passard, C., Jallu, F. and Toubon H., *Nuclear Instruments and Methods in Physics Research B*, 211 (2003) 389.

Mariscotti, M.A, *Nuclear Instruments and Methods* 50 (1967) 309.

Mccallum, G.J. and Coote, G.E., *Nuclear Instruments and Methods* 130 (1975) 189.

McNelles, L.A., and Campbell, J.L., *Nuclear Instruments and Methods* 109 (1973) 241.

Meeks, A.M. and Chapman, J., Technical report, Oak Ridge National Laboratory (ORNL), ORNL/TM-13362 (1991).

Metropolis, N. and Ulam, S., *Journal of the American Statistical Association* 44 (1949) 335. [doi:10.2307/2280232](https://doi.org/10.2307/2280232). [PMID 18139350](https://pubmed.ncbi.nlm.nih.gov/18139350/).

Miller, T.G., *Nuclear Instruments and Methods* 63 **(1968)** 121.

Moens, L., De Donder, J., Xilei, Lin, De Corte, F., De Wispelaere, A., Simonits, A. and Hoste, J., *Nuclear Instruments and Methods* 187 **(1981)** 451.

Montgomery, D.M. and Montgomery, G.A., *Journal of Radioanalytical and Nuclear Chemistry, Articles*, 193 **(1995)** 71.

Moss, C., Goulding, C., Hollas C. and Myers, W., *IEEE Trans. Nucl. Sci.*, 51 **(2004)** 1677.

Mukhopadhaya, P.K., *Proceedings of Symposium on Intelligent Nuclear Instrumentation, Mumbai* **(2001)** 307.

N

Nakamura, T. and Suzuki, T., *Nuclear Instruments and Methods* 205 **(1983)** 211.

Nir-El, Y. and Sima, O., *Applied Radiation and Isotopes* 55 **(2001)** 1.

Normand, S., Mouanda, B., Haan S. and Louvel, M., *Nuclear Instruments and Methods in Physics Research A* 484 **(2002)** 342.

Norman, E., Prussin, S., Larimer, R., Shugart, H., Browne, E., Smith, A., McDonald, R.,

Nitsche, H., Gupta, P., Frank M. and Gosnell, T., *Nuclear Instruments and Methods in Physics Research A* 521 **(2004)** 608.

O

Owen, E. and Fage, W., *Proc. Phys. Soc., London*, 34 **(1921)** 27.

P

Parker, J.L., Los Alamos National Laboratory report, LA-10045, (1986).

Pérez-Moreno, J., San Miguel, E.J.P. and Bolívar, J.L., *Nuclear Instruments and Methods in Physics Research A* 491 (2002) 152.

Peerani, P. and Looman, M., Proceedings of the 24th ESARDA Annual Meeting, Luxembourg (2002) 131.

Pessara, W., *International Journal of Applied Radiation and Isotopes* 34 (1983) 519.

Press, W.H., Teukolsky, S.A., Vetterling, W.T. and Flannery, B.P., Numerical recipes in Fortran 77, Cambridge University Press (1996).

R

Reilly, D., Ensslin, N., Smith, Jr. H. and Kreiner, S. (Eds), United States Nuclear Regulatory Commission Report NUREG/CR-5550, LAUR-90-732 (1991).

Reus, U. and Westmeier, W., *At. Data Nucl. Data Tab.* 29 (1983).

Richardson, A.E. and Sallee, W.W., *Nuclear Instruments and Methods in Physics Research A* 299 (1990) 344.

Rodenas, J., Martinavarro, A. and Rius V., *Nuclear Instruments and Methods in Physics Research A* 450 (2000) 88.

Ródenas, J., Pascual, A., Zarza, I., Serradell, V., Ortiz, J. and Ballesteros, L., *Nuclear Instruments and Methods in Physics Research A* 496 (2003) 390.

Rogers, D.R., Handbook of Nuclear Safeguards Measurement Methods, United States Regulatory Commission, NUREG/CR-2078 (1983).

- Routti, J.T. and Prussin, S.G., *Nuclear Instruments and Methods* 72 **(1969)** 125.
- Russo, P.A., Siebelist, R., Painter, J.A. and Gilmer, J.E. Los Alamos National Laboratory report, LA-11729-MS **(1990)**.
- Russo, P.A. and Vo, D.T., Los Alamos National Laboratory report, LA-UR-05-3813 **(2005)**.

S

- Sanchez, F., Navarro, E., Ferrero, J.L., Moreno, A., Roldan, C., Baeza, A. and Paniagua, J., *Nuclear Instruments and Methods in Physics Research B* 61 **(1991)** 535.
- Sanchez-Reyes, A.F., Febrian, M.I., Baro, J. and Tejada, J., *Nuclear Instruments and Methods in Physics Research B* 28 **(1987)** 123.
- Sanyal, S., Pancholi, S. and Gupta, S. *Nuclear Instruments and Methods* 136 **(1976)** 157.
- Schima, F.J. and Hoppes, D.D., *International Journal of Applied Radiation and Isotopes* 34 **(1983)** 1109.
- Sheppard, G.A., Russo, P.A., Miller, M.C., Wenz, T.R., Piquette, E.C., Haas, F.X., Glick, J.B. and Garrett, A.G., Los Alamos National Laboratory report LA-UR-91-2507 **(1991)**.
- Shima, K., Umetani, K. and Mikomu, T., *Journal of Applied Physics* 51 **(1980)** 846.
- Sima, O. and Arnold, D., *Applied Radiation and Isotopes* 67 **(2009)** 701.
- Sima, O. and Arnold, D., *Applied Radiation and Isotopes* 47 **(1996)** 889.
- Sima, O., *Applied Radiation and Isotopes* 47 **(1996)** 919.
- Sima, O. and Arnold, D., International Conference on Low Level Measurement Techniques. ICRM 1995, Seville, 2-6 October **(1995)**.
- Sima, O. and Arnold, D., *Applied Radiation and Isotopes* 67 **(2009)** 701.

Simmonds, S.M., Sprinkle, Jr., J.K., Hsue, S.-T. and Kellogg, M.P., Los Alamos National Laboratory, Los Alamos, NM, LA-UR-90-2253 (1990).

Sinkko, K. and Aaltonen, H., Report STUK-B-VALO 40, Helsinki (1985).

Slavic, I.A. and Bingulac, S.P., *Nuclear Instruments and Methods* 84 (1970) 261.

Sprinkle, Jr., J.K., Cole, R., Collins, M.L., Hsue, S.-T., Russo, P.A., Siebelist, R., Smith, Jr., H.A., Ceo, R.N. and Smith, S.E., Los Alamos National laboratory report LA-UR-96-3482 (1996).

Sobol, I.M., A primer for the Monte Carlo method, CRC Press (1993).

Sundgren, O., *The Science of The Total Environment*, 130-131 (1993) 167.

T

Thirring, H., *Physik. Zeitschr.*, 13 (1912) 266.

Tripathi, R., Tomar, B.S., Reddy, A.V.R. and Manohar, S.B., BARC Internal report, BARC/ 2002/I/009, (2002).

Tzika, F., Stamatelatos, I.E., Kalef-Ezra, J. and Bode, P., *Nukleonika* 49 (2004) 115.

Tzika, F., Kontogeorgakos, D., Vasilopoulou, T. and Stamatelatos, I.E., *Applied Radiation and Isotopes* 68 (2010) 1441.

V

Van Riper, K.A., Metzger, R.L. and Kearfott, K.J., Proceedings of the Topical Meeting on Radiation Serving Society, Santa Fe, NM (2002).

Vargas, M.J., Timo' n, A.F., Di'az, N.C. and Sa'nchez, D.P. *Journal of Radioanalytical and Nuclear Chemistry* 253 (2002) 439.

Vidmar, T., et al., *Applied Radiation and Isotopes* 66 (2008) 764.

W

Wainio, K.M. and Knoll, G.F., *Nuclear Instruments and Methods* 44 (1966) 213.

Wang, T.F., Carlson, J.B., Koenig, Z.M., Ruhter, W.D., Lee, T.S.H. and Winn, J., *Nuclear Instruments and Methods in Physics Research A* 353 (1994) 678.

Wang, Z., Kahn, B. and Valentine, J.D., *IEEE Transactions on Nuclear Science* 49 (2002) 1925.

Tuttle, R.J., *Nuclear Science and Engineering*, 56 (1975) 37.

Vargas, M.J., Fernandez Timon, A., Cornejo Diaz, N. and Perez Sanchez, D., *Applied Radiation and Isotopes* 57 (2002) 893.

Venkataraman, R. and Croft, S., *Nuclear Instruments & Methods in Physics Research A* 505 (2003) 527.

Wang, Z., Kahn, B. and Valentine, J.D., *IEEE transactions on Nuclear Science* 49 (2002) 1925.

Weber, A-L., *Esarda Bulletin*, 35 (2006) 59.

Wells, G.M., Cookson, J.A., Metcalfe, B., Håkansson, Ane and Bäcklin, Anders, Hildingsson, Lars and Danielson, Nina, *Proceedings of the 13th Annual ESARDA Symposium on Safeguards and Nuclear Materials Management* (1991) 325.

Wenz, T.R., Russo, P.A., Miller, M.C., Menlove, H.O., Takahashi, T., Yamamoto Y. and Aioki, I., *Los Alamos National Laboratory report LA-UR-91-3323* (1991).

Willet, J.B., *Nuclear Instruments and Methods* 84 (1970) 157.

Winyard, R.A. and McBeth, G.W., *Nuclear Instruments and Methods in Physics Research A* 98 (1972) 525.

Woller, J., *The Basics of Monte Carlo Simulations*, University of Nebraska-Lincoln Physical Chemistry Lab, Spring (1996).

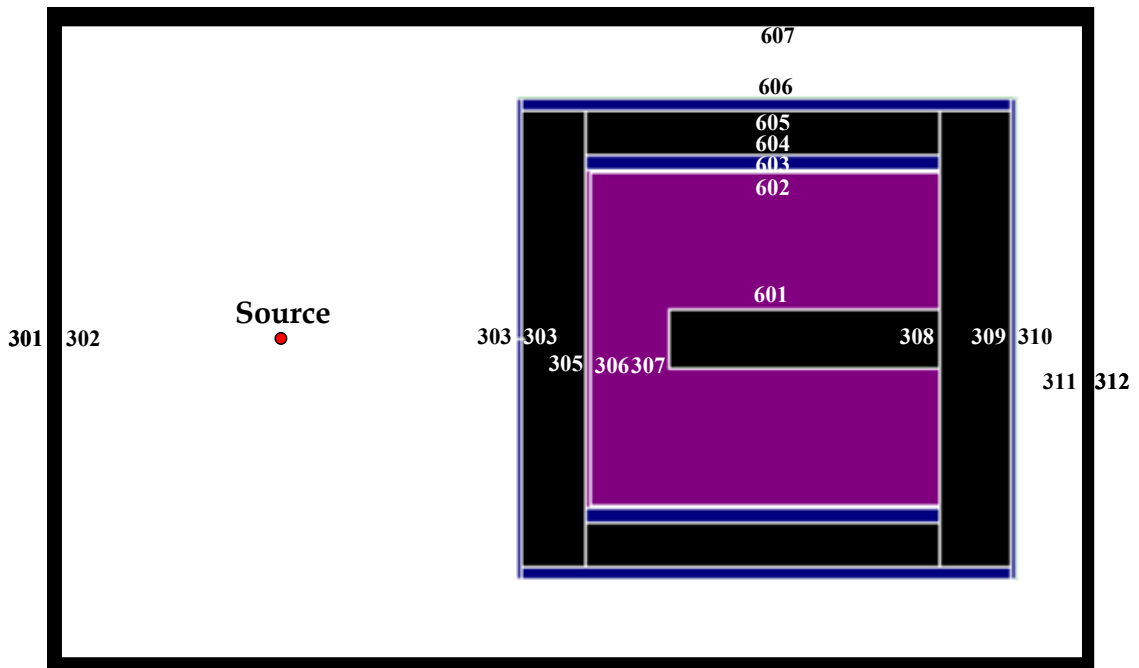
γ

Yalcin, S., Gurler, O., Kaynak, G. and Gundogdu, O., *Applied Radiation and Isotopes* 65 (2007) 1179.

APPENDIX I

A typical input file of MCNP

The input file given in this section corresponds to the HPGe detector geometry shown below:



The HPGe detector considered here is a closed end co-axial detector. The surface numbers corresponding to different planar and cylindrical surfaces of the detector system have been marked in the figure. The view shown in the figure is a view of the geometry from the XZ plane. A point source is placed at a distance of 5.0 cm and emits gamma rays in the range of 88-662 keV. The *F8* tally is used which gives information about the pulse height distribution of the source.

Input to calculate HPGe detector response over wide energy range

C	Cell cards			
1	0		306 -307 -601	imp:p=1 \$ Inner hole
2	1	-5.35	305 -307 -602 #1	imp:p=1 \$ Ge detector
3	1	-5.35	304 -307 -603 #1 #2	imp:p=1 \$ Dead layer
4	0		303 -304 -605	imp:p=1 \$ Front vacuum
5	0		304 -307 604 -605	imp:p=1 \$ Side vacuum
6	0		307 -308 -605	imp:p=1 \$ Back vacuum
7	2	-2.699	302 -303 -606	imp:p=1 \$ Al casing (front)
8	2	-2.699	303 -308 605 -606	imp:p=1 \$ Al casing (side)
9	2	-2.699	308 -309 -606	imp:p=1 \$ Al casing (back)
10	3	-.0013	301 -302 -607	imp:p=1 \$ Air (front)
11	3	-.0013	302 -309 606 -607	imp:p=1 \$ Air (side)
12	3	-.0013	309 -310 -607	imp:p=1 \$ Air (back)
13	0		607:-301:310	imp:p=0 \$ Universe
14	2	-2.699	304 -307 -604 603	imp:p=1 \$ Al covering on dead layer

C End of Cell cards

C Surface cards

301	px	-50.0
302	px	0.0
303	px	0.07

304 px 0.97

305 px 1.04

306 px 2.18

307 px 6.02

308 px 7.02

309 px 7.09

310 px 10.0

C

601 cx 0.425

602 cx 2.365

603 cx 2.425

604 cx 2.625

605 cx 3.26

606 cx 3.41

607 cx 5.0

C End of surface cards

mode p

sdef pos=-5.0 0 0 erg=d1

si1 1 0.088 0.122 0.136 0.279 0.662

sp1 0.1 0.1 0.1 0.1 0.1

f8:p 2

e0 0 2600I 1.300

m1	32000	1.0		
m2	13027	1.0		
m3	7000	0.78		
	8000	0.22		
nps	1.0E+8			
prdmp	1.0E+8	-5	j	4
phys:p	1.300	0		1

```
c    /// ALL THE QUANTITIES ARE IN CGS UNITS. ///
```

```
      N = 10
```

```
      nmax = 100000
```

```
c    /// OPENING AN INPUT AND OUTPUT FILE ///
```

```
      open (9 ,file = 'transm.txt')
```

```
      open (8, file = 'cylinder.out')
```

```
      h = 2.0
```

```
      d = 100.0
```

```
      g = 2.5
```

```
      amu = 0.502294
```

```
c    /// READING THE INPUT FILE ///
```

```
      do 20 k = 1, N
```

```
        read (9,*) tt
```

```
        alnt = alog (tt)
```

```
c    /// CALCULATION OF SAMPLE RADIUS ///
```

```
      f = (-alnt/amu/2.0)
```

```
      sum1 = 0.
```

```
      sum2 = 0.
```

```
      do 10 i = 1, nmax
```

```
c    /// GENERATION OF RANDOM POINTS IN SAMPLE VOLUME ///
```

```
      a = aphas (-f, f)
```

```
      b = aphas (-f, f)
```

```
      c = aphas (-h/2, h/2)
```

```

bb=sqrt (a*a + b*b)
if (bb.gt.f) goto 10
c  /// GENERATION OF RANDOM POINTS ON DETECTOR SURFACE ///
a1 = aphas ( -g, g)
c1 = aphas ( -g, g)
aaa = sqrt (a1*a1+c1*c1)
bbb = g
if (aaa.gt.bbb) goto 10
c  /// CALCULATION OF (X,Y,Z) ///
p = (d-b)**2+(a1-a)**2
q = -2.0*(a1-a)*(b*a1-a*d)
s = f**2*(d-b)**2
s = -(s-(b*a1-a*d)**2)
y1 = q*q-4.0*p*s
y = (-q+sqrt(y1))/(2.0*p)
z = (y*(c1-c)-b*c1+c*d)/(d-b)
x = (y*(a1-a)-b*a1+a*d)/(d-b)
c  /// CALCTN OF NUMERATOR AND DENOMINATOR OF EQN 3.14 ///
t = sqrt((b-y)**2+(c-z)**2+(a-x)**2)
rsquare = ((b-d)**2+(c-c1)**2+(a-a1)**2)
term = (exp(-amu*t))/rsquare
sum1 = sum1+(1./rsquare)
sum2 = sum2+term

```

```
10  continue

c   /// ATTENUATION CORRECTION FACTOR CALCULATION ///

    cfat = sum1/sum2

    print *,cfat, tt, f

c   /// WRITING THE OUTPUT IN FILE ///

    write (8,*) tt, f, cfat,

20  continue

    end

    Function aphasax1, x2)

c   aphasax

c   random floating point number equally distributed between x1 and x2

    double precision a,b

    data a /.78149275363e0/

    b = (a+11d0/87d0)*87d0

    i = b

    a = b-i

    aphasax = x1+(x2-x1)*a

    return

    end
```

A Typical Input File for the Attenuation Correction Program

Input 1. “transm.txt”

.01
.09
.17
.25
.33
.41
.57
.73
.89
.97

This input file gives the values of the transmittance at which attenuation correction factors have to be calculated.

Program 2. Box geometry

```

*****
cc --- Attenuation correction factors for box geometry -----
*****

c      /// DESCRIPTION OF THE PARAMETERS ///
c      N = Number of input transmittance value for which attenuation
c      correction factor has to be calculated
c      nmax = number of random points generated
c      d = sample-to-detector distance taken from the centre of the sample
c      amu = linear attenuation coefficient
c      tt = transmittance, g = radius of detector crystal
c      yy, f = half thickness of box
c      CFAT = Attenuation correction factor
c      /// ALL THE QUANTITIES ARE IN CGS UNITS. ///

      N = 10

      nmax = 100000

c      /// OPENING AN INPUT AND OUTPUT FILE ///

      open(8, file='transm.txt')

      open(9, file='box.out')

      amu= 0.502294

      d=100.0

c      /// READING THE INPUT FILE ///

      do 20 k=1, N

```

```

read (8,*)tt
alnt = alog(tt)
c    /// CALCULATION OF SAMPLE HALF-THICKNESS ///
f = -alnt/amu/2.0
yy = f
sum1 = 0.
sum2 = 0.
do 10 i = 1, nmax
c    /// GENERATION OF RANDOM POINTS IN SAMPLE VOLUME ///
a= aphas(0.0, f)
b = aphas(-f, f)
c = aphas(0.0, f)
c    /// GENERATION OF RANDOM POINTS ON DETECTOR SURFACE ///
a1 = aphas(-g, g)
c1 = aphas(-g, g)
aaa = sqrt (a1*a1+c1*c1)
bbb = g
if (aaa.gt.bbb) goto 10
c    /// CALCULATION OF (X,Y,Z) ///
z=(yy*(c1-c)-b*c1+c*d)/(d-b)
x=(yy*(a1-a)-b*a1+a*d)/(d-b)
c    /// CALCTN OF NUMERATOR AND DENOMINATOR OF EQN 3.14 ///
t=sqrt((b-yy)**2+(c-z)**2+(a-x)**2)

```

```

rsquare=((b-d)**2+(c-c1)**2+(a-a1)**2)
term=(exp(-amu*t))/rsquare
sum1=sum1+(1./rsquare)
sum2=sum2+term
10  continue
c   /// ATTENUATION CORRECTION FACTOR CALCULATION ///
    cfat=sum1/sum2
    print *,tt, f, cfat
c   /// WRITING THE OUTPUT IN FILE ///
    write(9,*)tt, f, cfat
20  continue
    end
    function aphasax(x1,x2)
c   aphasax
c   random floating point number equally distributed between x1 and x2
    double precision a, b
    data a /.78149275363e0/
    b=(a+11d0/87d0)*87d0
    i=b
    a=b-i
    aphasax=x1+(x2-x1)*a
    return
    end

```

Program 3. Spherical geometry

```

c
*****

cc --- Attenuation correction factors for spherical geometry -----

*****

c      /// DESCRIPTION OF THE PARAMETERS ///
c      N = Number of input transmittance value for which attenuation
c      correction factor has to be calculated
c      nmax = number of random points generated
c      d = sample-to-detector distance taken from the centre of the sample
c      amu = linear attenuation coefficient
c      tt = transmittance
c      f = radius of sphere
c      g = radius of detector crystal
c      CFAT = Attenuation correction factor
c      /// ALL THE QUANTITIES ARE IN CGS UNITS. ///

      N = 10

      nmax = 100000

c      /// OPENING AN INPUT AND OUTPUT FILE ///

      open (8,file = 'transm.txt')

      open (9,file = 'sphere.out')

      d = 100.0

      amu = 0.502294

```

```

c      /// READING THE INPUT FILE ///

      do 20 k = 1, N

      read (8,*) tt

      sum1 = 0.

      sum2 = 0.

      tt = float(k)/100.0

      alnt = alog(tt)

c      /// CALCULATION OF SAMPLE RADIUS ///

      f = -alnt/amu/2.

      do 10 i = 1,nmax

c      /// GENERATION OF RANDOM POINTS IN SAMPLE VOLUME ///

      a = aphas (-f, f)

      b = aphas (-f, f)

      c = aphas (-f, f)

      abc = sqrt (a*a + b*b + c*c)

      if (abc.gt.f) goto 10

c      /// GENERATION OF RANDOM POINTS ON DETECTOR SURFACE ///

      c1 = aphas (-g, g)

      pp = sqrt (g*g - c1*c1)

      a1 = aphas (-pp, pp)

c      /// CALCULATION OF (X,Y,Z) ///

      p = (d-b)**2+(c1-c)**2+(a1-a)**2

      q = -2.0*((c1-c)*(b*c1-c*d)+(a1-a)*(b*a1-a*d))

```

```

s = f**2*(d-b)**2
s = -(s-(b*c1-c*d)**2-(b*a1-a*d)**2)
y1 = q*q-4.0*p*s
y = (-q + sqrt(y1))/(2.0*p)
z = (x*(c1-c)-b*c1+c*d)/(d-b)
x = (x*(a1-a)-b*a1+a*d)/(d-b)
c    /// CALCLTN OF NUMERATOR AND DENOMINATOR OF EQN 3.14 ///
t = sqrt((b-y)**2+(c-z)**2+(a-x)**2)
rsquare = ((b-d)**2+(c-c1)**2+(a-a1)**2)
term = (exp(-amu*t))/rsquare
sum1 = sum1+(1./rsquare)
sum2 = sum2+term
10   continue
c    /// ATTENUATION CORRECTION FACTOR CALCULATION ///
cfat = sum1/sum2
c    /// WRITING THE OUTPUT IN FILE ///
write (9,*) tt, f, cfat
20   continue
end
function aphasax(x1, x2)
c    aphasax
c    random floating point number equally distributed between x1 and x2
double precision a, b

```

```
data a /.78149275363e0/  
b = (a+11d0/87d0)*87d0  
i = b  
a = b-i  
aphasa = x1+(x2-x1)*a  
return  
end
```

Program 4. Disc geometry

```

c
*****

cc --- Attenuation correction factors for disc geometry -----

*****

c      /// DESCRIPTION OF THE PARAMETERS ///

c      N = Number of input transmittance value for which attenuation
c      correction factor has to be calculated

c      h = Half - thickness of the disc

c      nmax = number of random points generated

c      d = sample-to-detector distance taken from the centre of the sample

c      amu = linear attenuation coefficient

c      tt = transmittance

c      f = radius of cylinder

c      g = radius of detector crystal

c      CFAT = Attenuation correction factor

c      /// ALL THE QUANTITIES ARE IN CGS UNITS. ///

c      N = 10

c      nmax = 100000

c      /// OPENING AN INPUT AND OUTPUT FILE ///

c      open(8, file='transm.txt')

c      open(9, file='disc.out')

c      d = 100.0

```

```
g = 1.27
c  /// READING THE INPUT FILE ///

do 20 k = 1,16

read(8,*) tt

tt = float(k)/100.0

alnt = alog(tt)

c  /// CALCULATION OF SAMPLE THICKNESS ///

g = -alnt/amu/2.

sum1 = 0.

sum2 = 0.

do 10 i = 1,nmax

c  /// GENERATION OF RANDOM POINTS IN SAMPLE VOLUME ///

a = apha (0.0, f)

b = apha (-h, h)

c = apha (0.0, f)

bb=sqrt(a*a + c*c)

if (bb.gt.f) goto 10

c  /// GENERATION OF RANDOM POINTS ON DETECTOR SURFACE ///

a1 = apha (-g, g)

c1 = apha (-g, g)

aaa = sqrt(a1*a1 + c1*c1)

bbb = g

if(aaa.gt.bbb) goto 10
```

$$z = (f*(c1-c)-b*c1+c*d)/(d-b)$$

$$x = (f*(a1-a)-b*a1+a*d)/(d-b)$$

$$aa = \text{sqrt}(x*x + z*z)$$

$$bb = g$$

if(aa.gt.bb) then

c //// CALCULATION OF (X,Y,Z) ////

$$p = (c1-c)**2+(a1-a)**2$$

$$q = 2.0*(a1-a)*(a*c1-a1*c)$$

$$s = g**2*(c1-c)**2$$

$$s = -(s-(a*c1-c*a1)**2)$$

$$y = q*q-4.0*p*s$$

$$y1 = (-q+\text{sqrt}(y))/(2.0*p)$$

$$y2 = (-q-\text{sqrt}(y))/(2.0*p)$$

$$z = (y1*(c1-c)-b*c1+c*d)/(d-b)$$

$$x = (y1*(a1-a)-b*a1+a*d)/(d-b)$$

c //// CALCLTN OF NUMERATOR AND DENOMINATOR OF EQN 13 ////

$$t = \text{sqrt}((b-y1)**2+(c-z)**2+(a-x)**2)$$

$$\text{rsquare} = ((b-d)**2+(c-c1)**2+(a-a1)**2)$$

$$t = \text{sqrt}((b-h)**2+(c-z)**2+(a-x)**2)$$

$$\text{rsquare} = ((b-d)**2+(c-c1)**2+(a-a1)**2)$$

$$\text{term} = (\text{exp}(-\text{amu}*t))/\text{rsquare}$$

$$\text{sum1} = \text{sum1} + (1./\text{rsquare})$$

$$\text{sum2} = \text{sum2} + \text{term}$$

```
10    continue
c     ///< ATENUATION CORRECTION FACTOR CALCULATION ///<
      cfat = sum1/sum2
c     ///< WRITING THE OUTPUT IN FILE ///<
      write( 9,*) tt, cfat
20    continue
      end
      function aphasax1, x2
c     aphasax
c     random floating point number equally distributed between x1 and x2
      double precision a, b
      data a /.78149275363e0/
      b = (a+11d0/87d0)*87d0
      i = b
      a = b-i
      aphasax = x1+(x2 - x1)*a
      return
      end
```

APPENDIX III

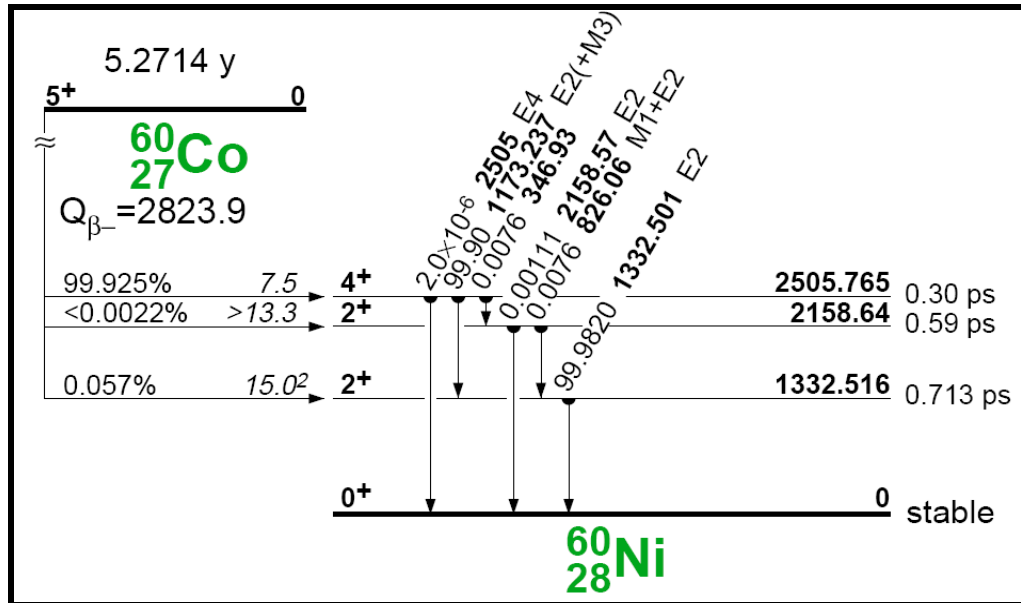
Coincidence Summing Corrections

(Decay schemes and numerical expressions for coincidence correction factors)

***** USE OF THE TABLES *****

1. (E) represents the total efficiency at the gamma ray energy E.
2. {E} represents the full energy peak efficiency at the gamma ray energy E.

I. ^{60}Co (β decay)



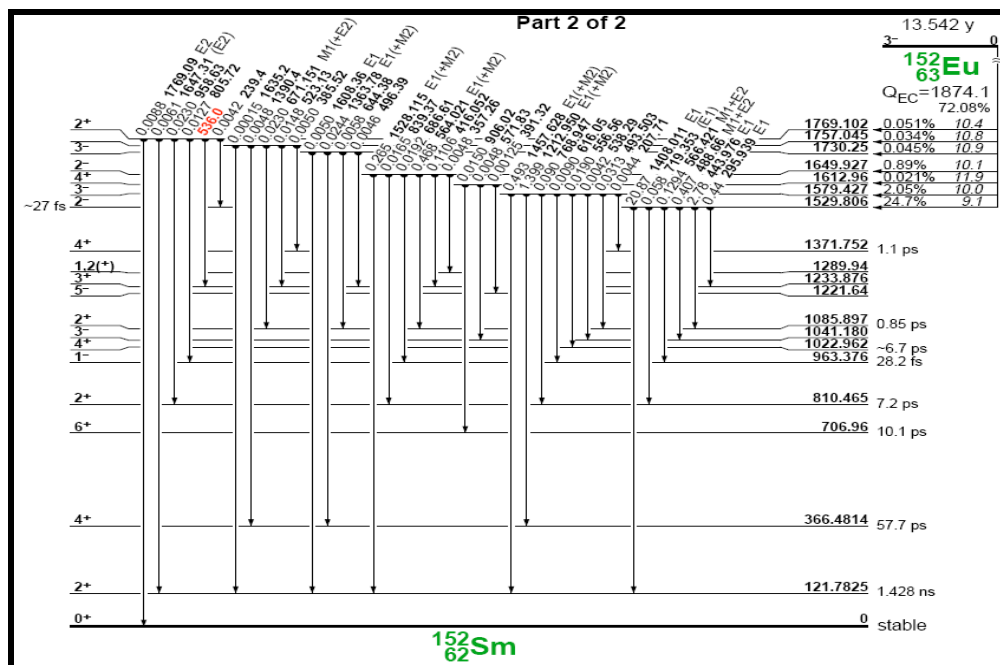
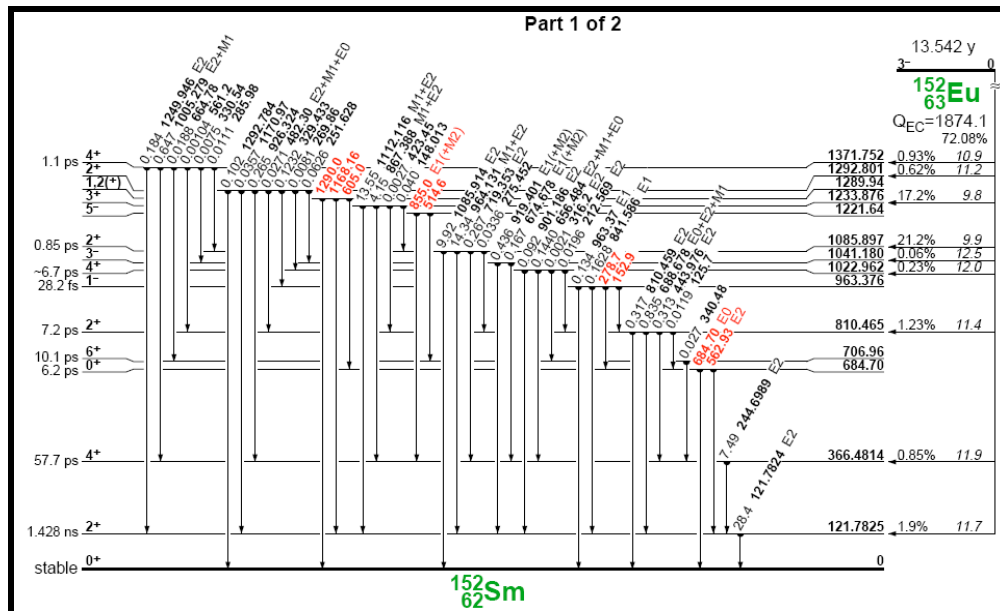
1173 keV

$$\frac{1}{k_{TCS}} = [1 - 0.904(1173)]$$

1332 keV

$$\frac{1}{k_{TCS}} = [1 - 0.904(1332)]$$

II. a) ^{152}Eu (EC decay)



121.8 keV

$$\begin{aligned} \frac{1}{k_{TCS}} = & [1 - 0.7720(KX) - 0.1218(244.7) - 0.0072(295.9) - 0.0269(444) - 0.0136(688.7) \\ & - 0.0043(719) - 0.0026(841.6) - 0.0675(867.4) - 0.0071(919.4) - 0.2332(964) \\ & - 0.2204(1112.9) - 0.0006(1170) - 0.0227(1212.9) - 0.0030(1249) - 0.3394(1408.0) \\ & - 0.0080(1457.6) - 0.0043(1528.1)] \end{aligned}$$

244.7 keV

$$\begin{aligned} \frac{1}{k_{TCS}} = & [1 - 1.06(KX) - 0.4619(121.8) - 0.0124(295.9) - 0.0377(444) - 0.0136(488) - 0.0174(656.5) \\ & - 0.0201(674.5) - 0.0322(719.4) - 0.5001(867.4) - 0.0319(926.3) - 0.0780(1005.3) \\ & - 0.1686(1212.9) - 0.0594(1457.6)] \end{aligned}$$

964 keV

$$\frac{1}{k_{TCS}} = [1 - 1.064(KX) - 0.4619(121.8) - 0.1129(444) - 0.0013(493) - 0.0190(564.0)]$$

444 keV

$$\begin{aligned} \frac{1}{k_{TCS}} = & [1 - 1.06(KX) - 0.2698(121.8) - 0.0098(244.7) - 0.0014(275) - 0.0108(719) - 0.5823(964) \\ & - 0.4028(1085)] \end{aligned}$$

1408 keV

$$\begin{aligned} \frac{1}{k_{TCS}} = & [1 - 1.046(KX) - 0.4619(121.8)] [1 + 0.0087 \{444\} \{964\} / \{1408\} + 0.0210 \{1112\} \{295.9\} / \{1408\} \\ & + 0.0141 \{488.6\} \{919.4\} / \{1408\}] \end{aligned}$$

867.4 keV

$$\frac{1}{k_{TCS}} = [1 - 1.046(KX) - 0.4619(121.8) - 0.9025(244.7) - 0.0247(295.9) - 0.0062(416)]$$

1112 keV

$$\frac{1}{k_{TCS}} = [1 - 1.063(KX) - 0.4619(121.8) - 0.0247(295.9) - 0.0041(416)] [1 + 0.2764 \{867.2\} \{244.8\} / \{1112\}]$$

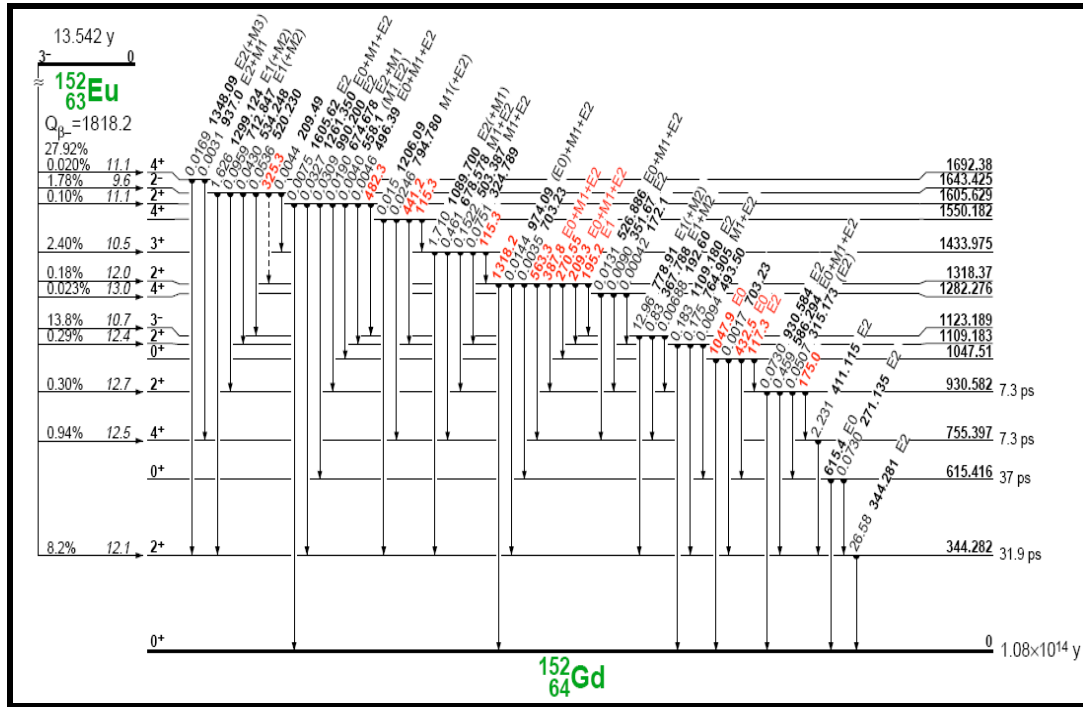
1085 keV

$$\frac{1}{k_{TCS}} = [1 - 0.771(KX) - 0.1084(444) - 0.0183(564)] [1 + 0.6677 \{964\} \{121.8\} / \{1085.8\}]$$

1212 keV

$$\frac{1}{k_{TCS}} = [1 - 0.771(KX) - 0.4619(121.8) - 0.9025(244.7)]$$

b) ^{152}Eu (β decay)



344.3 keV

$$\frac{1}{k_{TCS}} = [1 - 0.003(KX) - 0.0013(324) - 0.0300(367) - 0.0807(411.1) - 0.0092(503) - 0.0018(520) - 0.0166(586) - 0.0167(678) - 0.0063(764) - 0.4689(778.9) - 0.0619(1089.7) - 0.0589(1299)]$$

778.9 keV

$$\frac{1}{k_{TCS}} = [1 - 0.003(KX) - 0.9616(344.3) - 0.0039(520)][1 + 0.0014\{367.8\} \{411.1\} / \{778.9\}]$$

411 keV

$$\frac{1}{k_{TCS}} = [1 - 0.003(KX) - 0.9616(344.3) - 0.3633(367) - 0.0057(526) - 0.2018(678) - 0.0108(794)]$$

367 keV

$$\frac{1}{k_{TCS}} = [1 - 0.003(KX) - 0.9616(344.3) - 0.9767(411.1) - 0.0039(520)]$$

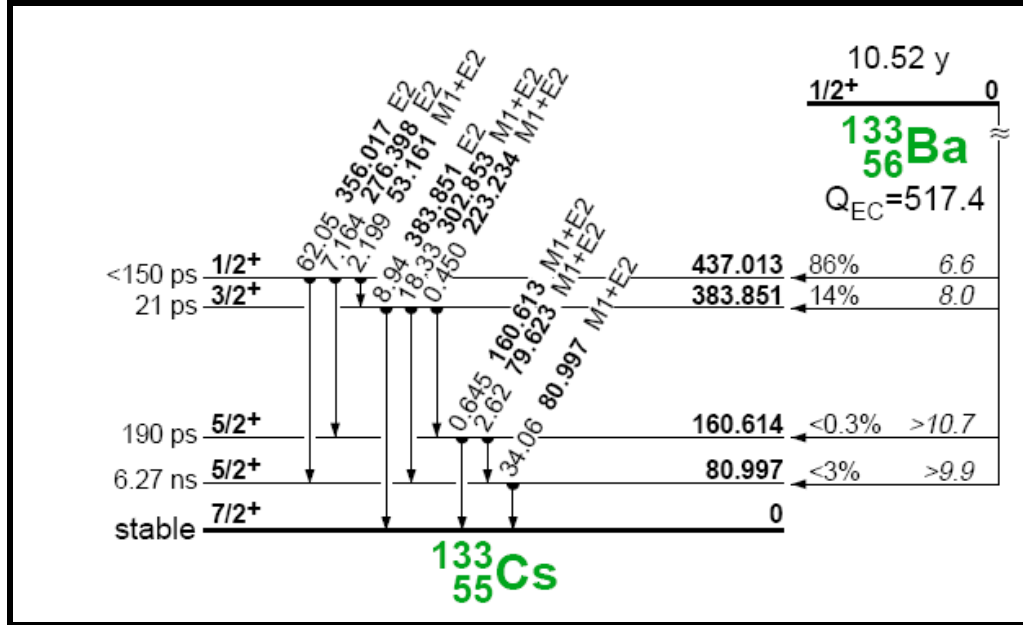
1089 keV

$$\frac{1}{k_{TCS}} = [1 - 0.003(KX) - 0.9616(344.3)][1 + 0.2633\{678\} \{411\} / \{1089\}]$$

1299 keV

$$\frac{1}{k_{TCS}} = [1 - 0.003(KX) - 0.9616(344.3)][1 + 0.0454\{712\} \{586\} / \{1299\} + 0.0125\{534\} \{764\} / \{1299\}]$$

III. ¹³³Ba (EC decay)



81 keV

$$\frac{1}{k_{TCS}} = [1 - 0.789(KX) - 0.0281(79.6) - 0.0157(53.2) - 0.0043(223.1) - 0.0689(276.4) - 0.196(302.9) - 0.665(356)]$$

302 keV

$$\frac{1}{k_{TCS}} = [1 - 1.478(KX) - 0.0076(53.2) - 0.3650(81)][1 + 0.0079\{223.1\} \{79.6\} / \{302.9\}]$$

356 keV

$$\frac{1}{k_{TCS}} = [1 - 1.2(KX) - 0.3650(81)][1 + 0.0373\{79.6\} \{276.4\} / \{356\} + 0.0226\{53.1\} \{302.9\} / \{356\}]$$

383 keV

$$\frac{1}{k_{TCS}} = [1 - 1.023(KX) - 0.0765(53.2)][1 + 0.7483\{81\} \{302.9\} / \{383.9\} + 0.004\{223.1\} \{160.6\} / \{383.9\}]$$

276 keV

$$\frac{1}{k_{TCS}} = [1 - 1.52(KX) - 0.3234(79.6) - 0.3269(81) - 0.0796(160.6)][1 + 0.0048\{53.2\} \{223.1\} / \{276.4\}]$$

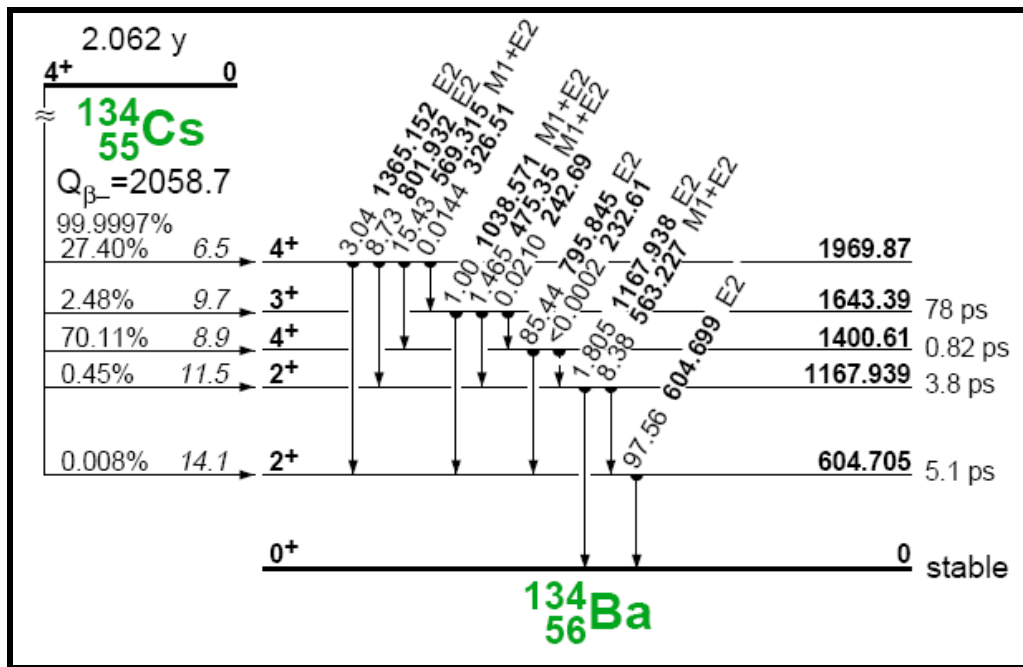
160 keV

$$\frac{1}{k_{TCS}} = [1 - 1.52(KX) - 0.0047(53.2) - 0.0555(223.1) - 0.8842(276.4)][1 + 1.4825\{81\} \{79.6\} / \{160.6\}]$$

223 keV

$$\frac{1}{k_{TCS}} = [1 - 1.52(KX) - 0.0765(53.2) - 0.3234(79.6) - 0.3269(81) - 0.0796(160.6)]$$

IV. $^{134}\text{Cs}(\beta \text{ decay})$



475.4 keV

$$\frac{1}{k_{TCS}} = [1 - 0.007(KX) - 0.00575(326.5) - 0.8173(563.2) - 0.8191(604.7) - 0.1760(1167.4)]$$

563.2 keV

$$\frac{1}{k_{TCS}} = [1 - 0.007(KX) - 0.1429(475.4) - 0.9944(604.7) - 0.8514(801.9)]$$

569.3 keV

$$\frac{1}{k_{TCS}} = [1 - 0.007(KX) - 0.9944(604.5) - 0.9971(795.8)][1 + 0.0009\{326.5\} \{242.7\} / \{569.3\}]$$

604.7 keV

$$\frac{1}{k_{TCS}} = [1 - 0.004(KX) - 0.0123(475.4) - 0.0854(563.2) - 0.1573(569.3) - 0.8709(795.8) - 0.0733(801.9) - 0.0102(1038.6) - 0.0310(1365.1)]$$

795.8 keV

$$\frac{1}{k_{TCS}} = [1 - 0.0064(KX) - 0.1801(569.3) - 0.9944(604.7)]$$

801.9 keV

$$\frac{1}{k_{TCS}} = [1 - 0.008(KX) - 0.8173(563.2) - 0.8191(604.7) - 0.1760(1167.4)][1 + 0.0016\{326.5\} \{475.4\} / \{801.8\}]$$

1365. keV

$$\frac{1}{k_{TCS}} = [1 - 0.0046(KX) - 0.9944(604.7)][1 + 0.0047\{326.5\} \{1038.6\} / \{1365.1\} + 5.0369\{569.3\} \{795.8\} / \{1365.1\} + 2.8492\{801.9\} \{563.2\} / \{1365.1\}]$$

1167.4 keV

$$\frac{1}{k_{TCS}} = [1 - 0.007(KX) - 0.0008(326.5) - 0.1429(475.4) - 0.8514(801.9)][1 + 4.6166\{563.2\} \{604.7\} / \{1167.4\}]$$

1038.6 keV

$$\frac{1}{k_{TCS}} = [1 - 0.007(KX) - 0.0058(326.5) - 0.9944(604.7)][1 + 1.1973\{563.2\} \{475.4\} / \{1038.6\}]$$

0